CHARMONIUM IN HOT MEDIUM

A Dissertation

by

XINGBO ZHAO

Submitted to the Office of Graduate Studies of
Texas A&M University
in partial fulfillment of the requirements for the degree of

DOCTOR OF PHILOSOPHY

December 2010

Major Subject: Physics

CHARMONIUM IN HOT MEDIUM

A Dissertation

by

XINGBO ZHAO

Submitted to the Office of Graduate Studies of
Texas A&M University
in partial fulfillment of the requirements for the degree of

DOCTOR OF PHILOSOPHY

Approved by:

Chair of Committee,	Ralf Rapp
Committee Members,	Che-Ming Ko
	Joseph Natowitz
	Bhaskar Dutta
	Valery Pokrovsky
Head of Department,	Edward Fry

December 2010

Major Subject: Physics

ABSTRACT

Charmonium in Hot Medium. (December 2010)
Xingbo Zhao, B.S., University of Science and Technology of China
Chair of Advisory Committee: Dr. Ralf Rapp

We investigate charmonium production in the hot medium created by heavy-ion collisions by setting up a framework in which in-medium charmonium properties are constrained by thermal lattice QCD (lQCD) and subsequently implemented into kinetic approaches. A Boltzmann transport equation is employed to describe the time evolution of the charmonium phase space distribution with the loss and gain term accounting for charmonium dissociation and regeneration (from charm quarks), respectively. The momentum dependence of the charmonium dissociation rate is worked out. The dominant process for in-medium charmonium regeneration is found to be a 3-to-2 process. Its corresponding regeneration rates from different input charm-quark momentum spectra are evaluated. Experimental data on J/ψ production at CERN-SPS and BNL-RHIC are compared with our numerical results in terms of both rapidity-dependent inclusive yields and transverse momentum (p_t) spectra. Within current uncertainties from (interpreting) lQCD data and from input charm-quark spectra the centrality dependence of J/ψ production at SPS and RHIC (for both mid- and forward rapidity) is reasonably well reproduced. The J/ψ p_t data are shown to have a discriminating power for in-medium charmonium properties as inferred from different interpretations of lQCD results.

To my parents

ACKNOWLEDGMENTS

First, I would like to thank my advisor, Prof. Ralf Rapp, for his patience, enthusiasm and dedication. His guidance helped me during the research and writing of this dissertation. I look forward to our continued collaboration.

I wish to express my gratitude to Prof. Che-Ming Ko for his suggestions and help throughout the past five years.

Prof. Valery Pokrovsky, Prof. Bhaskar Dutta, and Prof. Joseph Natowitz deserve my special thanks as my dissertation committee members.

My sincere thanks also go to Prof. Pengfei Zhuang and Mr. Yunpeng Liu in Tsinghua University. I learned a lot from the discussions with them.

I am grateful to Dr. Grandchamp Loic for providing us with his codes.

I acknowledge fruitful discussions with Dr. Hendrik van Hees, Dr. Riek Felix and Dr. Min He.

TABLE OF CONTENTS

CHAPTER Page

I INTRODUCTION 1

A. Quantum Chromodynamics 2
B. QCD Phase Diagram 6
C. Heavy-Ion Collisions 8
D. Charmonium 16
E. Outline of Dissertation 23

II CHARMONIUM TRANSPORT THEORY 26

A. Overview of Charmonium Production in Relativistic Heavy-Ion Collisions 26
B. Boltzmann Transport Equation 28
1. General Setup 28
2. Rate-Equation 35
3. Equilibrium Limit 36
C. c-$\bar{c}$ Correlations for Charmonium Production 40
1. Charmonium Production in the Canonical Ensemble . 40
2. Charm-Quark Correlation Volume 44

III CHARMONIUM IN THE HOT MEDIUM 47

A. Charmonium in QGP 47
B. Charmonium Dissociation in the QGP 50
C. Charm-Quark Spectra and Charmonium Regeneration in the QGP 56
D. Charmonium Dissociation in Hadronic Matter 61
E. Charmonium Spectral Function 63

IV THERMAL FIREBALL DESCRIPTION OF MEDIUM EVOLUTION 69

A. Fireball Expansion Profile 69
B. Equation of State of the Medium 70
C. Blastwave Description of Charmonium p_t Spectra 75

V PRIMORDIAL CHARMONIUM PRODUCTION 78

CHAPTER Page

A. Charmonium Production in p+p Collisions 78
B. Charmonium Production in A+A Collisions 81
1. Brief Review of Glauber Model 81
2. Cold Nuclear Matter Effects 84
a. Nuclear Shadowing 84
b. Cronin Effect 87
c. Nuclear Absorption 88
3. Implementation of CNM Effects 89

VI APPLICATION TO HEAVY-ION COLLISIONS 97

A. The Rate Equation Approach 98
B. Inclusive J/ψ Yield and p_t Spectra at SPS and RHIC . . . 104
1. Inclusive J/ψ Yield 104
2. J/ψ Transverse Momentum Spectra 111
a. Average Transverse Momentum 111
b. High p_t J/ψ Production and Elliptic Flow 114
C. Explicit Calculations of the Regeneration Component . . . 119
1. Sensitivity of J/ψ Regeneration to Charm-Quark p_t Spectra 119
2. Sensitivity of J/ψ Regeneration to Charm-Quark Correlation Volume 122
D. ψ' and χ_c Production 124
E. Charmonium Production at FAIR 126

VII CONCLUSIONS AND OUTLOOK 132

REFERENCES 136

VITA 147

LIST OF FIGURES

FIGURE		Page
1	Elementary particles in the standard model	1
2	Running coupling constant α_s of QCD	3
3	Energy density and chiral condensate from lQCD	7
4	Schematic view of QCD phase diagram in terms of the baryon chemical potential μ_B and temperature T	8
5	Schematic picture of the various stages of a heavy-ion collision	10
6	Schematic representation of a noncentral heavy-ion collision, characterized by an almond-shaped initial overlap zone, and a subsequent pressure-driven build-up of elliptic flow	11
7	Spacetime diagram of ultra-relativistic nuclear collisions	12
8	Elliptic flow measured by PHENIX and STAR compared to hydrodynamic calculations	13
9	$R_{AA}(p_t)$ ratio measured by PHENIX for neutral pions, compared to jet-quenching calculations	15
10	Charmonium spectrum	16
11	Schematic representation of color-Debye screening in a deconfined medium	18
12	Charmonium binding energies as a function of Debye mass	19
13	Free energy of a static $c\bar{c}$ pair, as computed in lattice QCD	20
14	Charmonium correlator ratio in the vector and scalar channel as computed in lattice QCD	22

FIGURE Page

15 The probability distribution of integer number (k) pairs of charm quarks in one event 42

16 Temperature dependence of in-medium charm quark mass in the strong and weak binding scenarios 48

17 Temperature dependence of J/ψ binding energy in the strong and weak binding scenarios 49

18 Diagram of the gluo-dissociation process 51

19 Comparison of the parton-induced dissociation cross section 52

20 Diagrams of the quasifree process 53

21 Temperature and momentum dependence of Ψ dissociation rates . . . 55

22 Charm-quark p_t spectra and J/ψ regeneration rates 59

23 J/ψ dissociation rates by pions and rhos as a function of the temperature T of the hadron gas 62

24 Temperature dependence of the strength of the resonance part of the S-wave spectral function, $Z_\Psi(T)$, for the strong and weak binding scenarios 65

25 Spectral functions in the vector channel for the strong and weak binding scenarios 66

26 Ratio of vector channel correlator to the reconstructed correlator for the strong and weak binding scenarios 67

27 Spectral functions in the scalar channel 67

28 Comparison of energy density and pressure from an ideal massive parton gas with data from lattice QCD 71

29 Time profiles of temperature for central collisions of heavy nuclei (participant number $N_{\rm part}$=380) at RHIC and SPS 72

30 Excitation function of the baryon chemical potential at the assumed phase transition line 73

FIGURE Page

31 Temperature evolution of heavy-ion collisions at FAIR 74

32 Schematic representation of the geometry of Glauber model 82

33 Modification of parton distribution function in lead nucleus 85

34 Rapidity dependence of J/ψ R_{dAu} in d+Au collisions at $\sqrt{s}$=200AGeV measured by PHENIX 87

35 $\langle p_t^2 \rangle$ of the J/ψ as a function of the geometric length of matter, L, traversed by partons in the initial state 88

36 J/ψ R_{AA} (normalized to Drell-Yan pairs) vs. L for p+A, S+U, Pb+Pb systems 89

37 Centrality dependence of J/ψ R_{dAu} in 200AGeV d+Au collisions measured by PHENIX 90

38 Schematic representation of the geometry of J/ψ nuclear absorption . 91

39 Centrality dependence of J/ψ R_{dAu} in 200 AGeV d+Au collisions measured by PHENIX together with a Glauber fit with a nuclear absorption cross section σ_{abs}=3.2mb, 3.5mb, and 7.8mb for backward, mid- and forward rapidity 94

40 Temperature dependence of charm-quark fugacity and in-medium J/ψ equilibrium limit using the statistical model in the QGP within the strong-binding scenario, the weak-binding scenario and in the hadronic phase for temperatures below T_c=180 MeV 101

41 J/ψ production versus centrality at SPS evaluated with the thermal rate-equation approach, compared to NA50 data 105

42 J/ψ R_{AA} versus centrality at mid-rapidity at RHIC evaluated with the thermal rate-equation approach, compared to PHENIX data . . . 106

43 J/ψ R_{AA} versus centrality at forward rapidity at RHIC compared to PHENIX data 107

44 Ratio of J/ψ R_{AA} between forward and mid-rapidity versus centrality in the strong and weak binding scenarios compared to PHENIX data 108

FIGURE Page

45 J/ψ abundance as a function of time in central collisions at RHIC . . 110

46 $\langle p_t^2 \rangle$ of J/ψ vs. centrality at SPS, compared to NA50 data 112

47 $\langle p_t^2 \rangle$ of J/ψ vs. centrality at RHIC at mid-rapidity and forward rapidity, compared to PHENIX data 113

48 Ratio of J/ψ from B-meson feeddown to inclusive J/ψ indicated by Tevatron and STAR data 115

49 J/ψ R_{AA} versus p_t in central 200 AGeV Au+Au collisions including formation-time effects and B-meson feeddown contributions . . . 116

50 J/ψ R_{AA} vs. p_t in 0-60% Cu+Cu at RHIC, compared RHIC data . . 117

51 J/ψ $v_2(p_t)$ for 20-40% central Au+Au collisions at RHIC 119

52 J/ψ regeneration from different charm-quark spectra 120

53 $\langle p_t^2 \rangle$ of J/ψ's regenerated from different charm-quark spectra 121

54 J/ψ regeneration with different charm-quark correlation volumes . . 123

55 Inclusive ψ' to J/ψ ratio at SPS compared to NA50 data 125

56 Inclusive $\psi'/(J/\psi)$ and $(\chi_{c1}+\chi_{c2})/(J/\psi)$ ratio at RHIC evaluated with the thermal rate-equation approach 126

57 Temperature dependence of J/ψ binding energy at FAIR in the strong binding scenario 127

58 Results of the thermal rate-equation approach for $R_{AA}^{J/\psi}$ vs. centrality at FAIR 127

59 Results of the thermal rate-equation approach for the $\psi'/(J/\psi)$ ratio vs. centrality at FAIR 129

60 Results of the thermal rate-equation approach for $\langle p_t^2 \rangle$ vs. centrality at FAIR 129

61 $R_{AA}^{J/\psi}$ vs. transverse momentum for different centrality selections of Pb+Pb collisions at FAIR 131

CHAPTER I

INTRODUCTION

The standard model has been established as the underlying theory of modern particle physics. It describes the three fundamental interactions (electromagnetic, weak and strong) in a unified framework. The standard model includes 12 spin-1/2 particles (fermions). They are six quarks: up (u), down (d); charm (c), strange (s); top (t), bottom (b) and six leptons: electron (e), electron neutrino (ν_e), muon (μ), muon neutrino (ν_μ), tau (τ), tau neutrino (ν_τ). It also includes spin-1 particles (bosons) mediating the interaction between fermions. They are the photon mediating the electromagnetic interaction, W^+, W^- and Z bosons mediating the weak interactions and 8 gluons mediating the strong interaction. The elementary particles in the standard model are summarized in Fig. 1.

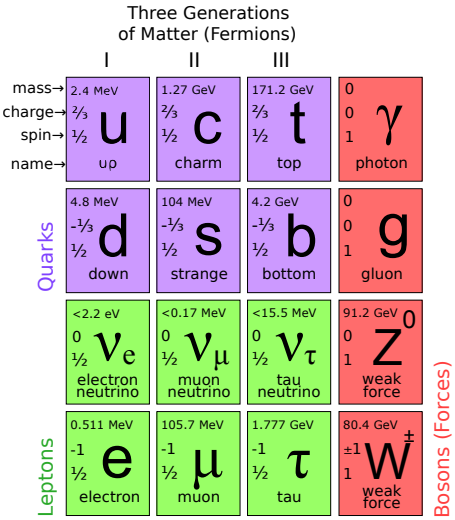

Fig. 1. Elementary particles in the standard model.

The interaction among elementary particles is mathematically described by gauge

---

This dissertation follows the style of Physical Review C.

field theories with the (local) gauge symmetry group of $SU(3)_C \otimes SU(2)_L \otimes U(1)_Y$, where $SU(3)_C$ and $SU(2)_L \otimes U(1)_Y$ are the gauge groups governing the strong and the electro-weak interaction, respectively. The gauge field theory with the $SU(3)_C$ gauge group is quantum chromodynamics (QCD) [1, 2]. Although QCD has been established as the underlying theory for the strong interaction, many aspects of it are still not well understood, especially in regimes where the strong coupling becomes large. The ultimate goal of this work is to improve our understanding about the strong interaction in these regimes. Therefore let us begin with a review of properties of QCD.

A. Quantum Chromodynamics

The fundamental degrees of freedom in QCD are quarks and gluons. Their interaction is described by the following Lagrangian,

$$\mathcal{L}_{QCD} = \sum_f^{N_f} \bar{\psi}_f (i\gamma^\mu D_\mu - m_f)\psi_f - \frac{1}{4} F_a^{\mu\nu} F^a_{\mu\nu} \ . \tag{1.1}$$

Here the gluon field strength tensor $F^a_{\mu\nu}$ reads

$$F^a_{\mu\nu} = \partial_\mu A^a_\nu - \partial_\nu A^a_\mu + ig f_{abc} A^b_\mu A^c_\nu \ , \tag{1.2}$$

in terms of the gluon gauge fields A^μ_a (a$= 1 \cdots 8$). The colored quark fields ψ_f ($f = u, d, s, c, b, t$) are coupled to the gluons through the gauge covariant derivative

$$D_\mu = \partial_\mu - ig\frac{\lambda_a}{2} A^a_\mu \ , \tag{1.3}$$

where λ_a are the Gell-Mann matrices, which are generators of the $SU(3)_c$ group satisfying

$$[\lambda_a, \lambda_b] = f_{abc}\lambda_c \ , \tag{1.4}$$

f_{abc} being the structure constants of $SU(3)_c$.

The important properties of QCD include:

1. Asymptotic freedom. One of the most notable differences between the strong and electromagnetic interaction comes from the fact that not only quarks but also gluons themselves carry color charge, reflected in the last term of Eq. (1.2). This gives rise to gluon self-interactions, which in turn lead to the QCD coupling constant,$\alpha_s = g^2/4\pi$ decreasing logarithmically with the momentum transfer in the process,

$$\alpha_s(Q) = \frac{g^2}{4\pi} = \frac{1}{\beta_0 \ln(Q^2/\Lambda^2_{QCD})} \ , \tag{1.5}$$

where $\Lambda_{QCD} \simeq$200MeV is introduced as a "non-perturbative" scale where $\alpha_s(Q)$ for-

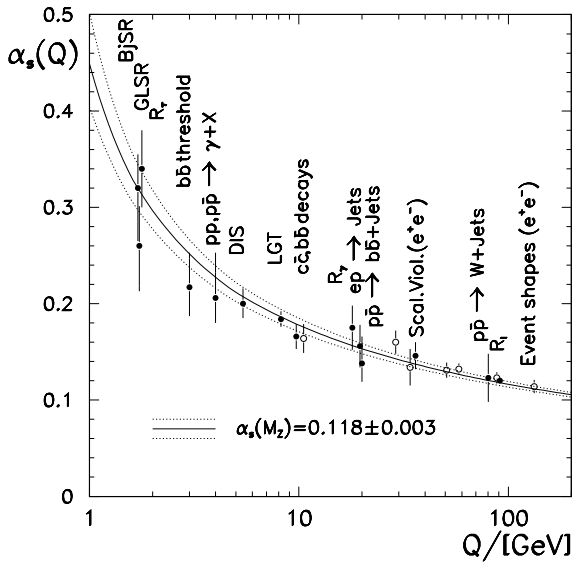

Fig. 2. Running coupling constant α_s of QCD. Dependence of the QCD coupling constant, $\alpha_s = g^2/4\pi$, on the momentum transfer, Q, of the interaction. Figure taken from Ref. [3].

mally diverges, see Fig. 2. Note that the logarithmic behavior in Eq. (1.5) is based on perturbative calculations, which break down at momentum transfer well above Λ_{QCD}. In practice, the scale for the onset of non-perturbative effects is typically given by

the hadronic mass scale of $\sim$1 GeV. For interactions with large momentum transfer $Q \gg 1\,\mathrm{GeV}$ (or equivalently at small distance $r \ll 1\mathrm{fm}$ according to the uncertainty principle), theoretical calculations can be organized in a converging series of terms characterized by increasing powers of α_s. In this "perturbative" regime, QCD is well tested, attaining excellent agreement with experiment. In the opposite limit, due to the growing strong coupling constant toward small Q, the perturbative expansion breaks down and the QCD enters the "strong" regime where "non-perturbative" phenomena occur.

2. Confinement. A striking non-perturbative phenomenon is the confinement of color charges, which refers to the fact that isolated colored particles, quarks and gluons, have never been observed. They are always confined in "bags" of color-neutral baryons or mesons. For example, in deep inelastic scattering (DIS) experiments, when a colored quark is knocked out of a proton, $q\bar{q}$ pairs form along the trajectory of the outgoing quark to neutralize color. The knocked-out quark is thus accompanied by large concentrations of hadrons along its direction of propagation, so-called "jets".

3. Spontaneous Breaking of Chiral Symmetry (SBCS). Usually the u and d (and sometimes s) quarks are referred to as "light quarks"; c, b, t quark are referred to as heavy quarks. In the massless limit of light quarks the QCD Lagrangian with two light flavors can be written as

$$\mathcal{L}_{QCD} = \bar{\psi}_L i\gamma^\mu D_\mu \psi_L + \bar{\psi}_R i\gamma^\mu D_\mu \psi_R - \frac{1}{4} F_a^{\mu\nu} F^a_{\mu\nu} \,, \tag{1.6}$$

where

$$\psi = \begin{pmatrix} u \\ d \end{pmatrix} . \tag{1.7}$$

The ψ_L and ψ_R are the left-handed and right-handed components of the quark field. The Lagrangian (1.6) is unchanged under a rotation in flavor space ($u \leftrightarrow d$) "inde-

pendently" with respect to ψ_L or ψ_R. This symmetry of the Lagrangian is called the chiral symmetry. This symmetry is, however, spontaneously broken by the complex structure of QCD vacuum. The latter is filled with various condensates of quark-antiquark and gluon fields. In particular, the scalar quark condensate of up and down quarks can be quantified by a vacuum expectation value,

$$\langle\bar{\psi}\psi\rangle = \langle 0|\bar{\psi}_R\psi_L + \bar{\psi}_L\psi_R|0\rangle \simeq (-250\text{MeV})^3 \ , \tag{1.8}$$

translating into a total pair density of about $4/\text{fm}^3$ (for two flavors). As a result the quarks inside the hadrons propagating through the QCD vacuum acquire an effective mass, $m_q^* \simeq$350 MeV, which is much larger than their bare mass, $m_{u,d}^0 \simeq$ 5-10 MeV. The QCD condensates are thus the main source of the visible mass in the Universe.

Currently the theoretical efforts of studying QCD in the non-perturbative regime are mainly pursued in two directions:

1. Effective theory/model. Various effective theories are developed with degrees of freedom appropriately adapted to specific problems. They are rather successful in describing the physics within their applicable energy range. For example in the low-energy regime of QCD, chiral perturbation theory was developed with hadrons, rather than quarks and gluons, as the effective degrees of freedom. The interaction term is dictated by the chiral symmetry, which is approximately respected by the original QCD Lagrangian. After the effective coupling constants are determined by fitting to experimental data, chiral perturbation theory gains predictive power for low energy hadronic reactions/decays. Another example is Non-Relativistic QCD, in which the heavy quarks are described by a Schrödinger field theory while the gluons and light quarks are modelled by the usual relativistic Lagrangian of QCD.

2. Lattice QCD. The basic idea of lattice QCD (lQCD) is to study the QCD Lagrangian in discretized euclidean (imaginary-time) spacetime, with the lattice points,

called sites, separated by the lattice spacing, a. This effectively introduces an ultraviolet cutoff, $\Lambda = 1/a$ on any momentum component. Fermion fields, ψ, reside on the lattice sites, while the gauge fields, A, are associated with the links joining neighboring sites. The lQCD partition function can then be calculated on lattice as

$$\mathcal{Z} = \int [dA][d\bar{\psi}][d\psi] e^{-\int \mathcal{L} d^4x} \ . \tag{1.9}$$

Here functional integration denotes summing over all possible field configurations with every possible value of the gauge fields, the antifermion fields and the fermion fields on each link and sites, respectively. In practice, Monte-Carlo simulations are employed to make this summation process possible. In terms of the partition function the thermal average values of observables are given by

$$\langle \mathcal{O}(A, \bar{\psi}, \psi) \rangle = \frac{1}{\mathcal{Z}} \int [dA][d\bar{\psi}][d\psi] e^{-\int \mathcal{L} d^4x} \mathcal{O}(A, \bar{\psi}, \psi) \ . \tag{1.10}$$

Due to the "fermion sign problem" lQCD is currently applicable only in the regime of low baryon density.

As the computer technology and power have advanced in recent years lattice QCD has yielded many important results and thus provided profound insights into the non-perturbative regime of QCD, see Ref. [4] for a recent review. One of the central goals in this work is to establish the link between the lQCD results and heavy-ion phenomenology.

B. QCD Phase Diagram

A question of fundamental importance is what happens if the hadronic matter is compressed so that the distance between hadrons is smaller than the radius of hadrons. Intuitively one expects that the boundary of hadrons disappears and the quarks and

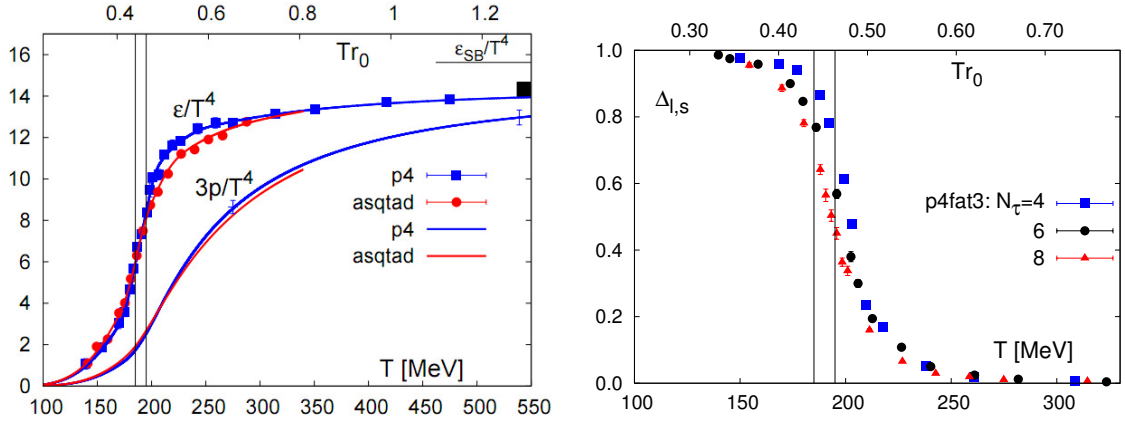

Fig. 3. Energy density and chiral condensate from lattice QCD. Left panel: Lattice calculation of the energy density and pressure of QCD matter as a function of temperature, taken from Ref. [5]. Right panel: Strength of the chiral condensate as a function of temperature, taken from Ref. [6].

gluons can move freely inside the entire nuclear matter and become the relevant degrees of freedom (deconfinement). It turns out that in the low baryon density region this picture is supported by recent lQCD calculations: The energy density shows a rapid rise in the temperature region around 170-190 MeV, as shown in the left panel of Fig. 3. At high temperatures the energy density ϵ is within 15% of the values expected for an ideal gas of quarks and gluons, known as the Stefan-Boltzmann limit, which implies the relevant degrees of freedom have indeed transitioned into quarks and gluons, forming the quark-gluon plasma (QGP). Lattice QCD calculations also show that the rapid increase of ϵ is accompanied by a sudden decrease of quark condensate, see the right panel of Fig. 3, implying its evaporation at high temperature similar to the evaporation of Cooper pairs above the critical temperature.

In the regime with low temperature and high baryon density (characterized by large baryon chemical potential, μ_B), theoretical studies [7, 8] reveal the existence of another deconfined phase, see Fig. 4, where the high density quarks form Cooper pairs which condense ($\langle qq \rangle \neq 0$) and result in superconducting of color charge.

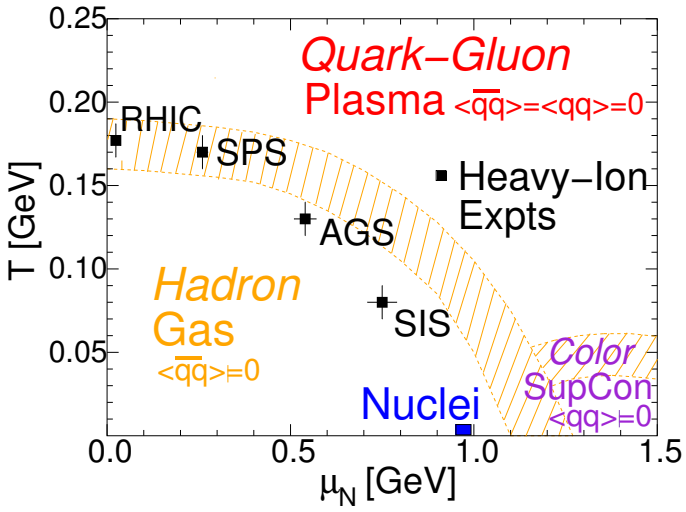

Fig. 4. Schematic view of QCD phase diagram in terms of the baryon chemical potential μ_B and temperature T. Figure taken from Ref. [9].

Since the formation of deconfined matter (also called quark matter) requires either extremely high temperature or density the natural occurrence is expected in the early universe or inside compact stars. According to the Big Bang theory the universe is believed to have passed through the QGP phase at the age of a few microseconds. Inside compact stars such as neutron star the temperature is far lower than 180MeV, but the high density makes it possible that the inside matter is in the color-superconducting phase. Since the properties of quark matter are characterized by the strong interactions, new insights about the strong interaction is expected to be obtained by studying these new states of matter.

C. Heavy-Ion Collisions

Since quark matter in nature is far from reach scientists are motivated to create it in laboratories, through ultra-relativistic heavy-ion collisions (URHICs).

The idea is that by accelerating heavy nuclei to very high speed and then colliding them a large amount of energy is deposited into a small spatial region and converted

to thermal energy resulting in extremely high temperature. The currently running experimental facilities include the Super-Proton-Synchrotron (SPS) at CERN, Relativistic Heavy-Ion Collider (RHIC) at BNL and newly constructed Large Hadron Collider (LHC) at CERN. The new Facility for Antiproton and Ion Research (FAIR) at GSI (Germany) will be completed within a few years. These experimental facilities come with one of two typical setups: the first category is the fixed-target experiments, in which only one beam of ions (the projectiles) is accelerated, and its colliding partner is placed in a stationary target into the path of the beam. The SPS and FAIR are fixed target experiments; the second category is the collider, in which both beams (projectile and targets) are accelerated and directed to collide with each other. The RHIC and LHC fall into this category. Usually the fixed target accelerators have higher luminosity (leading to a larger number of collision events per unit time) so that more rare reactions can be studied, whereas the advantage of colliders is that higher collision energy can be reached (in fixed target accelerators a large amount of the energy of the projectile is "wasted" on the kinetic energy of the center of mass of two colliding nuclei).

So far at SPS collisions have been conducted between various ion beams, such as proton (p), deuteron (d), O, S, Pb, and different targets such as S, Si, Cu, W, Pb, U, at different energies from 20 AGeV to 158 AGeV (for a proton beam it can reach up to 450 GeV). RHIC has produced collisions between p+p, d+Au, Cu+Cu and Au+Au at different energies ranging from $\sqrt{s}$=22.4AGeV to 200AGeV. In near future Pb+Pb collisions will be performed at LHC with up to $\sqrt{s}$=5.5 ATeV. FAIR will carry out heavy-ion collisions with $\sqrt{s}$ close to 10AGeV. Different heavy-ion experiments, with different beam energies, probe different regions in the QCD phase diagram, Fig. 4: the matter created in the central region of collisions with higher beam energies is more symmetric between baryons and antibaryons, while the lower energy experiments

(such as FAIR) enable to study the properties of dense baryonic matter. In this work we mainly focus on charmonium production in Pb(158 AGeV)+Pb collisions at SPS and $\sqrt{s}$=200 AGeV Au+Au collisions at RHIC.

The time evolution of a typical heavy-ion collision is sketched in Fig. 5. Two Lorentz-contracted nuclei approach each other at close to the speed of light until primordial nucleon-nucleon collisions occur. After subsequent reinteractions for τ_0=0.5-1fm/c a Quark-Gluon Plasma (QGP) is supposedly created. Driven by the pressure gradient the QGP expands and cools (for a duration of τ_{QGP} ~3-5fm/c). The hadronization then follows with further expansion in the hadronic phase until the "chemical freeze-out" point when inelastic interactions cease with particle abundances fixed; after further expansion/cooling until "kinetic freeze-out" elastic interactions stop with particle transverse momentum spectra fixed. The total fireball lifetime is approximately 10-15fm/c depending on the beam energy.

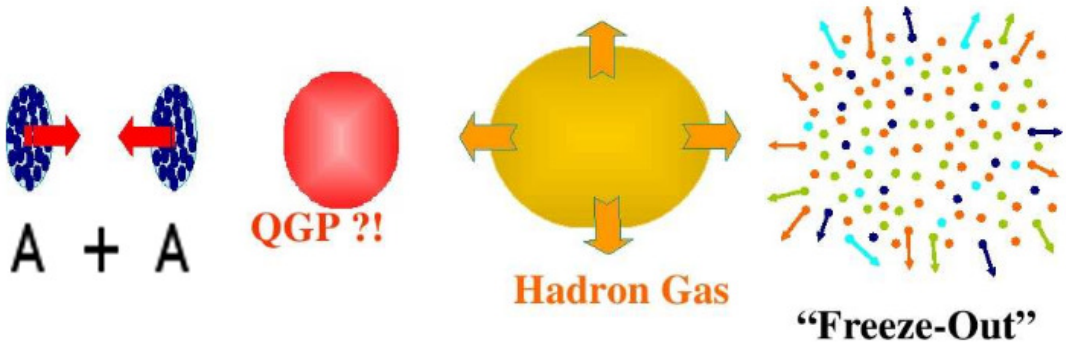

Fig. 5. Schematic picture of the various stages of a heavy-ion collision. Picture taken from Ref. [9].

It is convenient to introduce the standard coordinate system for heavy-ion collisions: The z axis is parallel to the beam line. Since most nucleus-nucleus (A-A) collisions are not head-on collisions, there exists a two-dimensional vector connecting

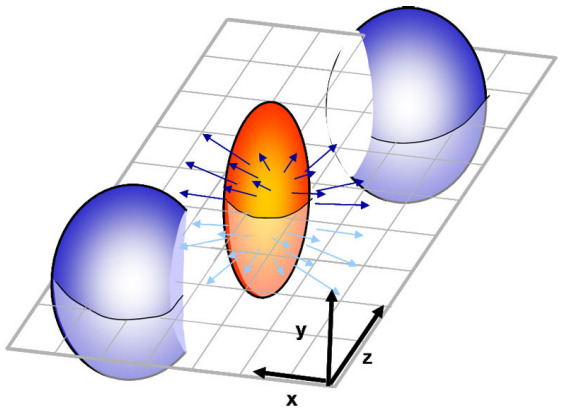

Fig. 6. Schematic representation of a noncentral heavy-ion collision, characterized by an almond-shaped initial overlap zone, and a subsequent pressure-driven build-up of elliptic flow. Picture taken from Ref. [9].

centers of the colliding nuclei in the plane transverse to z axis, which is called the impact vector, $\vec{b}$, its length is the impact parameter, b. The x-axis is chosen to be parallel to the impact vector, $\vec{b}$, see Fig. 6. The x- and z-axes span the "reaction plane" of a given collision. The x- and y-axes span the "transverse plane". The component of the 3-momentum of produced particles parallel to z-axis is denoted by p_z, and the transverse component is $\vec{p}_t$. For relativistic particles it is convenient to use the (longitudinal) rapidity instead of the (longitudinal) velocity. The former is defined as

$$y = \tanh^{-1}\left(\frac{p_z}{E}\right) = \tanh^{-1} v_z \ . \tag{1.11}$$

Here $E = \sqrt{m^2 + \vec{p}^2}$ is the energy of a particle. Due to the time-dilation effect particles with larger v_z in center of mass frame are "younger" than the ones with smaller v_z. This means that the above mentioned evolution of the matter is "measured" by the longitudinal proper time $\tau = \sqrt{t^2 - z^2}$ rather than by the lab time t, as illustrated in Fig. 7.

Due to the short lifetime of the medium, special probes are needed to access the

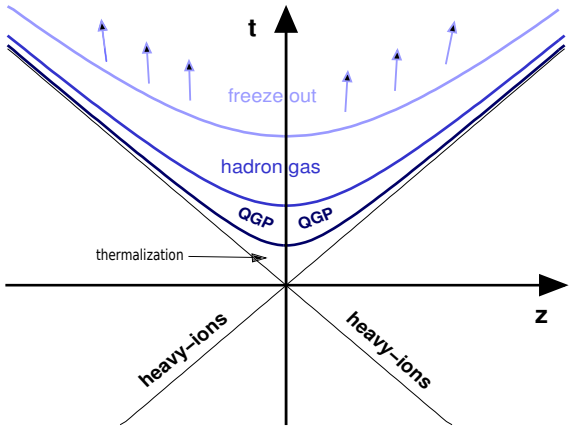

Fig. 7. The spacetime diagram of ultra-relativistic nuclear collisions. Figure taken from [10].

properties of the medium. The only probes turn out to be the produced particles themselves. According to their energies the probes are divided into two categories: soft probes and hard probes.

The soft probes are associated with the particles with relatively low energy (e.g., $\lesssim$2GeV), which constitute the bulk medium (>95% at RHIC) created in heavy-ion collisions. The soft probes reflect the collective properties of the medium, such as thermal and transport properties. One of the key measurements at RHIC is the elliptic flow, v_2, for the bulk particles (π,K,p). The elliptic flow, v_2, characterizes the azimuthal asymmetry of these particles in the transverse plane in terms of the second harmonic coefficient of an azimuthal Fourier decomposition of the momentum spectra,

$$\left.\frac{dN}{d^2p_t dy}\right|_{y=0} = \frac{dN}{\pi dp_t^2 dy}\left[1 + 2v_2(p_t)\cos(2\phi) + \dots\right]. \tag{1.12}$$

Here ϕ is the azimuthal angle in the transverse plane with ϕ=0 for x-axis. At mid-rapidity the system is symmetric about $y-z$ plane, so there is no $\cos\phi$ term.

For soft particles (p_t <2 GeV) the elliptic flow arises because, in semi-central

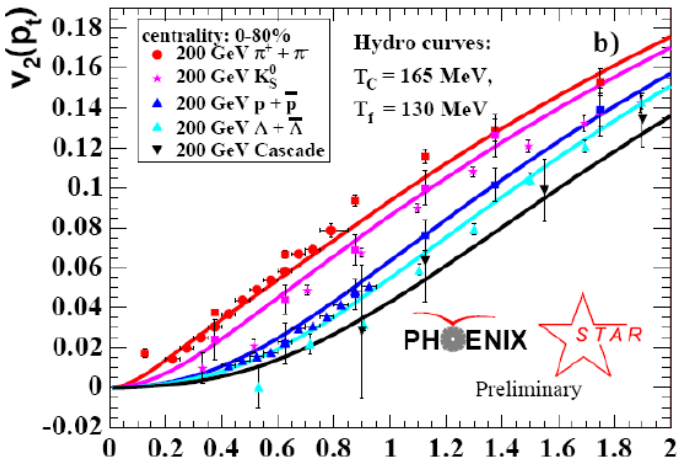

Fig. 8. Elliptic flow measured by PHENIX and STAR [11, 12] compared to hydrodynamic calculations [13].

collisions, the geometry of the initial interaction region has the shape of an ellipse, see Fig. 6. Once the system thermalizes this initial geometrical anisotropy translates into stronger pressure gradients in the direction of the smaller axis of the ellipse. This induces momentum correlations among particles which *flow* preferentially along the small axis of the ellipse, leading to a positive v_2, see Fig. 8. Since the spatial anisotropy is largest at the beginning of the evolution, a measurement of v_2 provides access to the thermalization time scale τ_0 of the system. Applications of ideal relativistic hydrodynamics have shown that the experimentally measured $v_2(p_T)$ for various hadrons (π, K, p, Λ) is best described when implementing a thermalization time of τ_0=0.5-1 fm/c.

Other valuable soft probes include particle ratios and the HBT (Hanbury-Brown-Twiss) particle interferometry. The former is used to estimate the temperature T and chemical potential μ_B of "chemical freeze-out" when the inelastic interactions cease and the particle ratios are fixed. The latter provides clues about the size, shape and time evolution of the medium [14].

To further study the properties of the medium, in particular the more microscopic aspects, the second category of the probes, namely the hard probes, are required.

The hard probes are associated with the particles with relatively high energy (>2GeV) including either light particles with large momentum or heavy particles irrespective of their momenta. Usually a hard probe can only be generated in initial hard collisions (their energy scale is usually much larger than the typical temperature of the medium) and their initial production can be estimated from p+p collisions. By measuring the modification of hard probes after traversing the QGP medium, one can obtain information on the microscopic interaction between strongly interacting medium and the probe particle. To quantitatively describe the modification due to the medium it is convenient to define the nuclear modification factor,

$$R_{AA}(b;p_T) = \frac{dN^{AA}/dp_T}{N_{\rm coll}(b)\ dN^{NN}/dp_T}\ , \tag{1.13}$$

where $N_{\rm coll}(b)$ is number of binary collisions for a given impact parameter, b. The relation between $N_{\rm coll}$ and b will be worked out in Section V.B.1. The production of hard probe (high p_t, large mass) particles usually scales with $N_{\rm coll}(b)$, implying R_{AA}=1 if there are no medium induced modifications. For soft particles R_{AA} is usually less than 1 because the production of these particles scales with number of participant nucleons, $N_{\rm part}(b)$. ($N_{\rm part}(b)$ is smaller than $N_{\rm coll}(b)$ in A-A collisions).

One of the key measurements of hard probes at RHIC is the observation of "jet-quenching" [15] for high p_t particles. A jet is a narrow cone of hadrons produced by the hadronization of a high momentum parton. If these partons traverse the QGP they are expected to undergo collisional and medium-induced radiational energy loss. The energy loss will be reflected in the suppression of high p_t hadron multiplicities. The data on π^0 production in central Au+Au collisions at RHIC have shown a large suppression by a factor of 4-5 up to $p_t \simeq 20\,{\rm GeV}$, see Fig. 9. The attenuation of the

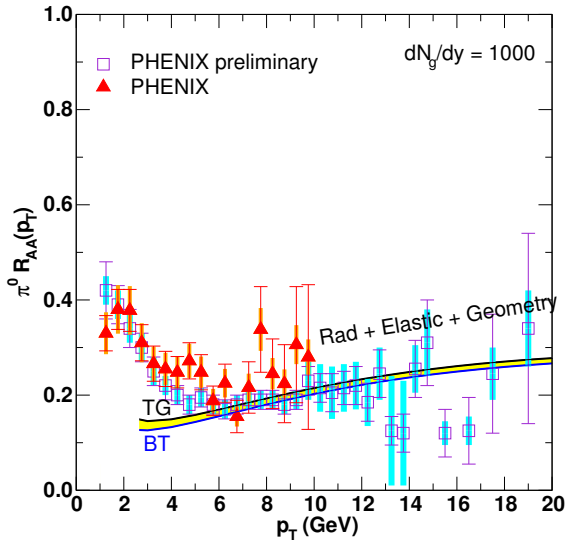

Fig. 9. $R_{AA}(p_t)$ ratio measured by PHENIX for neutral pions [12], compared to jet-quenching calculations [16].

parton energy allows one to extract the initial parton density in QGP in terms of the transport coefficient $\hat{q}$=Q^2/λ, which characterizes the (squared) momentum transfer per mean free path of the fast parton.

Another important hard probe is the heavy quark, which is expected to only partially thermalize in the medium considering its large mass and the limited fireball lifetime. One advantage of heavy quarks over high p_t light particles is that they are always distinguishable from bulk particles even if they are slowed down. Therefore the final heavy-quark (HQ) spectra may be taken as "witnesses" carrying a memory of the interaction history throughout the evolving fireball, by operating in between the limits of thermalization and free streaming.

Typical hard probe particles have only one "hard" scale characterized by their high energy, therefore they are not particularly sensitive to physics at the energy scale of medium temperature, T. However there exists one special hard probe particle which has an additional (softer) energy scale (on the order of T) making it very sensitive to

physics at the medium temperature. This probe is the charmonium.

D. Charmonium

A quarkonium is a bound state of a quark and its own antiquark. A quarkonium made of a pair of heavy quarks (c,b) is called heavy quarkonium. Heavy quarkonium includes charmonium ($c\bar{c}$) and bottomonium ($b\bar{b}$). The heaviest toponium does not exist because the top quark decays through the electroweak interaction (τ_t=$1/\Gamma_t \simeq$0.1fm/c) before a bound state can form. In this dissertation we focus on charmonium which can be rather abundantly produced at SPS and RHIC energies. The charmonium spectrum in vacuum is summarized in Fig. 10. Since only vector mesons can couple

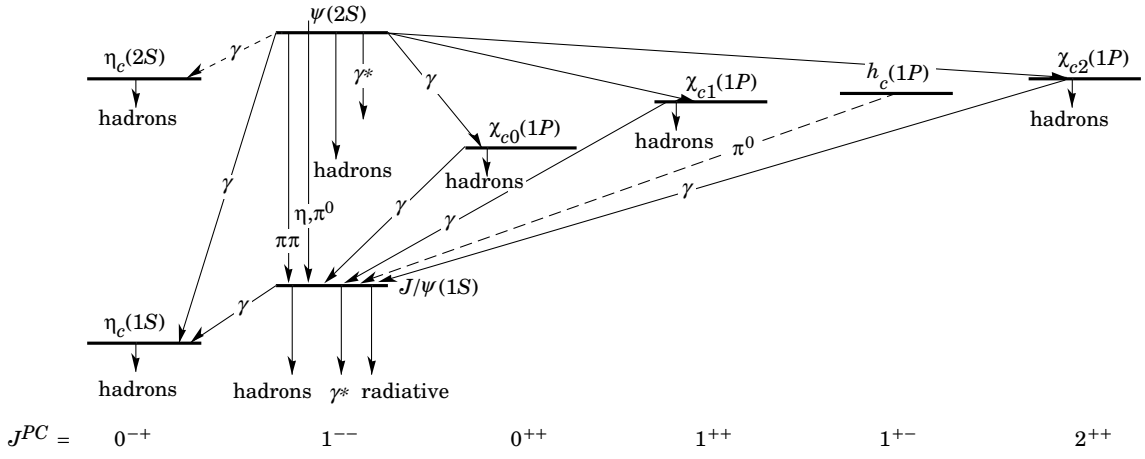

Fig. 10. Charmonium spectrum. Figure taken from Ref. [17].

to virtual photons and have dilepton as the decay product, which allow for quite accurate measurements, in this work we mainly focus on the productions of vector charmonium, such as, J/ψ and ψ'. However we keep in mind that 32% (8%) of observed J/ψ are from feeddown of $\chi_c(\psi')$ [18, 19], which happens at around 1000fm/c, much later than typical thermal medium lifetime ($\sim$10fm/c). Throughout

this dissertation we will use Ψ to denote J/ψ, χ_c and ψ'. The vacuum masses for J/ψ, χ_c and ψ' are $m_{J/\psi}$=3.1 GeV, $m_{\chi_{c0}}$=3.4 GeV, $m_{\chi_{c1}}$=3.5 GeV, $m_{\chi_{c2}}$=3.55 GeV and $m_{\psi'}$=3.7 GeV [17].

Unlike light quarkonium states the heavy quarks move inside the heavy quarkonium with a speed significantly smaller than the speed of light, with, *e.g.*, $\langle v^2/c^2\rangle \sim$0.25 for J/ψ [20]. As a result the heavy quark bound system can be described with non-relativistic Schroedinger approach with static heavy quark potentials, in a similar way of describing, *e.g.*, the hydrogen atom. An early ansatz yet successful in describing the charmonium spectrum is the Cornell-potential [21, 22],

$$V(r;T=0) = -\frac{4}{3}\frac{\alpha_s}{r} + \sigma r \ , \tag{1.14}$$

with $\alpha_s \simeq$0.35 and $\sigma \simeq$1 GeV/fm [23]. The first term corresponds to a Coulombic part which originates from one-gluon exchange and is dominant at small distance (r), the second term linear in r reflects the confining interaction.

As mentioned in the previous section, aside from its large mass, the charmonium has another characteristic energy scale, which is its binding energy ϵ_B. The charmonium binding energy is usually counted as the difference between the charmonium mass and the open-charm threshold,

$$\epsilon_B^0 = 2m_D - m_\Psi \ , \tag{1.15}$$

with $m_D \simeq$1.87 GeV. In vacuum the $D\bar{D}$ pair is usually considered as the open charm threshold for charmonium states. The charmonium states typically have binding energies of the order of several hundred MeV, e.g., $\epsilon_B^{J/\psi}$=640MeV, which is on the the same order of typical medium temperatures at URHICs.

If a charmonium is put inside the deconfined QGP medium the color force between c and $\bar{c}$ is subject to screening by the surrounding colored partons, see Fig. 11,

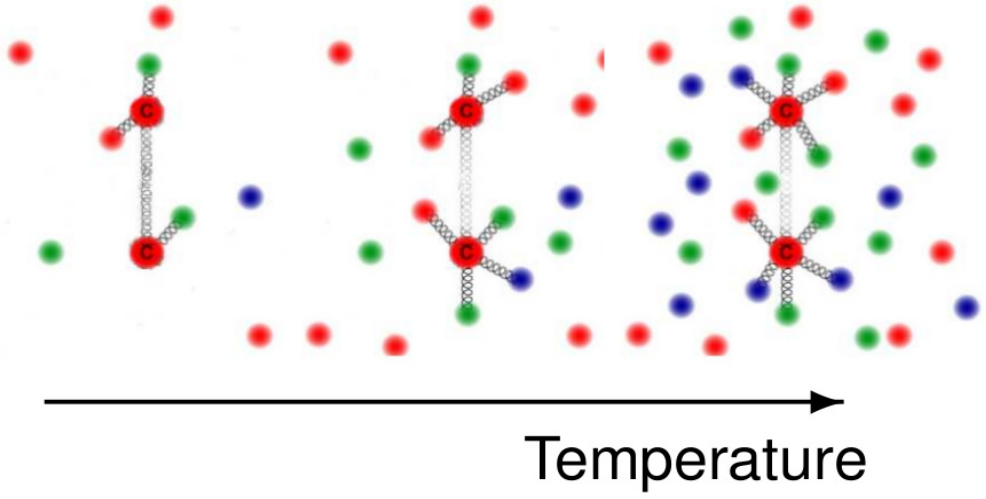

Fig. 11. Schematic representation of color-Debye screening in a deconfined medium.

in a way similar to screening of the electric field in dielectric materials: The $c(\bar{c})$ quark attracts partons in the medium with opposite color charge and forms the "Debye cloud" which screens the color electric field of the $c(\bar{c})$ quark. The screening effect in the Coulombic part of the Cornell potential can be evaluated with thermal perturbative QCD (pQCD). In the confining parts it is usually described by a phenomenological ansatz in early calculations, leading to the following form of the screened Cornell potential at finite temperature [24],

$$V_{\bar{Q}Q}(r;T) = \frac{\sigma}{\mu_D(T)}\left(1 - \mathrm{e}^{-\mu_D(T)r}\right) - \frac{4\alpha_s}{3r}\,\mathrm{e}^{-\mu_D(T)r}\ . \tag{1.16}$$

A direct consequence of the color Debye-screening is the lowering of charmonium binding energies, see Fig. 12. According to thermal pQCD calculations the Debye mass is related to the temperature of the medium,T, via

$$\mu_D(T) \sim gT. \tag{1.17}$$

Here g is the strong coupling constant. Inserting g ∼2 (corresponding to α_s ∼0.3),

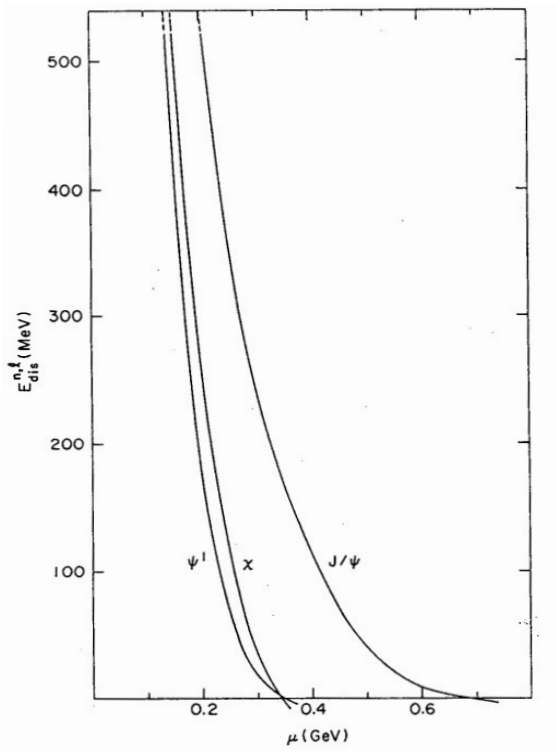

Fig. 12. Charmonium binding energies as a function of Debye mass. They are estimated from Eq. (1.16). Figure taken from [24].

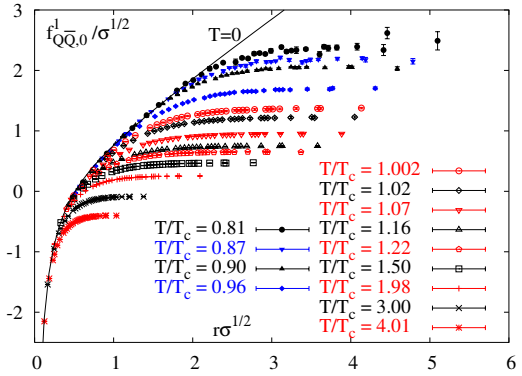

Fig. 13. Free energy of a static $c\bar{c}$ pair, as computed in lattice QCD [25].

we see that above a temperature of $T \sim 350$MeV the J/ψ is not bound any more and is expected to dissolve into separate c and $\bar{c}$ quarks. Based on this mechanism J/ψ suppression was first suggested in 1986 as a signature of QGP [26]. Similar phenomena are expected for the excited charmonium states, such as ψ' and χ_c. Their smaller binding energies imply lower dissociation temperatures. Therefore the entire charmonium spectra could provide a "thermometer" for the matter created in heavy-ion collisions.

Recently[1] quantitative lQCD computations of the free energy, $F_{Q\bar{Q}}(r;T)$, of a static heavy quark pair at finite temperatures, became available [25, 27], see Fig. 13. This has been used as the main input for recent potential models. However, it remains controversial to date whether the free energy or the internal energy,

$$U_{Q\bar{Q}}(r;T) = F_{Q\bar{Q}}(r;T) - T\frac{\partial F_{Q\bar{Q}}(r;T)}{\partial T} \ , \tag{1.18}$$

or any combination thereof, should be identified with a static $Q\bar{Q}$ potential at finite temperature, T. Usually the internal energy leads to stronger binding than the free-energy. We refer to the former ($V_{Q\bar{Q}} = U_{Q\bar{Q}}$) and latter ($V_{Q\bar{Q}} = F_{Q\bar{Q}}$) as strong- and

[1]The discussions in this and next paragraph mostly follow Ref. [28].

weak-binding scenario, respectively.

Further progress in thermal lQCD came with the computation of two-point correlation functions of a quarkonium current, j_α, with hadronic quantum number α,

$$G_\alpha(\tau,\vec{r}) = \langle\langle j_\alpha(\tau,\vec{r}) j_\alpha^\dagger(0,\vec{0})\rangle\rangle \ , \tag{1.19}$$

as a function of imaginary (euclidean) time, τ (also called temporal correlator). The imaginary part of the Fourier transform of the correlation function, $G_\alpha(\tau,\vec{r})$, is commonly referred to as the spectral function,

$$\sigma_\alpha(\omega,p) = -\frac{1}{\pi}\mathrm{Im}G_\alpha(\omega,p) \ , \tag{1.20}$$

which is related to the temporal correlator via

$$G_\alpha(\tau,T) = \int_0^\infty d\omega \sigma_\alpha(\omega,T) K(\omega,\tau,T) \tag{1.21}$$

with the finite-T kernel

$$K(\omega,\tau,T) = \frac{\cosh[(\omega(\tau-1/2T)]}{\sinh[\omega/2T]} \ . \tag{1.22}$$

Lattice QCD results for two-point correlation functions are usually normalized to a "reconstructed" correlator evaluated with the kernel at temperature T,

$$G_\alpha^{\mathrm{rec}}(\tau,T) = \int_0^\infty d\omega \ \sigma_\alpha(\omega,T^*) \ K(\omega,\tau,T) \ , \tag{1.23}$$

but with a spectral function at low temperature, T^*, where no significant medium effects are expected. The correlator ratio,

$$R_\alpha(\tau,T) = G_\alpha(\tau,T)/G_\alpha^{\mathrm{rec}}(\tau,T) \ , \tag{1.24}$$

is then an indicator of medium effects in $G_\alpha(\tau,T)$ through deviations from one. Current lQCD calculations find that the correlator ratio, $R_\alpha(\tau,T)$, in the pseudoscalar

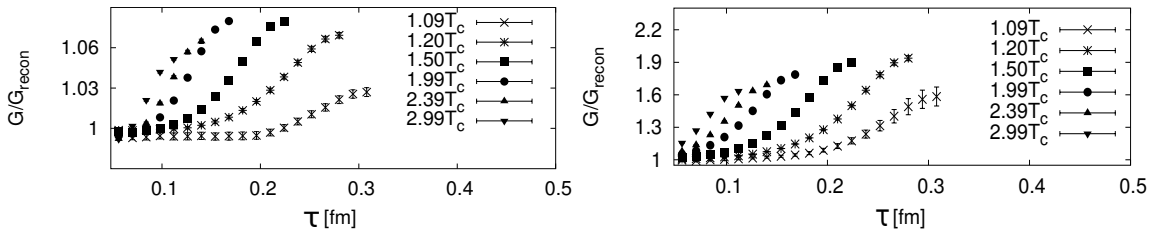

Fig. 14. Charmonium correlator ratio in the vector (left panel) and scalar (right panel) channel as computed in lattice QCD [29].

(η_c) and vector (J/ψ) channel are close to 1 (within ca. 10%) at temperatures up to 2-3 T_c [29, 30, 31], see the left panel of Fig. 14. In the P-wave channels (scalar and axialvector) the correlators ratios are substantially enhanced over 1 at large τ, see the right panel of Fig. 14. This feature is believed to be due to "zero-mode" contributions (at ω=0) which are related to the scattering of a charm (or anti-charm) quark, $c \to c$ (or $\bar{c} \to \bar{c}$), rather than to $c\bar{c}$ bound-state properties [32]. This interpretation is supported by studies of the τ-derivative of P-wave correlator ratios, which exhibits a much smaller variation (in the limit that the zero-mode part is a δ-function, $\sigma_{\rm zm}(\omega) \propto \delta(\omega)$, its contribution to the temporal correlator is a constant) [33, 34].

In principle, the in-medium properties of charmonia, such as pole mass, in-medium width and dissociation temperature, are fully encoded in their spectral function. However, the finite number of data points for the two-point correlator computed in lQCD severely hampers the inversion of the transform in Eq. (1.21), rendering the determination of the spectral function difficult, although various attempts are made, such as the Maximum Entropy Method (MEM) [35].

Although associated with large uncertainties, these lQCD data suggest that the J/ψ bound states might still survive above the critical temperature. As a consequence the c and $\bar{c}$ pairs produced in initial hard collisions may coalesce and regenerate J/ψ in QGP [36, 37], rendering the original picture with J/ψ suppression as the signal

of QGP more complicated. Quantitative calculations disentangling primordial J/ψ production and regeneration are thus necessary for utilizing J/ψ to assess the basic properties of the hot and dense medium created in URHICs. These constitute the main part of this dissertation.

E. Outline of Dissertation

In Chapter II we first give an overview of the physical processes related to charmonium production in each stage of heavy-ion collisions. Then we introduce our main framework: the Boltzmann transport equation approach. The Boltzmann transport equation describes the time evolution of the charmonium phase space distribution function due to dissociation, regeneration and drifting. If one is only interested in the inclusive yield of charmonium the Boltzmann transport equation can be reduced to a simpler rate-equation. Next we discuss the important relation between the dissociation rate and the regeneration rate, which is the principle of detailed balance. We discuss its microscopic origin and show its connection with the equilibrium limit of the charmonium phase distribution. We also examine the experimental fact that the c and $\bar{c}$ are always produced in pair and discuss its consequence on the charmonium regeneration. Finally we consider the correlation between the c and $\bar{c}$ in coordinate space and estimate its influence on charmonium regeneration.

In Chapter III we discuss the microscopic interaction between the charmonium states and the hot medium. In the QGP we calculate the dissociation rates from a "quasifree" mechanism with realistic charmonium in-medium binding energies estimated from lQCD potentials. We work out the momentum dependence of the dissociation rates. Based on the detailed balance we calculate and compare the charmonium regeneration rates with different input charm-quark momentum spectra ranging from

the hard pQCD spectra to the thermal spectra. With the in-medium width of charmonia estimated from "quasifree" dissociation rates we construct a model spectral function and calculate the correlator ratios. By comparing these ratios with lQCD data we extract the Ψ dissociation temperatures, which determine the start time of the regeneration process in the kinetic approach.

In Chapter IV we present our description of the space-time evolution of a heavy-ion collision, which is modeled by an isentropically and cylindrically expanding fireball with input parameters determined from the observed hadro-chemistry and the collective flow velocities. The resulting thermal evolution scenario is in line with basic features of hydrodynamic calculations. In particular we extend the fireball description to lower energies, which will be explored by future FAIR experiments. In this regime it turns out that, despite the low initial temperature, the deconfined phase still lasts for about 4fm/c, with a notable reheating process in the mixed phase driven by the latent heat. Finally, based on the flow field of the fireball model, we estimate the transverse momentum spectra of locally thermalized charmonia.

In Chapter V we estimate the charmonium phase space distribution at the moment of thermalization which serves as the initial condition of the Boltzmann transport equation. We discuss the primordial production of charmonium in initial nucleon-nucleon collisions and its subsequent interaction with the pre-equilibrium medium. Emphases are placed on the deviation of primordial charmonium production in nucleus-nucleus (A+A) from scaled p+p due to the so-called cold nuclear matter (CNM) effects.

In Chapter VI we present the numerical results of our model of charmonium production in heavy-ion collisions. We introduce the procedure of applying the kinetic equations to calculate charmonium production in the strong and weak binding scenarios. We first compare our results for both inclusive J/ψ yields and their trans-

verse momentum spectra with data at SPS and RHIC. Within current theoretical uncertainties we find that both scenarios can reproduce SPS and RHIC data for the centrality dependence of inclusive J/ψ production reasonably well. However the partition of primordial and regeneration yields is quite different in the two scenarios: the former dominates for strong binding, while for weak binding regeneration largely prevails at RHIC energies (except for peripheral collisions). This difference entails the strong binding scenario to be slightly favored by the p_t data. We also study the effects specifically relevant for high p_t J/ψ production, including formation time effects and B-meson feeddown. These effects lead to a moderate enhancement of J/ψ R_{AA} at high p_t. Then we explicitly evaluate J/ψ regeneration from different input charm-quark spectra. Next we compare the results of ψ' to ψ ratio to experimental data at SPS and provide the prediction of χ_c and ψ' production at RHIC. Last we present our prediction for charmonium production at FAIR energies.

We conclude in Chapter VII and give a few directions along which we plan to expand the work undertaken in this dissertation. The input charm-quark phase space distribution based on Langevin simulations, hydrodynamic simulations of the medium evolution as well as a microscopic model for primordial $c\bar{c}$ and charmonium production need to be implemented to improve charmonium toward a more quantitative probe of the hot and dense QCD matter.

CHAPTER II

CHARMONIUM TRANSPORT THEORY

In this chapter we discuss the main framework in which charmonium production in heavy-ion collisions is studied. In Section II.A we start with an overview of charmonium production in different stages of heavy-ion collisions and relevant production/dissociation mechanisms in each stage. In Section II.B we introduce the Boltzmann transport equation to describe the evolution of charmonium phase space distribution functions. The Boltzmann transport equation plays a central role in our framework. Finally we investigate constraints imposed by the pair production of charm-anticharm quarks and study their influence on charmonium regeneration in Section II.C.

A. Overview of Charmonium Production in Relativistic Heavy-Ion Collisions

The conventional picture of charmonium (Ψ=J/ψ, χ_c, ψ') production in heavy-ion collisions involves three stages: 1) Hard production stage: The two ultra-relativistically moving nuclei collide with each other and charm quark pairs are created from the hard collisions between partons. This is a fast process due to the rather large momentum transfer ($\sim$ $2m_c$=2.5GeV) involved. The typical time scale is estimated as $\tau \sim \frac{1}{2m_c} \sim 0.1$ fm/c. 2) Pre-equilibrium stage: If the charm and anti-charm quarks produced in initial hard collisions are sufficiently close to each other in phase space they can further develop into a charmonium state through non-perturbative interactions. The charmonium formation processes are rather slow compared to the charm quark production processes. The typical estimates for the charmonium formation time are $\sim$1 fm/c [20]. In the mean time the partons created in initial hard collisions rescatter and are in the process of thermally equilibrating. When the "pre-

charmonium" $c\bar{c}$ pairs travel in this medium some of them may collide with passing-by nucleons and be subsequently dissociated. The process is usually called "nuclear absorption", which will be discussed in more detail in Chapter V. The overall duration of the pre-equilibrium stage is estimated to be about $0.3 - 1.0\text{fm}/c$ depending on the center-of-mass energy of the collision. 3) Equilibrium stage: When the medium reaches thermal equilibrium, it is supposed to be either in the deconfined Quark-Gluon Plasma (QGP) phase, if the energy deposited in heavy-ion collision is large enough, or otherwise in the hadronic gas (HG) phase. The medium continues to expand and cool until it becomes so dilute that the particles in it stop interacting with each other. This moment is usually called "freeze-out", which signifies the end of the entire evolution of the medium. After "freeze-out" the produced particles stream freely to the detectors with their yields and transverse momentum spectra fixed at the moment of "freeze-out". The lifetime of the thermal medium depends largely on initial energy densities of the medium. Typically it lasts for about $10(12)\text{fm}/c$ for central Pb+Pb (Au+Au) collisions at SPS (RHIC). The description of the thermal medium will be detailed in Chapter IV. In the equilibrium stage there exist two competing effects on the charmonium abundance: On the one hand charmonia undergo inelastic collisions with particles in the thermal bath and are subsequently destroyed, on the other hand the charm quarks or D mesons in the medium may recombine and regenerate charmonia. Since these two competing processes are inverse processes of each other, their relative strength is governed by the principle of detailed balance which ensures that the charmonium abundances approach their thermal equilibrium values. The rates of approaching equilibrium strongly depend on the temperature and particularly the effective degrees of freedom, *i.e.*, the phase, of the medium. In QGP, both the significantly reduced Ψ binding energies (due to color-Debye screening) and the thermal parton density (due to the large color degeneracy) lead to dissociation/regeneration

rates much larger than those in HG phase.

B. Boltzmann Transport Equation

1. General Setup

The charmonia in the thermal medium form a system off thermodynamic equilibrium. The Boltzmann transport equation is an ideal tool for studying such a system. In this work we employ the Boltzmann transport equation to describe the time evolution of the charmonia phase space distribution function $f_\Psi(\vec{p},\vec{x},t)$ in the thermal medium [38, 39, 40, 41, 42],

$$\partial f_\Psi/\partial t + \vec{v}_\Psi \cdot \vec{\nabla} f_\Psi = -\alpha_\Psi f_\Psi + \beta_\Psi \ . \tag{2.1}$$

Here, the distribution function $f_\Psi(\vec{x},\vec{p},t)$ is the number of charmonia ($\Psi = J/\psi, \chi_c, \psi'$) per unit phase space volume at a given time t,

$$f_\Psi(x,p,t) = \frac{(2\pi)^3 dN_\Psi}{d^3x\, d^3p} \ . \tag{2.2}$$

The first term on the left-hand side of Eq. (2.1) describes the rate of change of the charmonium distribution function at a specific position in the phase-space. The second (drift) term reflects the charmonium diffusion from one position to another with velocity $\vec{v}_\Psi = \vec{p}/\sqrt{p^2+m_\Psi^2}$. Since the mass of Ψ is much larger than typical medium temperature ($m_\Psi \gg T$) we neglect the elastic scattering between Ψ and the medium and assume the Ψ to move on a straight line. Therefore the left-hand side of Eq. (2.1) represents the change of charmonium density other than charmonium diffusion. Other than diffusion the change in Ψ distribution function can only be due to the dissociation and regeneration of charmonia, which are accounted for by the first ("loss") and second ("gain") term on the right-hand side, respectively. The loss term consists of the product of the charmonium phase space density and its dissociation

rate, $\alpha_\Psi(\vec{p},\vec{x})$. The gain term, $\beta_\Psi(\vec{p},\vec{x})$, reflects the charmonium regeneration rate from charm quark coalescence.

One of the premises of Boltzmann transport equation is that the medium should be "dilute" enough so that a subsequent collision occurs well after the end of the first one (no quantum interference between successive collisions). The typical duration for one collision can be estimated by the reciprocal of the virtuality, $\sqrt{Q^2-m_\Psi^2}$, of the Ψ after scattering with thermal particles, which can be estimated as follows: Denote the four momentum of the Ψ before a collision as $(p^2/(2m_\Psi)+m_\Psi,\vec{p})$, and the four momentum of a thermal parton as $(k,\vec{k})$ with $k{=}|\vec{k}|$. Then the four momentum of Ψ after scattering becomes $(q_0,\vec{q}){=}(p^2/(2m_\Psi)+m_\Psi+k,\vec{p}+\vec{k})$. The virtuality is given by

$$\begin{aligned} Q^2-m_\Psi^2 = q_0^2-\vec{q}^2-m_\Psi^2 &= \left(\frac{p^2}{2m_\Psi}+m_\Psi+k\right)^2-(\vec{p}+\vec{k})^2-m_\Psi^2 \\ &= 2m_\Psi k-2\vec{p}\cdot\vec{k}+\frac{p^2k}{m_\Psi}+\frac{p^4}{4m_\Psi^2}\ . \end{aligned} \tag{2.3}$$

Assuming thermal momenta for Ψ and the parton, so that $p^2/(2m)\sim T$, $p\sim\sqrt{m_\Psi T}$, $k\sim T$, the virtuality $\sqrt{Q^2-m_\Psi^2}$ to leading order in $m_\Psi(\gg T)$ is on the order of $\sqrt{m_\Psi T}$. Therefore with a typical charmonium mass $\sim$3 GeV and a typical temperature $T\sim 0.3$GeV, the estimated duration for a dissociation process is around 0.2fm/c. On the other hand the typical Ψ dissociation rate at RHIC energy is on the order of 100MeV, as will be evaluated in Section III.B, corresponding to an average time of 2fm/c between successive collisions. Therefore the average interval between Ψ inelastic collisions is indeed much longer than typical collision time thus satisfying the premise of Boltzmann transport equation.

We proceed to work out the microscopic expression for the dissociation and gain rates, α_Ψ and β_Ψ. From now on we will omit the vector sign "$\vec{}$" on top of x

and p if no ambiguity arises. For simplicity let us first consider a 2-body dissociation/regeneration process, *e.g.*, $\Psi + g \leftrightarrows c + \bar{c}$, in which a Ψ scatters with a gluon and is subsequently dissociated into a $c\bar{c}$ pair. The dissociation rate is expressed as follows:

$$\alpha_\Psi(p,x) = \frac{1}{2E_\Psi}\int d\Phi_1(p_g)\; d\Phi_2(p_c,p_{\bar{c}}) \\ \times (2\pi)^4\delta^{(4)}(p_c+p_{\bar{c}}-p-p_g)\, d_g\, f_g(p_g)\, |\overline{\mathcal{M}_{\Psi g\to c\bar{c}}(s,t)}|^2 \;, \tag{2.4}$$

where $E_\Psi = \sqrt{p^2+m_\Psi^2}$ is the charmonium energy,

$$d_g f_g(p_g) = \frac{(2\pi)^3 dN_g}{d^3x\, d^3p_g} \tag{2.5}$$

is the gluon phase space distribution function with d_g=16 being the color-spin degeneracy factor for gluons, and $|\overline{\mathcal{M}_{c\bar{c}\to\Psi g}(s,t)}|^2$ is the transition matrix element between the initial state, $\Psi + g$, and the final state, $c + \bar{c}$, as a function of $s = (p + p_g)^2$ and $t = (p - p_c)^2$. The "bar" on top of $|\mathcal{M}|^2$ stands for summing over color and spin degeneracies of final states and averaging over color and spin degeneracy of initial states, *e.g.*, $|\overline{\mathcal{M}_{\Psi g\to c\bar{c}}}|^2$=$\Sigma|\mathcal{M}_{\Psi g\to c\bar{c}}|^2/(d_g d_\Psi)$, with d_g and d_Ψ being color and spin degeneracies of the gluon and the charmonium. The $\Sigma|\mathcal{M}_{\Psi g\to c\bar{c}}|^2$ denotes the transition matrix element with both initial and final state degeneracy summed over. In Eq. (2.4) $d\Phi_1(p_g)$ and $d\Phi_2(p_c,p_{\bar{c}})$ are Lorentz invariant 1-body and 2-body phase space integration measures,

$$d\Phi_1(p_g) = \frac{d^3p_g}{(2\pi)^3 2E_g}\;, \tag{2.6}$$

$$d\Phi_2(p_c,p_{\bar{c}}) = \frac{d^3p_c}{(2\pi)^3 2E_c}\frac{d^3p_{\bar{c}}}{(2\pi)^3 2E_{\bar{c}}}\;, \tag{2.7}$$

where E_g, E_c and $E_{\bar{c}}$ are the gluon, c and $\bar{c}$ energies, respectively.

It is convenient to express the dissociation rate α_Ψ in terms of the charmonium

dissociation cross section σ_Ψ, which can be expressed in terms of the transition probability, $|\overline{\mathcal{M}_{c\bar{c}\to\Psi g}}|^2$, as follows,

$$\sigma_\Psi(s) = \frac{1}{2E_\Psi}\int d\Phi_2(p_c,p_{\bar{c}})(2\pi)^4\delta^{(4)}(p_c+p_{\bar{c}}-p-p_g)\frac{1}{2E_g|v_\Psi-v_g|}|\overline{\mathcal{M}_{\Psi g\to c\bar{c}}(s,t)}|^2 \ , \tag{2.8}$$

where $v_\Psi = p/\sqrt{p^2+m_\Psi^2}$ and $v_g = p_g/\sqrt{p_g^2+m_g^2}$ are the velocities of the charmonium and gluon, respectively. By comparing Eq. (2.8) with Eq. (2.4) one can identify the relation between α_Ψ and σ_Ψ,

$$\alpha_\Psi(p,x) = \int \frac{d^3p_g}{(2\pi)^3}\, d_g\, f_g(p_g)\, v_{rel}\, \sigma_\Psi(s) \ , \tag{2.9}$$

where v_{rel}=$|v_\Psi - v_g|$ is the relative velocity between the gluon and the charmonium.

Next we proceed to the microscopic expression of the gain rate, β_Ψ, given by

$$\begin{aligned}\beta_\Psi(p,x) = \frac{1}{2E_\Psi}\int & d\Phi_1(p_g)d\Phi_2(p_c,p_{\bar{c}})(2\pi)^4\delta^{(4)}(p_c+p_{\bar{c}}-p-p_g) \\ & \times|\overline{\mathcal{M}_{c\bar{c}\to\Psi g}(s,t)}|^2\, d_c\, f_c(p_c)\, d_{\bar{c}}\, f_{\bar{c}}(p_{\bar{c}})\,(1+f_g(p_g)) \ ,\end{aligned} \tag{2.10}$$

where $d_c f_c(p_c)$ and $d_{\bar{c}} f_{\bar{c}}(p_{\bar{c}})$ are charm and anti-charm phase space distribution functions,

$$d_c f_c(p_c) = \frac{(2\pi)^3 dN_c}{d^3x\, d^3p_c} \ , \tag{2.11}$$

with d_c=$d_{\bar{c}}$=6 being the color-spin degeneracy factors for c and $\bar{c}$, respectively. The factor of $1+f_g(p_g)$ is the Bose-enhancement factor for the final state gluon. The "bar" on top of $|\overline{\mathcal{M}_{c\bar{c}\to\Psi g}}|$ denotes summing over final states and averaging over the initial states, $|\overline{\mathcal{M}_{c\bar{c}\to\Psi g}}|$=$\Sigma|\mathcal{M}_{c\bar{c}\to\Psi g}|/(d_c d_{\bar{c}})$. We note that the underlying dynamics of the transition between $g+\Psi$ and $c+\bar{c}$, QCD, is time-reversal symmetric, therefore the transition probability satisfies the principle of detailed balance as

$$\Sigma|\mathcal{M}_{c\bar{c}\to\Psi g}|^2 = \Sigma|\mathcal{M}_{\Psi g\to c\bar{c}}|^2 \ . \tag{2.12}$$

It is straightforward to extend the above expressions for the dissociation and gain rates to 2-to-3 processes, $i + \Psi \to i + c + \bar{c}$ (i=g,q,$\bar{q}$) and its inverse 3-to-2 processes, $i+c+\bar{c} \to i+\Psi$. What needs to be modified are: 1) Replacing the 2-body integration measures in Eqs. (2.4), (2.8) and (2.10) by 3-body integration measures,

$$d\Phi_3(p_c, p_{\bar{c}}, \bar{p}_i) = \frac{d^3p_c}{(2\pi)^3 2E_c}\frac{d^3p_{\bar{c}}}{(2\pi)^3 2E_{\bar{c}}}\frac{d^3\bar{p}_i}{(2\pi)^3 2E_i} \ , \tag{2.13}$$

accounting for the phase space of the extra light parton in the final state of dissociation (or the initial state of regeneration), 2) Inserting the four-momentum of the extra light parton into the 4-momentum conserving delta function. 3) Supplying the phase space distribution function, $d_i f_i(\bar{p}_i)$, for the extra parton if it appears in the initial state or the Bose-enhancement/Pauli-blocking factors, $1 \pm f_i(\bar{p}_i)$, if it appears in the final state. The "$\pm$" takes $+(-)$ for $i = g$ ($i = q, \bar{q}$). The explicit expressions of σ_Ψ, α_Ψ and β_Ψ for two-to-three processes are

$$\begin{aligned}\sigma_\Psi(s) = &\frac{1}{2E_\Psi}\sum_i \int d\Phi_3(p_c, p_{\bar{c}}, \bar{p}_i)(2\pi)^4\delta^{(4)}(p_c + p_{\bar{c}} + \bar{p}_i - p - p_i) \\ &\times \frac{1}{2E_g|v_\Psi - v_i|}|\overline{\mathcal{M}_{\Psi i\to c\bar{c}i}(s,t)}|^2(1 \pm f_i(\bar{p}_i)) \ ,\end{aligned} \tag{2.14}$$

$$\begin{aligned}\alpha_\Psi(p,x) = &\frac{1}{2E_\Psi}\sum_i \int d\Phi_1(p_i)\Phi_3(p_c, p_{\bar{c}}, \bar{p}_i)(2\pi)^4\delta^{(4)}(p_c + p_{\bar{c}} + \bar{p}_i - p - p_i) \\ &\times |\overline{\mathcal{M}_{\Psi i\to c\bar{c}i}(s,t)}|^2 \, d_i \, f_i(p_i) \, (1 \pm f_i(\bar{p}_i)) \ ,\end{aligned} \tag{2.15}$$

$$\begin{aligned}\beta_\Psi(p,x) = &\frac{1}{2E_\Psi}\sum_i \int d\Phi_1(p_i)d\Phi_3(p_c, p_{\bar{c}}, \bar{p}_i)(2\pi)^4\delta^{(4)}(p_c + p_{\bar{c}} + \bar{p}_i - p - p_i) \\ &\times |\overline{\mathcal{M}_{c\bar{c}i\to\Psi i}(s,t)}|^2 \, d_c \, f_c(p_c) \, d_{\bar{c}} \, f_{\bar{c}}(p_{\bar{c}}) \, d_i \, f_i(\bar{p}_i) \, (1 \pm f_i(p_i)) \ .\end{aligned} \tag{2.16}$$

Here $\bar{p}_i$ denotes the momentum of the light parton for the three-body state (together with c and $\bar{c}$).

We will illustrate in Section III.C that in the case where the charmonium binding

energies are small compared to the medium temperature, a 3-to-2 regeneration process, $i+c+\bar{c} \to i+\Psi$ ($i = g, q, \bar{q}$), can be readily factorized into a 2-to-2 (perturbative) quasi-elastic scattering process, $i + c(\bar{c}) \to i + c'(\bar{c}')$ and 2-to-1 (non-perturbative) coalescence process, $c+\bar{c} \to \Psi$ owing to the different time scales for these two processes. The four-momentum is conserved for the entire 3-to-2 regeneration process.

So far we have established the connection between the charmonium transport equation and the microscopic dynamics of Ψ dissociation/regeneration. The required inputs from microscopic calculations are 1) The transition matrix element, $|\mathcal{M}_{ic\bar{c}\to\Psi i}|^2$; 2) Charmonium binding energies, ϵ_Ψ, which determine the initial state phase space for the dissociation processes and the final state phase space for the regeneration processes; 3) The in-medium charm quark spectra, $f_c(p_c)$, $f_{\bar{c}}(p_{\bar{c}})$, determining the charmonium regeneration rates. We will discuss these input quantities based on microscopic calculations in Chapter III. With all these quantities supplied by microscopic calculations we are ready to solve the Boltzmann transport equation (2.1).

The Boltzmann transport equation, Eq. (2.1), is a first-order, linear partial differential equation. It can be solved using the method of change of variables. Introducing the new variable

$$u = x - v_\Psi t \ ; \tag{2.17}$$

we have

$$f_\Psi(x,t) = f_\Psi(u + v_\Psi t, t) \ , \tag{2.18}$$

$$\alpha_\Psi(x,t) = \alpha_\Psi(u + v_\Psi t, t) \ , \tag{2.19}$$

$$\beta_\Psi(x,t) = \beta_\Psi(u + v_\Psi t, t) \ . \tag{2.20}$$

Since in Eq. (2.1) there is no derivative with respect to p, we consider p as a parameter and suppress its dependence in f_Ψ, α_Ψ, β_Ψ for the moment. Substituting Eq. (2.17)

into Eq. (2.1), we obtain

$$\partial f_\Psi(u+v_\Psi t,t)/\partial t = -\alpha_\Psi(u+v_\Psi t,t) f_\Psi(u+v_\Psi t,t) + \beta_\Psi(u+v_\Psi t,t) \ . \tag{2.21}$$

Now Eq. (2.21) is a first-order ordinary differential equation with u as a parameter. It has the following solution,

$$\begin{aligned} f_\Psi(u+v_\Psi t,t) = {} & f_\Psi(u+v_\Psi t_0,t_0) e^{-\int_{t_0}^{t} dt' \alpha_\Psi(u+v_\Psi t',t')} \\ & + \int_{t_0}^{t} dt' \beta_\Psi(u+v_\Psi t',t') e^{-\int_{t'}^{t} dt'' \alpha_\Psi(u+v_\Psi t'',t'')} \ . \end{aligned} \tag{2.22}$$

Finally we substitute Eq. (2.17) into Eq. (2.22) and obtain the solution for the Boltzmann transport equation.

$$\begin{aligned} f_\Psi(p,x,t) = {} & f_\Psi(p,x-v_\Psi(t-t_0),t_0) e^{-\int_{t_0}^{t} dt' \alpha_\Psi(p,x-v_\Psi(t-t'),t')} \\ & + \int_{t_0}^{t} dt' \beta_\Psi(p,x-v_\Psi(t-t'),t') e^{-\int_{t'}^{t} dt'' \alpha_\Psi(p,x-v_\Psi(t-t''),t'')} \ , \end{aligned} \tag{2.23}$$

where t_0 is the start time of the evolution. The initial phase space distribution of charmonia, $f_\Psi(p,x,t_0)$, is determined by initial hard production and cold nuclear matter effects, which are the main topic of Chapter V. The solution of the Boltzmann transport equation, Eq. (2.23), consists of two terms: The first term decays with time and describes the dissociation process of the initially produced charmonia. This component of the solution is usually referred to as the "primordial" component. The second term increases with time and describes the regeneration process of charmonia from coalescence of charm quarks in the medium. This component is referred to as the "regeneration" component.

2. Rate-Equation

If one is only interested in the inclusive yield of charmonia, N_Ψ, it is convenient to employ a rate-equation instead of the more differential Boltzmann equation. In this section we derive the widely employed rate-equation from the Boltzmann equation.

We start by integrating over the entire charmonium phase space on both sides of the Boltzmann equation (2.1). The left-hand side becomes

$$\begin{aligned}
&\int d^3x\,\frac{d^3p}{(2\pi)^3}\left(\partial f_\Psi(p,x,t)/\partial t + v_\Psi\cdot\nabla f_\Psi(p,x,t)\right)\\
&= \frac{\partial}{\partial t}\int d^3x\,\frac{d^3p}{(2\pi)^3} f_\Psi(p,x,t) + \int\frac{d^3p}{(2\pi)^3}\int d^3x\nabla\cdot\left(f_\Psi(p,x,t)v_\Psi\right)\\
&= dN_\Psi(t)/dt + \int\frac{d^3p}{(2\pi)^3}\oint_S d\vec{S}\cdot\left(f_\Psi(p,x,t)\vec{v}_\Psi\right)\\
&= dN_\Psi(t)/dt\ . \qquad (2.24)
\end{aligned}$$

In the second equality we used the definition of charmonium phase space distribution function, Eq. (2.2) and Gauss's law, where S is a large surface enclosing the integration volume of coordinate space. In the third equality we used the fact that the charmonium phase space distribution $f_\Psi(p,x,t)$ drops sufficiently fast as $|\vec{x}|\to\infty$. Next we proceed to the right-hand side, which consists of the loss and the gain terms. For the loss term, if spatial homogeneity is assumed, namely, $\alpha_\Psi(p,x,t)\to\alpha_\Psi(p,t)$, we have

$$\begin{aligned}
\int d^3x\,\frac{d^3p}{(2\pi)^3}\,\alpha_\Psi(p,x,t)f_\Psi(p,x,t) &= \int\frac{d^3p}{(2\pi)^3}\,\alpha_\Psi(p,t)\int d^3x\,f_\Psi(p,x,t)\\
&\approx \alpha_\Psi(\langle p\rangle,t)\int\frac{d^3p}{(2\pi)^3}\,d^3x\,f_\Psi(p,x,t)\\
&\approx \Gamma_\Psi(\langle p\rangle,t)N_\Psi(t)\ , \qquad (2.25)
\end{aligned}$$

where $\langle p\rangle$ is the average momentum of Ψ, and the $\alpha_\Psi(\langle p\rangle,t)$ is conventionally denoted as $\Gamma_\Psi(\langle p\rangle,t)$. Similar manipulations can be applied to the gain term. With the

assumption of spatial homogeneity the integration over coordinate space reduces to the multiplication with the volume of the medium (fireball), V_{FB}. The integration over charmonium momentum can also be performed. The resulting integrated gain term is conventionally denoted by $G_\Psi(t)$,

$$\begin{aligned} G_\Psi(t) &\equiv \int d^3x \frac{d^3p}{(2\pi)^3}\ \beta_\Psi(p,x,t) \\ &= V_{FB} \int \frac{d^3p}{(2\pi)^3}\ \beta_\Psi(p,t)\ . \end{aligned} \tag{2.26}$$

Putting Eqs. (2.24), (2.24) and (2.26) together we obtain the rate equation [43] describing the time-evolution of the inclusive charmonium yield,

$$\frac{dN_\Psi(t)}{dt} = -\Gamma_\Psi(t) N_\Psi(t) + G_\Psi(t)\ . \tag{2.27}$$

3. Equilibrium Limit

Let us consider the equilibrium limit of the solution of the Boltzmann transport equation, Eq. (2.1), which is defined by

$$f_\Psi^{\rm eq}(p) = \frac{\beta_\Psi(p)}{\alpha_\Psi(p)}\ , \tag{2.28}$$

where $f_\Psi^{\rm eq}(p)$, $\beta_\Psi(p)$ and $\alpha_\Psi(p)$ are also assumed to be homogeneous in space. It is easy to verify that the equilibrium distribution $f_\Psi^{\rm eq}(p)$ solves the Boltzmann equation. In this limit the (integrated) gain term in the rate-equation, G_Ψ, can be written in

terms of $f_\Psi^{\rm eq}(p)$ as

$$\begin{aligned} G_\Psi(t) &= V\int \frac{d^3p}{(2\pi)^3}\,\beta_\Psi(p,t) \\ &= V\int \frac{d^3p}{(2\pi)^3}\,\alpha_\Psi(p,t) f_\Psi^{\rm eq}(p) \\ &\approx \alpha_\Psi(\langle p\rangle,t) V\int \frac{d^3p}{(2\pi)^3} f_\Psi^{\rm eq}(p) \\ &= \Gamma_\Psi(t) N_\Psi^{\rm eq}(t)\ . \end{aligned} \tag{2.29}$$

Substituting Eq. (2.29) into Eq. (2.27), we obtain another common form of the rate-equation [44],

$$\frac{{\rm d}N_\Psi(t)}{{\rm d}t} = -\Gamma_\Psi(t)[N_\Psi(t) - N_\Psi^{\rm eq}(t)]\ . \tag{2.30}$$

This form is particularly convenient in the special case where the momentum spectra for both the charm-quark and the light partons are thermal. In this case the inclusive yield of charmonium in the equilibrium limit, $f_\Psi^{\rm eq}(p)$, is independent of the transition probability, $|\mathcal{M}|^2$. It is instructive to further discuss this special case.

For simplicity we first consider a 2-to-2 process, $\Psi + g \leftrightarrows c + \bar{c}$. We denote thermal (Boltzmann) charm-quark spectra as

$$f_c(p_c) = \gamma_c\, e^{-\sqrt{m_c^2+p_c^2}/T} = \gamma_c\, e^{-E_c/T}\ , \tag{2.31}$$

where γ_c is a charm quark fugacity reflecting its total yield deviating from chemical equilibrium (since $m_c \gg T$ we cannot expect charm quarks to reach chemical equilibrium). The gluons follow the thermal Bose distribution,

$$f_g(p_g) = \frac{1}{\exp\left(\frac{\sqrt{m_g^2+p_g^2}}{T}\right)-1} = \frac{1}{\exp\left(\frac{E_g}{T}\right)-1}\ , \tag{2.32}$$

where E_g is the energy of the gluon. Plugging these spectra into Eq.(2.10), we obtain

$$\begin{aligned}
\beta_\Psi(p) &= \frac{1}{2E_\Psi}\int d\Phi_1(p_g)d\Phi_2(p_c,p_{\bar{c}})(2\pi)^4\delta^4(p_c+p_{\bar{c}}-p-p_g) \\
&\qquad \times |\overline{\mathcal{M}_{c\bar{c}\to\Psi g})}|^2\, d_c\, f_c(p_c)\, d_{\bar{c}}\, f_{\bar{c}}(p_{\bar{c}})\,(1+f_g(p_g)) \\
&= \frac{\gamma_c^2 d_c^2}{2E_\Psi}\int d\Phi_1(p_g)d\Phi_2(p_c,p_{\bar{c}})(2\pi)^4\delta^4(p_c+p_{\bar{c}}-p-p_g) \\
&\qquad \times |\overline{\mathcal{M}_{c\bar{c}\to\Psi g}}|^2\, e^{-(E_c+E_{\bar{c}})/T}\,(1+f_g(p_g)) \\
&= \frac{\gamma_c^2 d_c^2}{2E_\Psi}\int d\Phi_1(p_g)d\Phi_2(p_c,p_{\bar{c}})(2\pi)^4\delta^4(p_c+p_{\bar{c}}-p-p_g) \\
&\qquad \times |\overline{\mathcal{M}_{c\bar{c}\to\Psi g}}|^2\, e^{-(E_\Psi+E_g)/T}\,(1+f_g(p_g)) \\
&= \frac{\gamma_c^2 d_\Psi}{2E_\Psi}\int d\Phi_1(p_g)d\Phi_2(p_c,p_{\bar{c}})(2\pi)^4\delta^4(p_c+p_{\bar{c}}-p-p_g) \\
&\qquad \times |\overline{\mathcal{M}_{\Psi g\to c\bar{c}}}|^2\, e^{-\sqrt{m_\Psi^2+p^2}/T}\, d_g\, f_g(p_g) \\
&= \gamma_c^2 d_\Psi e^{-\sqrt{m_\Psi^2+p^2}/T}\,\alpha_\Psi(p)\ , \qquad (2.33)
\end{aligned}$$

where in the third and fourth equality we used four-momentum conservation imposed by the 4-D δ-function, and an identity for the Bose-distribution for the gluon, $e^{-E_g/T}(1+f_g(p_g)) = f_g(p_g)$. In the fifth equality the detailed balance between $\Sigma|\mathcal{M}_{\Psi g\to c\bar{c}}|^2$ and $\Sigma|\mathcal{M}_{c\bar{c}\to\Psi g}|^2$, Eq. (2.12), and the definition of dissociation rate α_Ψ, Eq. (2.4), are used, The color-spin degeneracy factors for Ψ, gluon, c and $\bar{c}$ are d_Ψ=3, d_g=16, d_c=$d_{\bar{c}}$=6. Although this derivation is made for 2-to-2 processes, it is straightforward to verify that this relation also holds for 2-to-3 processes as long as the detailed balance and four-momentum conservation hold. Comparing Eq. (2.33) with Eq. (2.28), we obtain

$$f_\Psi^{\rm eq}(p) = \gamma_c^2 d_\Psi e^{-\sqrt{m_\Psi^2+p^2}/T}\ . \qquad (2.34)$$

This relation shows that as long as both charm quarks and light partons are in thermal equilibrium the regenerated charmonia have the thermal momentum spectra

as their equilibrium limit which does not depend on the microscopic details of the dissociation/regeneration mechanisms. Different microscopic transition mechanisms will only affect the transition rates, namely the speed with which charmonium spectra approach the equilibrium limit.

Since the thermal production and annihilation rates of $c\bar{c}$ are believed to be small in heavy-ion collisions at SPS and RHIC energies, $c\bar{c}$ pairs are assumed to be exclusively produced in primordial N+N collisions and conserved thereafter [36]. The charmonium equilibrium limit at a given time can be conveniently evaluated by solving the following charm conservation relation for γ_c,

$$\begin{aligned}\frac{N_{c\bar{c}}}{V} &= \frac{1}{2}\int \frac{d^3p_c}{(2\pi)^3}(f_c(p_c)+f_{\bar{c}}(p_{\bar{c}})) + \int \frac{d^3p}{(2\pi)^3} f_\Psi^{\rm eq}(p) \\ &= \gamma_c n_c^{\rm th} + \gamma_c^2 n_\Psi^{\rm th} \ , \end{aligned} \tag{2.35}$$

where $N_{c\bar{c}}$ is the total number of $c\bar{c}$ pairs from primordial production and, $n_c^{\rm th}$ and $n_\Psi^{\rm th}$ are thermal spatial densities for c and Ψ,

$$n_c^{\rm th} = d_c \int \frac{d^3p_c}{(2\pi)^3} e^{-\frac{\sqrt{m_c^2+p_c^2}}{T}} \ , \tag{2.36}$$

$$n_\Psi^{\rm th} = d_\Psi \int \frac{d^3p}{(2\pi)^3} e^{-\frac{\sqrt{m_\Psi^2+p^2}}{T}} \ . \tag{2.37}$$

This relation shows that in thermal equilibrium the partition of all charm quarks between the open-charm and charmonium states is solely determined by their respective masses and degeneracy factors [45].

We should keep in mind that the charmonium equilibrium limits have this nice feature only if the charm quark spectra are thermal, which, however, may not be the case in heavy-ion collisions, since charm quarks are heavy and take a rather long time to thermalize, compared to the typical lifetime of the medium (delayed by a factor of m_c/T compared to light partons). We will discuss more realistic charm quark spectra

and their implications for charmonium production in the medium in Chapter III.

C. c-$\bar{c}$ Correlations for Charmonium Production

1. Charmonium Production in the Canonical Ensemble

Before we finish this chapter and discuss the input to the kinetic equations from microscopic calculations we need to address another issue associated with Ψ regeneration. The problem originates from a simple experimental fact: The charm and anti-charm quarks are always produced in pairs. Its impact on charmonium production can be easily seen in a situation where few charm quark pairs are produced per event. For example, at SPS energy there is one charm quark pair produced every ten events in central Pb+Pb collisions, namely on average N_c=$N_{\bar{c}}$=0.1 per event. Accordingly one expects the average number of regenerated Ψ to be 1/10 of what we would get if there is one charm quark pair created in each event. However Eq. (2.10) naively suggests that the average number of regenerated Ψ is proportional to $N_c N_{\bar{c}}$=0.01, one hundredth of what we would get for the N_c=$N_{\bar{c}}$=1 case, an underestimate by a factor of 10! This example illustrates the importance of the correlation between charm and anti-charm production in charmonium regeneration.

To systematically solve this issue we employ the statistical description of charm quark pair production in a grand-canonical ensemble, where all thermodynamic properties of the charm pair system can be derived from its grand-partition function Z [46]. Let us start with the 1-body partition function (for 1 charm or anti-charm quark),

$$Z_1 = \gamma_c n_c^{\rm th} V_{FB} = \gamma_c \, V_{FB} \, d_c \int \frac{d^3 p_c}{(2\pi)^3} e^{-\sqrt{m_c^2+p_c^2}/T} \ , \tag{2.38}$$

where V_{FB} and T are the volume and temperature of the system, the charm quark fugacity γ_c is to account for the chemical off-equilibrium of charm quarks. $K_2(x)$ is

the modified Bessel function, $n_c^{\rm th}$ is the thermal density of charm quarks, defined in Eq. (2.36). The partition function with k charm quarks is

$$Z_k = \frac{Z_1^k}{k!} \ , \tag{2.39}$$

where $k!$ in the denominator results from the indistinguishability of k charm quarks. If we now impose the constraint that for each charm quark there exists its partner - anti-charm quark, we obtain the partition function for k charm pairs,

$$Z_k^{pair} = Z_k \cdot Z_k = \frac{Z_1^k}{k!}\frac{Z_1^k}{k!} \ . \tag{2.40}$$

The k (anti-)charm quarks are indistinguishable from each other, however the charm quarks are distinct from anti-charm quarks.

Next we sum over the contributions from arbitrary k pairs of charm quarks and obtain the grand-partition function Z, satisfying the constraint $N_c - N_{\bar{c}}$=0 for each individual event.

$$Z = \sum_{k=0}^{\infty} Z_k^{pair} = \sum_{k=0}^{\infty} \frac{Z_1^k Z_1^k}{k!k!} = I_0(2Z_1) \ , \tag{2.41}$$

where I_0 is the modified Bessel function. Sometimes such an ensemble is called "canonical ensemble". We keep in mind however that this canonicality is only referred to the strict constraint of the net charm number ($N_c - N_{\bar{c}}$ =0) rather than the "total" charm number, $N_c + N_{\bar{c}}$, which can still fluctuate event by event.

With grand-partition function obtained we are ready to evaluate average values over events (denoted by "$\langle\cdots\rangle$" in this section) of any thermodynamic quantity as

$$\langle\mathcal{O}\rangle \equiv \sum_{k=0}^{\infty} \mathcal{O}(k)P(k) \ , \tag{2.42}$$

where

$$P(k) = \frac{Z_k^{pair}}{Z} \ , \tag{2.43}$$

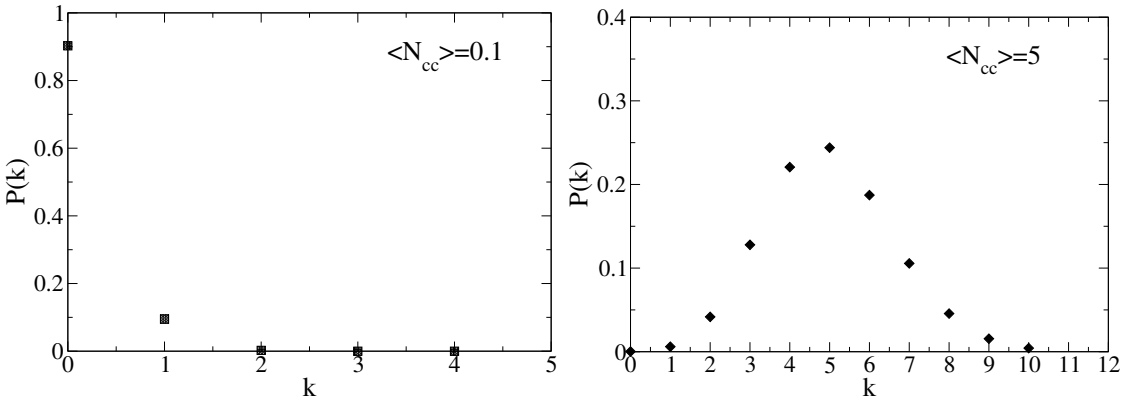

Fig. 15. The probability distribution of integer number (k) pairs of charm quarks in one event. Left panel: $\langle N_{c\bar{c}}\rangle$=0.1 corresponding to central Pb+Pb collisions (within Δy=1.8 around y=0) at SPS ($\sqrt{s}$=17.3AGeV). Right panel: $\langle N_{c\bar{c}}\rangle$=5.0, corresponding to central Au+Au collisions (within Δy=1.8 around y=0) at RHIC ($\sqrt{s}$=200AGeV).

is the probability of an event with an integer (k) number of pairs of charm quarks. For example, the average number of (open) charm pairs is

$$\langle N_{op}\rangle = \frac{1}{Z}\sum_{k=0}^{\infty} k Z_k^{pair} = Z_1 \frac{I_1(2Z_1)}{I_0(2Z_1)} \ . \tag{2.44}$$

Matching $\langle N_{op}\rangle$ to the experimentally measured $\langle N_{c\bar{c}}\rangle$ allows the determination of Z_1, Eq. (2.38) and therefore $P(k)$ (the number of the charmonium states in the system is numerically negligible compared to $\langle N_{op}\rangle$).

In central Pb+Pb collisions at SPS ($\sqrt{s}$=17.3AGeV) and in central Au+Au collisions at RHIC ($\sqrt{s}$=200AGeV) there are on average 0.1 and 5.0 charm-quark pairs produced in the rapidity window of Δy=1.8 around y=0 produced, respectively. The corresponding probability distributions $P(k)$ are shown in Fig. 15.

Eq. (2.23) states that the number of regenerated Ψ is proportional to the gain rate, β_Ψ, which, in turn, is proportional to the product of the charm and anti-charm quark phase space distribution, $f_c f_{\bar{c}}$. In events with exactly k pairs of charm quarks

produced, the regeneration component can be written as $N_\Psi^{\rm reg}(k) = k^2 N_1^{\rm reg}$, with $N_1^{\rm reg}$ being the number of Ψ regenerated from 1 $c\bar{c}$ pair. Therefore the average number of charmonia regenerated in the canonical ensemble over k is

$$\langle N_\Psi^{\rm reg}\rangle = \sum_{k=0}^{\infty} N_\Psi^{\rm reg}(k) P(k) = \frac{N_1^{\rm reg}}{I_0(2Z_1)} \sum_{k=0}^{\infty} k^2 Z_k^{pair} = N_1^{\rm reg} Z_1^2 \ . \tag{2.45}$$

Specifically, in the equilibrium limit we have

$$N_1^{\rm reg} = N_1^{\rm eq} = \gamma_{c(1)}^2 V_{FB} \int \frac{d^3p}{(2\pi)^3}\ d_\Psi e^{-\sqrt{m_\Psi^2+p^2}/T} = \gamma_{c(1)}^2 V_{FB} n_\Psi \ , \tag{2.46}$$

where $\gamma_{c(1)}$ satisfies

$$1 = \gamma_{c(1)} V_{FB} \int \frac{d^3p}{(2\pi)^3}\ d_c e^{-\sqrt{m_c^2+p^2}/T} = \frac{\gamma_{c(1)} Z_1}{\gamma_c} \ . \tag{2.47}$$

Substituting Eq. (2.47) into Eqs. (2.46) and (2.45) we obtain

$$\langle N_\Psi^{\rm eq}\rangle = N_1^{\rm eq} Z_1^2 = \gamma_c^2 V_{FB} n_\Psi \ . \tag{2.48}$$

With $\langle N_{op}\rangle$ and $\langle N_\Psi^{\rm eq}\rangle$ known we are ready to write down the charm conservation equation in the "canonical" ensemble [47],

$$\begin{aligned} \langle N_{c\bar{c}}\rangle &= Z_1 \frac{I_1(2Z_1)}{I_0(2Z_1)} + N_1^{\rm eq} Z_1^2 \\ &= \gamma_c n_c V_{FB} \frac{I_1(\gamma_c n_c V_{FB})}{I_0(\gamma_c n_c V_{FB})} + \gamma_c^2 V_{FB} n_\Psi \ . \end{aligned} \tag{2.49}$$

This equation allows us to solve for γ_c and obtain $\langle N_\Psi^{\rm eq}\rangle$. Again the second term on the r.h.s is numerically negligible due to $m_\Psi \gg m_c$.

It is instructive to examine two limits where a large (small) number of charm-quark pairs are produced. We first note the following property of Bessel functions,

$$\frac{I_1(x)}{I_0(x)} \to \begin{cases} 1 \ , & x \gg 1 \\ \frac{x}{2} \ , & x \ll 1 \ . \end{cases} \tag{2.50}$$

Therefore, in these two limits, Eq. (2.44) reduces to

$$\langle N_{c\bar{c}} \rangle \rightarrow \begin{cases} Z_1 \ , & \langle N_{c\bar{c}} \rangle \gg 1 \\ Z_1^2 \ , & \langle N_{c\bar{c}} \rangle \ll 1 \ . \end{cases} \tag{2.51}$$

Plugging Eq. (2.51) into Eq. (2.45), one obtains

$$\langle N_{\Psi}^{\rm reg} \rangle \rightarrow \begin{cases} \langle N_{c\bar{c}} \rangle^2 N_1^{\rm reg} \ , & \langle N_{c\bar{c}} \rangle \gg 1 \\ \langle N_{c\bar{c}} \rangle \, N_1^{\rm reg} \ , & \langle N_{c\bar{c}} \rangle \ll 1 \ . \end{cases} \tag{2.52}$$

In the limit of $\langle N_{c\bar{c}} \rangle \gg 1$, the yield of the regeneration component is proportional to $\langle N_{c\bar{c}} \rangle^2$, the same result one would get if the canonical constraint $N_c \equiv N_{\bar{c}}$ was neglected; therefore the this limit is often called the "grand-canonical" limit. In the opposite ("canonical") limit, where $\langle N_{c\bar{c}} \rangle \ll 1$, the regeneration component is proportional to $\langle N_{c\bar{c}} \rangle$: the canonical constraint $N_c \equiv N_{\bar{c}}$ effectively enhances the charmonium regeneration by a factor of $1/\langle N_{c\bar{c}} \rangle$ over the grand-canonical limit. As a side remark, particle production in the "canonical ensemble" can also be conveniently described with a kinetic master equation approach as developed in Ref. [48], which has been applied to study strange particle production in low energy heavy-ion collisions [49] where the net "strangeness", $(N_s - N_{\bar{s}})$, is constrained to zero in each event.

2. Charm-Quark Correlation Volume

It turns out that the correlation between the charm and anti-charm quarks goes beyond "production-in-pair" in each event. The charm and anti-charm quarks are produced at the same spatial point in hard N+N collisions and then recede from each other. Before the medium evolution stops (freeze-out) they can only diffuse into a limited portion of the fireball volume. The volume they explore is referred to as charm-quark correlation volume [44], V_{co}, which in general is smaller than the

full fireball volume, V_{FB}. A schematic estimate of $V_{co}(t)$ will be presented in Section VI.A. The restriction of $c\bar{c}$ pairs to within the correlation volume effectively increases the $c\bar{c}$ coalescence probability: One charm quark can more easily find its partner nearby inside the correlation volume V_{co} with the effective spatial density, $n_{\bar{c}}^{eff} \equiv d_{\bar{c}} \int \frac{d^3p}{(2\pi)^3} f_{\bar{c}}^{eff}(p)$, of its partner given by

$$n_{\bar{c}}^{eff} = \frac{k}{kV_{co}} = \frac{1}{V_{co}} \ , \tag{2.53}$$

for an event in which k charm quark pairs are produced. The effective density, $n_{\bar{c}}^{eff}$, is larger than k/V_{FB} (the $\bar{c}$ density without correlation volume effect) by a factor of $V_{FB}/(kV_{co})$, if we assume k anti-charm quarks residing in k correlation volume "bubbles" (no merging of correlation volumes).

It is instructive to work out the parametric dependence of the regeneration component, $N^{\rm reg}(k)$, on the charm quark pair number k in two limits:

(a) In the limit of $\langle N_{c\bar{c}} \rangle \ll V_{FB}/V_{co}$ the overlap of correlation "bubbles" can be neglected; we have $N^{\rm reg}(k) = [V_{FB}/(kV_{co})] \cdot k^2 N_1^{\rm reg}$.

(b) In the opposite limit, $\langle N_{c\bar{c}} \rangle \gg V_{FB}/V_{co}$, the k correlation volume "bubbles" maximally overlap with each other with their total volume filling the entire fireball volume V_{FB}, leading to an effective anti-charm quark density $n_{\bar{c}}^{eff} = k/V_{FB}$. In this limit there is no correlation volume effect so we have $N^{\rm reg}(k) = k^2 N_1^{\rm reg}$. In these two limits the average number of regenerated Ψ is

$$\langle N_\Psi^{\rm reg} \rangle = \sum_{k=0}^{\infty} N^{\rm reg}(k) P(k) \to \begin{cases} N_1^{\rm reg} Z_1 \frac{I_0(2Z_1)}{I_1(2Z_1)} \frac{V_{FB}}{V_{co}} \ , & \langle N_{c\bar{c}} \rangle \ll V_{FB}/V_{co} \\ N_1^{\rm reg} Z_1^2, & \langle N_{c\bar{c}} \rangle \gg V_{FB}/V_{co} \ . \end{cases} \tag{2.54}$$

Comparing Eq. (2.54) with Eq. (2.44) one sees that in the case of $1 \ll \langle N_{c\bar{c}} \rangle \ll V_{FB}/V_{co}$ the correlation volume effect renders $\langle N_\Psi^{\rm reg} \rangle$ to depend linearly on $\langle N_{c\bar{c}} \rangle$ even if the $c\bar{c}$ system is in the "grand-canonical" limit. In other words, the correlation

volume effect "delays" the transition between the "canonical" and "grand-canonical" ensembles from $\langle N_{c\bar{c}} \rangle \sim 1$ to $\langle N_{c\bar{c}} \rangle \sim V_{FB}/V_{co}$. In the general case where $\langle N_{c\bar{c}} \rangle$ is comparable to V_{FB}/V_{co} the merge of correlation volumes needs to be taken care of on a term-by-term basis in the series of $N^{\rm reg}(k)$. Whenever two correlation volume bubbles merge their new total volume (smaller than the sum of their individual volumes) should be used for estimating the effective anti-charm density n_c^{eff}. In Section VI.C.1, we will study the sensitivity of J/ψ regeneration on different correlation volume sizes based on a rather schematic prescription of merging correlation volumes: If at any given time, t, the total correlation volume of individual "bubbles" $kV_{co}(t)$ is larger than the fireball volume $V_{FB}(t)$, $kV_{co}(t)$ is set to $V_{FB}(t)$ for determination of the effective anti-charm density n_c^{eff} in the subsequent evolution.

We conclude this section by pointing out that a more rigorous and systematic way to account for canonical-ensemble and correlation volume effects is to use the joint phase space distribution function, $\langle f_c f_{\bar{c}} \rangle$, as the input for Ψ regeneration rate, β_Ψ. The $\langle f_c f_{\bar{c}} \rangle$ can be obtained, *e.g.*, from high statistics Langevin simulations of the evolution of charm quark pairs in the medium.

CHAPTER III

CHARMONIUM IN THE HOT MEDIUM

In this chapter we discuss the microscopic mechanisms for the reactions of charmonia, Ψ (Ψ=J/ψ, χ_c, ψ'), in the hot medium created in heavy-ion collisions. In Section III.A, we review the relevant properties of Ψ in the QGP relevant for charmonium production. In Section III.B, we discuss the charmonium dissociation mechanisms for Ψ with reduced in-medium binding energy $\epsilon_B < T$, the quasifree-dissociation process of charmonium dissociation, and compare to the more traditional mechanism, gluo-dissociation process. In Section III.C, we explicitly calculate charmonium regeneration rates in QGP with several input charm-quark spectra. In Section III.D, we briefly discuss charmonium dissociation in the hadronic matter (at T below the critical temperature T_c). In Section III.E, we construct charmonium spectral functions based on the quasifree dissociation rates and compare to lattice calculations, through which we extract charmonium dissociation temperatures, T^{Ψ}_{diss}.

A. Charmonium in QGP

On the microscopic level the medium affects charmonium states in three ways:

1) Debye screening: The QGP is a deconfined medium therefore the freely moving colored partons screen the binding force of a charmonium state and decrease its binding energy, $\epsilon_B(T)$. The in-medium $\epsilon_B(T)$ is defined as

$$\epsilon_B(T) = 2m_c^*(T) - m_\Psi(T) \ , \tag{3.1}$$

where m_c^* and m_Ψ are in-medium charm-quark and charmonium masses. The in-medium part of m_c^* is identified with the asymptotic value of the heavy-quark (HQ)

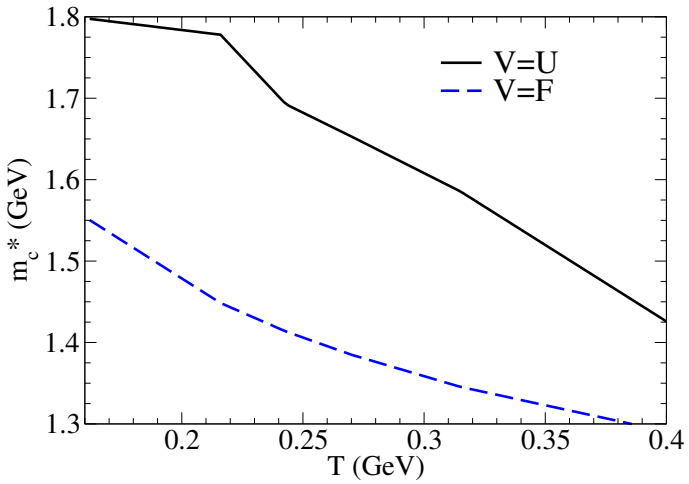

Fig. 16. Temperature dependence of in-medium charm quark mass in the strong (solid line) and weak binding (dashed line) scenarios. Figure taken from Ref. [28].

potential, as displayed in Fig. 16.

$$m_c^*(T) \equiv m_c^0 + V_{Q\bar{Q}}(r \to \infty; T)/2 \ . \tag{3.2}$$

In this work we approximate the HQ potential, $V_{Q\bar{Q}}(r;T)$, based on the lQCD heavy-quark free energy, $F_{Q\bar{Q}}(r;T)$, (recall Section I.D) within either the "strong" ($V_{Q\bar{Q}} = U_{Q\bar{Q}}(r;T)$) or "weak" binding ($V_{Q\bar{Q}} = F_{Q\bar{Q}}(r;T)$) scenario. The in-medium masses decrease with temperature appreciably, while the magnitude of $m_c^*(T)$ is significantly smaller in the weak-binding compared to the strong-binding scenario.

For a quantitative estimate of $\epsilon_B(T)$ we take recourse to the potential model of Ref. [50] where quarkonium spectral functions and correlators (recall Eq. (1.20) and Eq. (1.19)) have been calculated in a thermodynamic T-matrix approach, consistent with vacuum spectroscopy and including relativistic corrections for a proper description of scattering states. The calculations in there have been carried out for both free and internal energies as potential, and for two different lQCD inputs [27, 51]. Since the internal energy leads to stronger binding than the free energy we refer to

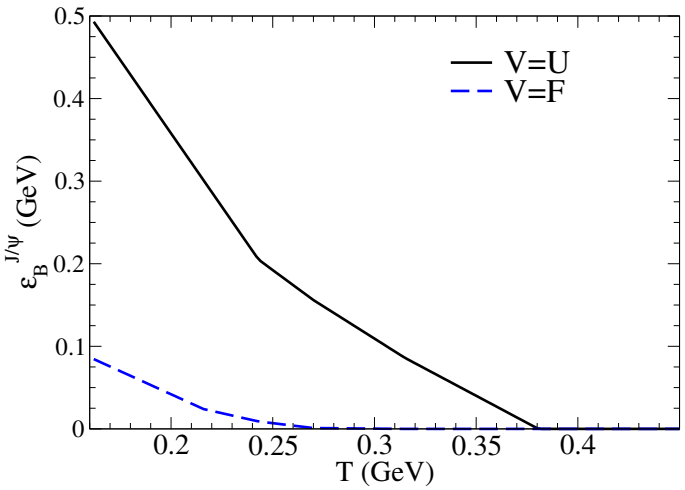

Fig. 17. Temperature dependence of J/ψ binding energy in the strong (solid line) and weak binding (dashed line) scenarios.

the former and latter as strong- and weak-binding scenario, respectively. In both scenarios (and for both potentials), an approximate constancy (within $\pm 15\%$) of the correlator ratios, Eq. (1.24), for pseudoscalar charmonium has been found (see lower panels of Fig. 12 and 14 in Ref. [50]). We believe that these results provide a reasonable bracket for potential-model results. Similar to $m_c^*(T)$, the resulting binding energies (plotted in Fig. 17) also decrease with T, again being significantly smaller in the weak-binding scenario. These features are, in fact, the main reason that both scenarios can be compatible with the small variations found in the lQCD correlator ratios: for weak/strong binding, a small/large constituent mass combines with a small/large binding energy, respectively, leading to an approximate compensation in the bound-state mass, $m_\Psi(T)$, recall Eq. (3.1).

2) Collisional dissociation/regeneration: Charmonia are subject to dissociation through collisions with particles in the medium even if they have finite binding energies. We assume both chemical and thermal equilibrium for light partons, so that

their p_t spectra follow the thermal Bose/Fermi distribution,

$$f_B^i(k,T) = \frac{1}{\exp\left(\frac{\sqrt{k^2+m_i^2}}{T}\right)-1}\ , \qquad i=g, \tag{3.3}$$

$$f_F^i(k,T) = \frac{1}{\exp\left(\frac{\sqrt{k^2+m_i^2}}{T}\right)+1}\ , \qquad i=u,\bar{u},d,\bar{d},s,\bar{s}\ . \tag{3.4}$$

Their thermal masses m_i are guided by perturbative QCD (pQCD) calculations,

$$m_{u,d}^2 = \frac{g^2T^2}{3}\ , \tag{3.5}$$

$$m_s^2 = m_0^2+\frac{g^2T^2}{3}\ , \tag{3.6}$$

$$m_g^2 = \left(1+\frac{N_f}{6}\right)\frac{g^2T^2}{2}\ , \tag{3.7}$$

where N_f=2.5 is the number of flavors, and the coupling constant g is adjusted so that the resulting energy density of the QGP medium, $e(T)$, reproduces the lattice-QCD results, see Chapter IV for more details. The microscopic mechanisms of the scattering between Ψ and particles in the heatbath will be detailed in the next section.

3) Bose-enhancement/Pauli blocking: In charmonium dissociation or regeneration processes light partons may be produced in the final state, *e.g.*, $i+\Psi \to i+c+\bar{c}(i=g,q,\bar{q})$. In the QGP the final state phase space of the light particle is altered due to the Bose-enhancement $(1+f_B^i(k,T))$ and Pauli blocking $(1-f_F^i(k,T))$ factors for gluons and quarks, respectively, recall Eqs. (2.14), (2.15) and (2.16).

B. Charmonium Dissociation in the QGP

Let us start with the traditional gluo-dissociation process ($\Psi+g\to c+\bar{c}$) as illustrated in Fig. 18, proposed by Bhanot and Peskin in the 1970s [52]. They evaluated the interaction between a charmonium state and a gluon within an Operator Prod-

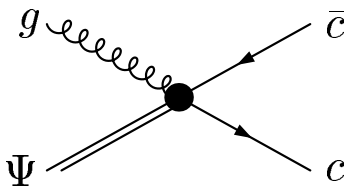

Fig. 18. Diagrams of the gluo-dissociation process. A charmonium absorbs a gluon and is subsequently dissociated.

uct Expansion (OPE) formalism. The leading order in α_s turns out to be a dipole interaction ($\vec{r}\cdot\vec{E}$) between the Ψ and the gluon. For J/ψ dissociation cross section it results in the following expression,

$$\sigma_{gJ/\psi}(E_g) = \frac{2\pi}{3}\left(\frac{32}{3}\right)^2\left(\frac{m_c}{\epsilon_B}\right)^{1/2}\frac{1}{m_c^2}\frac{(E_g/\epsilon_B-1)^{3/2}}{(E_g/\epsilon_B)^5}\ , \tag{3.8}$$

where the m_c is the mass of the charm quark, E_g is the energy of incoming gluon and ϵ_B is the binding energy of J/ψ, see Eq. (3.1). We note that the cross section $\sigma_{gJ/\psi}(E_g)$ exhibits a pronounced peak at $E_g = \frac{10}{7}\epsilon_B$, see Fig. 19. Note that since we adopt a massive gluon with $m_g|_{T=300\text{MeV}} \simeq$580MeV (see Eq. (3.7)), the peak appears at gluon momentum $p_g \simeq$700MeV for vacuum J/ψ binding energy of 640MeV. The limitations of the gluo-dissociation process include: (1) As mentioned in Ref. [52] the OPE procedure is valid only if the energy scale of the incoming gluon is much less the charmonium binding $E_g \ll \epsilon_B$. (2) Since Eq. (3.8) is only to the leading order in α_s, it does not include the interaction between J/ψ and light quarks.

Indeed, with in-medium binding energy $\epsilon_B < T$ the gluo-dissociation mechanism turns out to be not numerically efficient in destroying J/ψ. To see this we calculate the dissociation rate, Γ_Ψ, which is a convolution of the density of incoming particles (gluons in this context), $f_g(p_g)$, with the dissociation cross section, $\sigma_{g\Psi}(s)$ and the relative velocity v_{rel} between the incoming particle and the charmonium (cf. Eqs. (2.4)

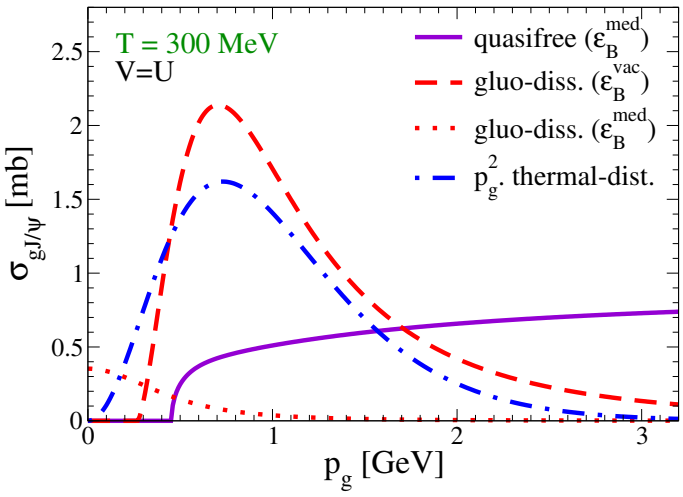

Fig. 19. Comparison of the parton-induced dissociation cross section. Solid line: quasifree dissociation mechanism; dashed line: gluo-dissociation with vacuum J/ψ binding energy; dotted line: gluo-dissociation cross section with in-medium J/ψ binding energy of 110MeV; dot-dashed line: gluon thermal distribution $p_g^2\, f_g(p_g)$ at T=300MeV.

and (2.9)),

$$\Gamma_\Psi(p,x) = \int \frac{d^3p_g}{(2\pi)^3}\, d_g f_g(p_g)\, v_{rel}\, \sigma_{g\Psi}(s)\ . \tag{3.9}$$

Here the gluon momentum distribution $f_g(p_g)$ follows from Eq. (3.3).

Figure 19 shows that the inefficiency of the gluo-dissociation for J/ψ with in-medium binding energy originates from the peak structure of the gluo-dissociation cross section. Note that since we use a massive gluon with $m_g|_{T=300\mathrm{MeV}} \simeq$580 MeV, the gluon energy at p_g=0 is already significantly larger than $\frac{10}{7}\epsilon_B|_{T=300\mathrm{MeV}}\sim$160 MeV, therefore only the "tail" of the gluo-dissociation cross section appears in Fig. 19, leading to a small overlap between the thermal gluon distribution $p_g^2\, f_g(p_g)$ and the dissociation cross section, $\sigma_{gJ/\psi}(p_g)$. The gluo-dissociation cross sections for χ_c and ψ' show similar peak structures, resulting in small in-medium dissociation rates.

On the other hand we know that in the limit of incoming gluon energy large compared to the charmonium binding energies, $\epsilon_B > E_g$, the interaction between

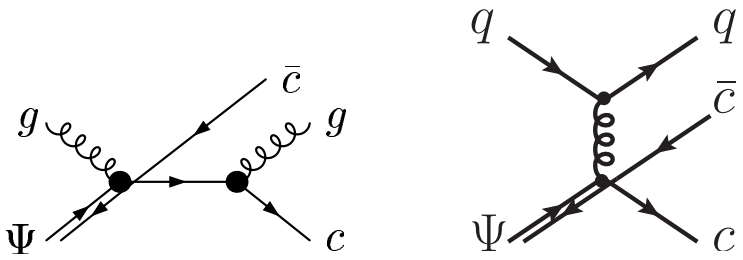

Fig. 20. Diagrams of the quasifree process. A charmonium can be dissociated by either a quark or a gluon.

the c and $\bar{c}$ inside the charmonium, which occurs on a time scale of $1/\epsilon_B > 1/E_g$, cannot interfere with the interaction between the incoming gluon and the $c(\bar{c})$. In this limit the $g - \Psi$ scattering cross section should approach the value of $2\sigma_{gc}$, the sum of the probability of the scattering between the gluon and one of the constituent charm quarks. Therefore the peak structure of gluo-dissociation cross section will be superseded by continuum-like "quasifree" dissociation cross section.

Following this idea an alternative (quasifree) dissociation mechanism, $i + \Psi \to i + c + \bar{c}(i = g, q, \bar{q})$, was proposed to describe the inelastic scattering between the charmonium and partons [37]. In these processes the incoming parton (gluon or quark) collides with the c or $\bar{c}$ quark in the Ψ. Since in the QGP charmonia are loosely bound states one such collision would be enough to dissociate the Ψ, as illustrated in Fig. 20. The transition matrix element for the quasifree dissociation can therefore be factorized as

$$
\begin{aligned}
&|\overline{\mathcal{M}_{\Psi i\to c\bar{c}i}(p_i, p_\Psi; \bar{p}_i, p_c, p_{\bar{c}})}|^2 \delta^{(4)}(p_i + p_\Psi - p_c - p_{\bar{c}} - \bar{p}_i) \\
&\qquad \to 2 \left|\overline{\mathcal{M}_{ci\to ci}\left(p_i, \frac{m_{c'}}{m_\Psi} p_\Psi; \bar{p}_i, p_c\right)}\right|^2 \delta^{(4)}\left(\frac{m_{c'}}{m_\Psi} p_\Psi + p_i - p_c - \bar{p}_i\right) \\
&\qquad\qquad \times (2\pi)^3 \, (2E_{\bar{c}}) \, \delta^{(3)}\left(\frac{m_c}{m_\Psi} p_\Psi - p_{\bar{c}}\right) \, , \qquad (3.10)
\end{aligned}
$$

where $|\overline{\mathcal{M}_{\Psi i\to c\bar{c}i}}|^2$ is the quasifree dissociation transition matrix element, and $|\overline{\mathcal{M}_{ci\to ci}}|^2$

the transition matrix element for the elastic scattering between i and c, calculated in Ref. [53]. The momenta p_i, p_Ψ, $\bar{p}_i$, p_c and $p_{\bar{c}}$ correspond to the initial state parton i, initial Ψ, final state parton i, final state c and final state $\bar{c}$. The overall factor of 2 is accounting for the fact that the elastic scattering with either c or the $\bar{c}$ can dissociate the Ψ.

To account for the leading kinematic correction from the residual binding energy, the incoming parton needs to be energetic enough to break up the bound state, which sets a lower limit for the incoming parton momentum. Overall 4-momentum conservation for the process $i + \Psi \to i + c + \bar{c}$ is maintained by assigning the binding energy to a decrease in mass of the initial-state charm-quark, c', *i.e.*, $m_{c'} = m_c - \epsilon_B$. In addition, we have introduced a Debye mass, $m_D = gT$, into the denominator of t-channel gluon-exchange propagator, $1/t \to 1/(t - m_D^2)$, to regulate the divergence for forward scattering (the strong coupling in m_D is taken consistently with the coupling constant α_s used for the quasifree process).

Inserting the quasifree transition probability Eq. (3.10) into Eq. (2.15) we can evaluate the corresponding dissociation cross section and rate. The comparison of the dissociation cross sections between the quasifree dissociation processes and the gluo-dissociation process is shown in Fig. 19. In contrast to the gluo-dissociation cross section the quasifree dissociation cross section saturates for partons with large incoming momentum ($k \gg \epsilon_B$). Since the quasifree process may not be the only dissociation mechanism for Ψ, for practical applications we effectively parameterize other dissociation mechanism into the quasifree processes by using the strong coupling constant α_s (figuring into $|\mathcal{M}_{ci\to ci}|^2$) as an adjustable parameter. We adjust it to the J/ψ suppression data measured at SPS/RHIC, see Chapter VI for the detailed procedure. The resulting value of α_s turns out to be $\simeq$0.3, quite compatible with the short-distance (color-Coulomb) term in the effective potential used to extract the

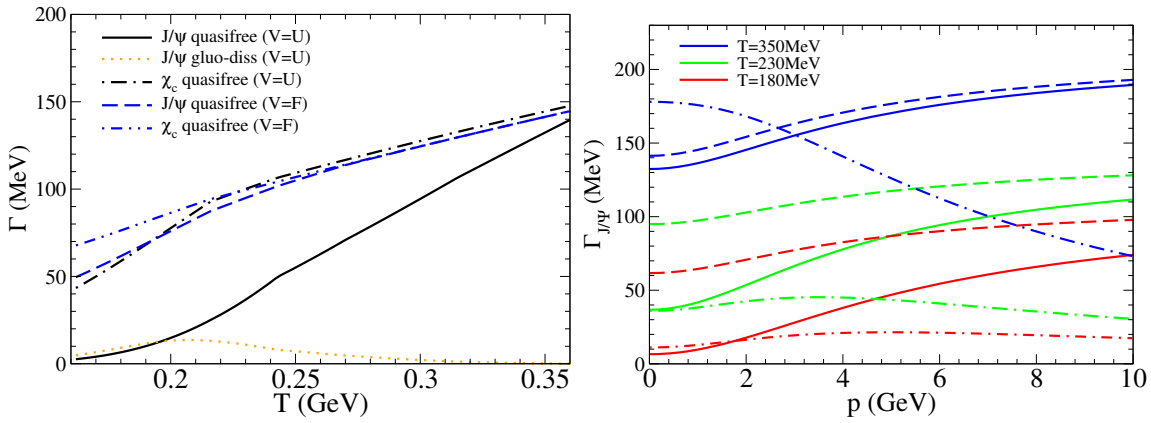

Fig. 21. Temperature and momentum dependence of Ψ dissociation rates. Left panel: Temperature dependence of dissociation rates (at p=0) for J/ψ and χ_c. Solid line: J/ψ quasifree dissociation rate in the strong binding scenario; dashed line: J/ψ quasifree dissociation rate in the weak-binding scenario; dot-dashed line: χ_c quasifree dissociation rate in the strong-binding scenario; double–dot-dashed line: χ_c quasifree dissociation rate in the weak-binding scenario; dotted line: J/ψ gluo-dissociation rate in the strong binding scenario with α_s=0.3. Right panel: Momentum dependence of J/ψ quasifree dissociation rates for strong binding scenario (solid line); weak binding scenario (dashed line) and gluo-dissociation rate with vacuum J/ψ binding energy (dot-dashed line).

binding energies by the T-matrix potential model. Note that the strong coupling constant in the quasifree process is decoupled from that figuring into parton thermal masses in Eqs. (3.5), (3.6) and (3.7).

The temperature dependence of the quasifree dissociation rates for the J/ψ and χ_c in the QGP is plotted for $\vec{p}$=0 in the left panel of Fig. 21, and for the J/ψ as a function of p at selected temperatures in the right panel.

In the weak-binding scenario, there is rather little difference between the dissociation rates of J/ψ and χ_c, especially above $T = 200\,\mathrm{MeV}$. Only in the strong-binding scenario the larger J/ψ binding energy makes a large difference, suppressing its destruction by, *e.g.*, a factor of $\sim$5 at $T \simeq 200\,\mathrm{MeV}$ relative to the χ_c and ψ' (not shown);

this difference becomes larger (smaller) at smaller (larger) T. For comparison we also calculated the rate due to the gluo-dissociation mechanism employing the expression derived in Ref. [52] with the same $\alpha_s \simeq 0.3$ as in the quasifree rate and with ϵ_B obtained from the strong-binding scenario (note that the Coulombic binding is much smaller), which turns out to be inefficient for dissociating J/ψ's (and even more so for the excited states) and is thus neglected in the following. We also note that to achieve a comparable dissociation rate, say, $\Gamma_{J/\psi} \sim 100\,\mathrm{MeV}$ at $T \sim 300\,\mathrm{MeV}$ in a hadronic medium, one needs a hadron density of about $5/\mathrm{fm}^3$ for typical thermal averaged hadronic dissociation cross section of around 1mb [54].

The 3-momentum dependence of the rates shows a monotonous increase with increasing p, which becomes more pronounced with increasing binding energy (for larger ϵ_B a finite 3-momentum facilitates the break-up since, on average, a larger center-of-mass energy is available in the collision of the bound state with thermal partons). This increase is a simple kinematic consequence of a monotonously increasing (or even constant) cross section with finite threshold and an increasing parton flux encountered by a moving J/ψ.

C. Charm-Quark Spectra and Charmonium Regeneration in the QGP

In the previous section we discussed in-medium dissociation of charmonium states on the microscopic level. The inverse process, the regeneration of charmonium states from charm quarks, should also occur and obey the principle of detailed balance with the dissociation processes. The expressions for the regeneration rates, Eq. (2.10) and Eq. (2.16), are similar to those of the dissociation rates, Eq. (2.4) and Eq. (2.15). The only difference is that the charm-quark phase space distributions, $f_{c(\bar{c})}(x, p_c, t)$, appear in the initial phase space. Below we first give a brief review of the typical

time evolution of $f_{c(\bar{c})}(x, p_c, t)$:

Since the c and $\bar{c}$ quarks are produced in hard collisions their initial transverse momentum spectra are rather "hard", with $\langle p_t^2 \rangle \simeq 3\,\mathrm{GeV}^2$. (As an estimate for a typical temperature of T=250 MeV in heavy-ion collisions, the thermal momentum spectra have $\langle p_t^2 \rangle \simeq 1\,\mathrm{GeV}^2$, much smaller than the initial spectra from hard collision.) Later they collide with particles in the (thermalized) medium and gradually equilibrate their momentum with the heatbath. If the medium does not cool down they will eventually be thermalized and their momentum spectra follow the thermal spectra, $f_{c(\bar{c})}(p_c) \propto e^{-E_c/T}$ with $E_c = \sqrt{m_c^2 + p_c^2}$. However, compared to light quarks the charm quark thermalization is a slow process, "delayed" relative to light quarks by a factor of $\sim m_c/T \simeq 5$. Since the thermalization time for the bulk medium is of order $\sim$ 1fm/c, the thermal relaxation time for charm quarks is expected be on the order of $\sim$ 5fm/c [55], which is comparable to the lifetime of QGP at RHIC. Therefore, during the lifetime of the hot medium the charm-quark spectra are expected to be partially thermalized. Quantitative calculations of charm quark thermalization can be performed with a Boltzmann transport equation for charm quarks.

The Boltzmann equation for charm quarks is an intego-differential equation, which is numerically difficult to handle. Therefore Fokker-Planck equations and Langevin simulation techniques are often employed as approximations to the Boltzmann transport equation to describe the time evolution of charm-quark phase space distribution function, see Ref. [55] for a recent review.

In this work we compare charmonium regeneration rates resulting from two limiting cases of charm-quark spectra:

1) fully thermalized charm-quark spectra. In the local rest frame, they have the

following form,

$$\frac{dN_c^{\rm th}}{d^3p} \propto e^{-\sqrt{m_c^2+p^2}/T} \ . \tag{3.11}$$

2) spectra from initial hard production (pQCD spectra). We employ a parameterization given in Ref. [56],

$$\frac{dN_c^{\rm pqcd}}{d^3p} \propto \frac{(p+A)^2}{(1+p/B)^\alpha} \ , \tag{3.12}$$

with A=0.5 GeV, B=6.8 GeV, α=21. This parameterization is based on the charm-quark p_t spectra generated in 200 GeV proton-proton (p+p) collisions by PYTHIA [57]. 3) pQCD spectra (3.12) in transverse direction, and a thermal spectrum in longitudinal (p_z) direction,

$$\frac{dN_c^{\rm pqcd+th}}{d^2p_t dp_z} \propto \frac{(\sqrt{p_t^2+p_z^2}+A)^2}{N(p_z)(1+\sqrt{p_t^2+p_z^2}/B)^\alpha} \times e^{-\sqrt{m_c^2+p_z^2}/T} \ , \tag{3.13}$$

where

$$N(p_z) = \int d^2p_t \frac{(\sqrt{p_t^2+p_z^2}+A)^2}{(1+\sqrt{p_t^2+p_z^2}/B)^\alpha} \ . \tag{3.14}$$

The thermal distribution in longitudinal direction is to mimic the longitudinal smearing of the center of the mass momentum due to various momentum fractions, x, carried by the two colliding primordial partons in $c\bar{c}$ production process $g(q)+g(\bar{q}) \to c+\bar{c}$. We denote these spectra as "pQCD+thermal" spectra.

The three types of charm-quark distribution are compared in the left panel of Fig. 22 in terms of the p_z-integrated p_t spectra. They are all normalized to the same total charm pair number. The thermal spectra are the softest ($\langle p_t^2\rangle$=1.1 GeV^2), with most of the yield concentrated at low p_t. The 3-dimensionally isotropic pQCD spectra ($\langle p_t^2\rangle$=3.5 GeV^2) and the transversely pQCD + longitudinally thermal spectra ($\langle p_t^2\rangle$=3.0 GeV^2) are almost of comparable hardness in the transverse plane, with the 2+1-dimensional pQCD spectra being slightly softer due to their thermalization in z

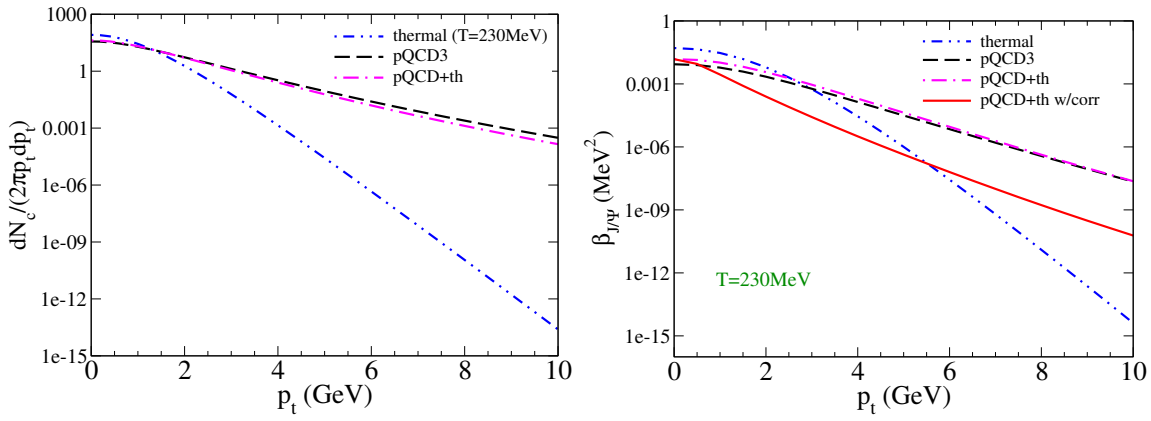

Fig. 22. Charm-quark p_t spectra and J/ψ regeneration rates. Left panel: Comparison of different input charm-quark p_t spectra. Right panel: their resulting charmonium regeneration rates evaluated in the strong binding scenario. Dashed line: 3-dimensional isotropic pQCD charm-quark spectra; dot-dashed line:transversely pQCD + longitudinally thermal spectra; double-dot-dashed line: thermal charm-quark spectra with m_c=1.73 GeV; solid line: transversely pQCD with angular correlation + longitudinally thermal spectra.

direction.

As discussed in Section III.B the quasifree process is the dominant dissociation mechanism for in-medium Ψ. According to the principle of detailed balance the inverse quasifree process, $i+c+\bar{c} \to i+\Psi$ $(i = g, q, \bar{q})$, is the corresponding regeneration processes. Its transition matrix element can be obtained by applying detailed balance, Eq. (2.12), to the quasifree dissociation matrix element, Eq. (3.10),

$$
\begin{aligned}
&|\overline{\mathcal{M}_{c\bar{c}i\to\Psi i}(p_i,p_c,p_{\bar{c}};\bar{p}_i,p_\Psi)}|^2\delta^{(4)}(p_c+p_{\bar{c}}+p_i-\bar{p}_i-p_\Psi) \\
&\qquad \to 2\,\left(\frac{d_\Psi}{d_c d_{\bar{c}}}\right)\,\left|\overline{\mathcal{M}_{ci\to ci}\left(p_i,p_c\,;\,\bar{p}_i,\frac{m_{c'}}{m_\Psi}\,p_\Psi\right)}\right|^2\,\delta^{(4)}\left(p_i+p_c-\bar{p}_i-\frac{m_{c'}}{m_\Psi}\,p_\Psi\right) \\
&\qquad\qquad \times(2\pi)^3\,(2E_{\bar{c}})\,\delta^{(3)}\left(p_{\bar{c}}-\frac{m_c}{m_\Psi}\,p_\Psi\right)\,. \qquad (3.15)
\end{aligned}
$$

Here, $|\overline{\mathcal{M}_{ci\to ci}}|^2$ is the transition matrix for the elastic scattering between i and c.

The momenta of initial state parton i, initial state c, initial state $\bar{c}$, final state i and final state Ψ are p_i, p_c, $p_{\bar{c}}$, $\bar{p}_i$, and p_Ψ. $m_{c'} = m_c - \epsilon_B$ is the mass of the charm quark in the final state of the elastic scattering process. Note that the factor of $\frac{d_\Psi}{d_c d_{\bar{c}}}$ comes from summing over final state color-spin degeneracy and averaging over initial state degeneracy. In the quasifree approximation the 3→2 coalescence process is reduced to a 2→2 (quasi-elastic) scattering process.

We proceed to calculate the charmonium regeneration rate by plugging the charm-quark spectra and the transition matrix element, Eq. (3.15), into Eq. (2.16). The resulting J/ψ regeneration rates, $\beta_\Psi(p_t)$, from different charm-quark spectra are compared in the right panel of Fig. 22. The $\beta_\Psi(p_t)$ can be interpreted as the regenerated number of Ψ with a given p_t per unit volume per unit time. Here we have integrated over the p_z dependence of $\beta_\Psi(p)$.

As expected, the p_t dependence of the regeneration rate from thermal (pQCD) charm spectra follows a thermal (pQCD) trend. The thermal charm spectra, with the largest charm-quark phase overlap in the low-p_t region, lead to the largest inclusive regeneration rate, $\beta_{tot} = \int d^3p\, \beta(p)$. The 3-dimensional isotropic pQCD spectra and the transverse pQCD + longitudinal thermal spectra lead to significantly smaller inclusive regeneration rates, amounting to 28% and 47% of that from thermal charm-quark spectra, respectively. This is similar to what is found in Ref. [58], where the dynamics of $c\bar{c}$ coalescence was encoded in a Gaussian Wigner function and the resulting number of J/ψ from pQCD charm-quark spectra is smaller than that from thermal spectra by a factor of 3. However in Ref. [40] where the (inverse) gluo-dissociation mechanism was employed for J/Ψ regeneration it is found that the inclusive yield of regenerated J/ψ from pQCD charm spectra is quite comparable with that from thermal spectra (within ∼30%). Further investigations are needed to clarify the discrepancy.

For pQCD+thermal charm spectra we also consider a possible angular correlation

between c and $\bar{c}$ in momentum space: it is expected from pQCD that in initial hard collisions back-to-back charm pair production is favored. We study its consequence on J/ψ regeneration by including a schematic ansatz of $dN_{c\bar{c}}/d\theta \sim (1-\cos\theta)$ in Eq. (2.15) (with θ being the relative angle between the p_t of c and $\bar{c}$ in the transverse plane). It turns out that the angular correlation of c and $\bar{c}$ significantly reduces the regeneration rate for high p_t J/ψ as seen in Fig. 22. The reason is that, compared to low p_t J/ψs, high p_t ones are more likely to be regenerated from a $c\bar{c}$ pair with small angle between them, the probability of which is suppressed by the angular correlation factor $(1-\cos\theta)$. The inclusive regeneration rate from the angular correlated pQCD+thermal spectra is 11% of that from thermal charm spectra. We subsequently plug $\beta_\Psi(p_t)$ into the Boltzmann transport equation and the numerical results for the inclusive yield and p_t spectra of the regenerated J/ψ will be compared in Chapter VI.

D. Charmonium Dissociation in Hadronic Matter

As the fireball expands, the medium keeps cooling. When the medium temperature decreases to the critical temperature, T_c, the deconfined QGP undergoes a phase transition to the confined hadronic phase. The charmonium dissociation rate in the hadronic phase is expected to be small compared to QGP due to the smaller light particle density and the larger charmonium binding energy. However, for a quantitative calculation of charmonium yields in heavy-ion collisions, dissociation/regeneration in hadronic phase needs to be taken into account.

The microscopic approaches for the hadronic charmonium dissociation can be divided into two categories, based on either quark or hadronic degrees of freedom. The approaches based on hadronic degrees of freedom are often less cumbersome yet very effective in assessing many dissociation processes, see Ref. [59] for a recent review.

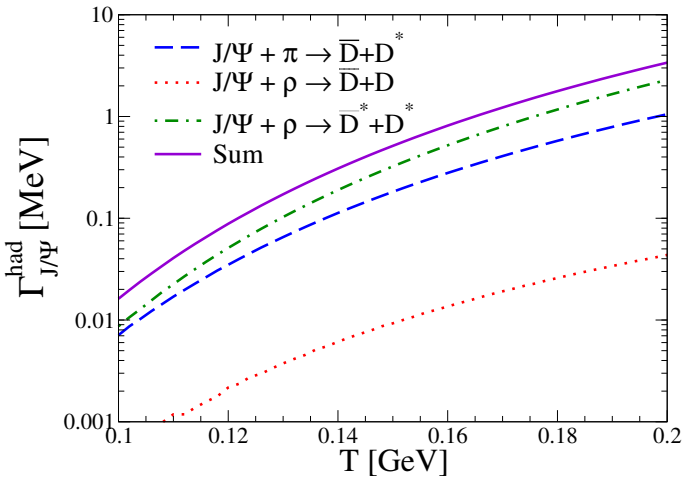

Fig. 23. J/ψ dissociation rates by pions and rhos as a function of the temperature T of the hadron gas. Figure taken from Ref. [61]. The full line is the sum of the three contributions, $J/\psi + \pi$ (dashed line), $J/\psi + \rho \to D^\star + \bar{D}^\star$ (dot-dashed line) and $J/\psi + \rho \to D + \bar{D}$ (dotted line).

In this work we adopt dissociation rates based on an effective meson Lagrangian with a local $SU(4)$ flavor symmetry [54, 60, 61]. The considered interactions are J/ψ with pions and rho mesons which are the most abundant particles in the hadronic medium,

$$\pi + J/\psi \quad \to D + \bar{D}^\star, \bar{D} + D^\star \tag{3.16}$$

$$\rho + J/\psi \quad \to D + \bar{D} \tag{3.17}$$

$$\rho + J/\psi \quad \to D^\star + \bar{D}^\star \ . \tag{3.18}$$

We neglect the interactions between J/ψ and kaons (In Ref. [62], the total cross section of J/ψ dissociation by kaons is found to be much smaller than that by pions). The resulting dissociation rates are shown in Fig. 23, with the main contribution given by the $\rho + J/\psi \to D^\star + \bar{D}^\star$ process. The vacuum masses are assumed for all the hadrons including J/ψ.

For dissociation rates of χ_c and ψ' we assume a geometrical scaling [114] of the

dissociation rates for J/ψ by the respective charmonium radii, namely,

$$\Gamma_{\chi}^{HAD} = \left(\frac{r_{\chi}}{r_{J/\psi}}\right)^2 \Gamma_{J/\psi}^{HAD} \simeq 2.36\ \Gamma_{J/\psi}^{HAD}\ , \tag{3.19}$$

$$\Gamma_{\psi'}^{HAD} = \left(\frac{r_{\psi'}}{r_{J/\psi}}\right)^2 \Gamma_{J/\psi}^{HAD} \simeq 3.73\ \Gamma_{J/\psi}^{HAD}\ . \tag{3.20}$$

The radii of the excited charmonia states are estimated by non-relativistic potential models from Ref. [24].

As expected, the overall charmonium dissociation rates in the hadronic phase are significantly smaller than in the QGP phase, resulting in a rather mild charmonium suppression in the hadronic medium compared to the QGP. As in the QGP, Ψ can also be regenerated in the hadronic matter [63]; their regeneration rates can be obtained from their dissociation rates using the principle of detailed balance.

E. Charmonium Spectral Function

So far we have obtained the charmonium binding energy ϵ_B and in-medium charm quark mass m_c^* (from the potential model) and its dissociation rate (from quasifree approximation in QGP and $SU(4)$ effective theory in HG). The charmonium binding energy ϵ_B and in-medium charm quark mass m_c^* allow us to infer the charmonium pole mass via m_Ψ=2m_c^*-ϵ_B. These pieces of information figure into the charmonium spectral function, Eq. (1.20), which is the imaginary part of the Fourier transform of the charmonium current-current correlation function, Eq. (1.19). Due to current limitations mentioned in Section I.D, we can not reliably extract the charmonium spectral function from the charmonium current-current correlation function calculated by lattice QCD. However, we can still utilize the rather precise correlator ratios, Eq. (1.24), as a constraint on the consistency among the charmonium pole mass, binding energy and its dissociation rate.

To be specific we adopt the following strategy: We "reconstruct" in-medium charmonium spectral functions using a relativistic Breit-Wigner + continuum ansatz, where the Ψ width and mass figure into the Breit-Wigner part while the continuum is determined by the open-charm threshold ($2m_c^*$). For a more realistic evaluation, we include a polestrength factor, $Z_\Psi(T)$, for the Breit-Wigner strength and a non-perturbative rescattering enhancement in the continuum [64, 65]. The vanishing of the polestrength factor furthermore serves to estimate the dissociation temperature of the ground state in each channel.

We first construct a model spectral function in vacuum, consisting of a zero-width bound-state and a perturbative (leading order) continuum part,

$$\sigma_\Psi(\omega) \;=\; A_\Psi \;\delta(\omega - m_\Psi) + \frac{B_\Psi N_c}{8\pi^2}\Theta(\omega - \sqrt{s_0})\omega^2\sqrt{1-\frac{s_0}{\omega^2}}(a + b\frac{s_0}{\omega^2}) \;. \quad (3.21)$$

Here, N_c=3 is the number of colors and the coefficients $(a,b) = (1,-1),(2,1)$ characterize the scalar and vector channel, respectively [66]. The open-charm threshold in vacuum, $\sqrt{s_0}$, is assumed to be given by twice the free D-meson mass, $\sqrt{s_0} \equiv 2m_D = 3.74\,\mathrm{GeV}$. The coefficient A_Ψ is related to the overlap of the wave-function, $R_{J/\psi}(0)$, or its derivative, $R'_{\chi_c}(0)$, at the origin [66, 67],

$$A_{J/\psi} = \frac{3N_c}{2\pi}|R_{J/\psi}(0)|^2 \;, \quad A_{\chi_c} = \frac{36N_c}{2\pi M_{\chi_c}^2}|R'_{\chi_c}(0)|^2 \;. \quad (3.22)$$

These quantities can be estimated from the electromagnetic decays widths via [67]

$$\Gamma_{ee} = \frac{4e_Q^2\alpha^2 N_c}{3m_{J/\psi}^2}|R_{J/\psi}(0)|^2 \;,\; \Gamma_{\gamma\gamma} = \frac{144e_Q^4\alpha^2 N_c}{m_{\chi_c}^4}|R'_{\chi_c}(0)|^2 \quad (3.23)$$

where α=1/137 is the electromagnetic coupling constant and $e_Q = 2/3$ the charge of the charm quark (we use Γ_{ee}=5.55 keV for the J/ψ and $\Gamma_{\gamma\gamma}$=2.40 keV for the χ_{c0}).

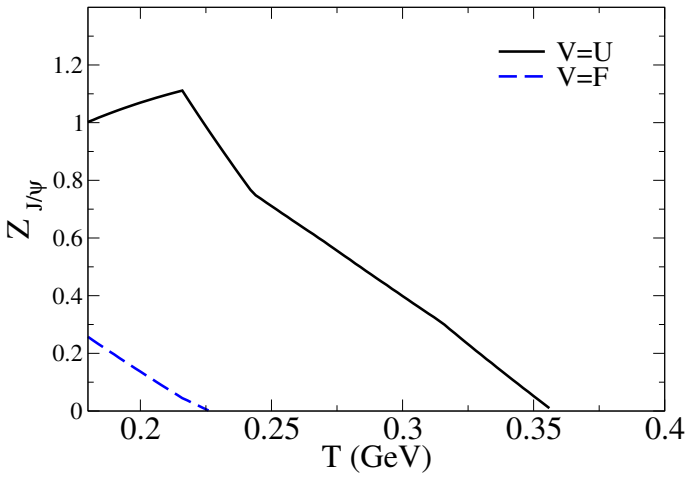

Fig. 24. Temperature dependence of the strength of the resonance part of the S-wave spectral function, $Z_\Psi(T)$, for the strong (solid line) and weak (dashed line) binding scenarios.

The resulting relations between A_Ψ and $\Gamma_{\Psi\to ee,\gamma\gamma}$ are

$$A_{J/\psi} = \frac{81 m_{J/\psi}^2}{32\pi\alpha^2}\,\Gamma_{ee}\ , \quad A_{\chi_c} = \frac{81 m_{\chi_{c0}}^2}{128\pi\alpha^2}\,\Gamma_{\gamma\gamma}\ . \tag{3.24}$$

The free J/ψ and χ_{c0} masses are taken at their empirical vacuum values. The coefficient B_Ψ in the continuum part of Eq. (3.21) equals to one in the non-interacting limit. To account for rescattering, which is particularly important close to threshold, we scale it up to match the continuum as calculated from the vacuum T-matrix in Ref. [50], amounting to $B_{J/\Psi} \simeq 2$ and $B_{\chi_c} \simeq 4$ in the vector and scalar channel, respectively. For simplicity we neglect ψ', χ_c' and higher excited states which play little role in the correlator ratios, Eq. (1.24).

At finite temperature we replace the δ-function bound-state part by a relativistic Breit-Wigner (RBW) distribution while the continuum part is assumed to be of the

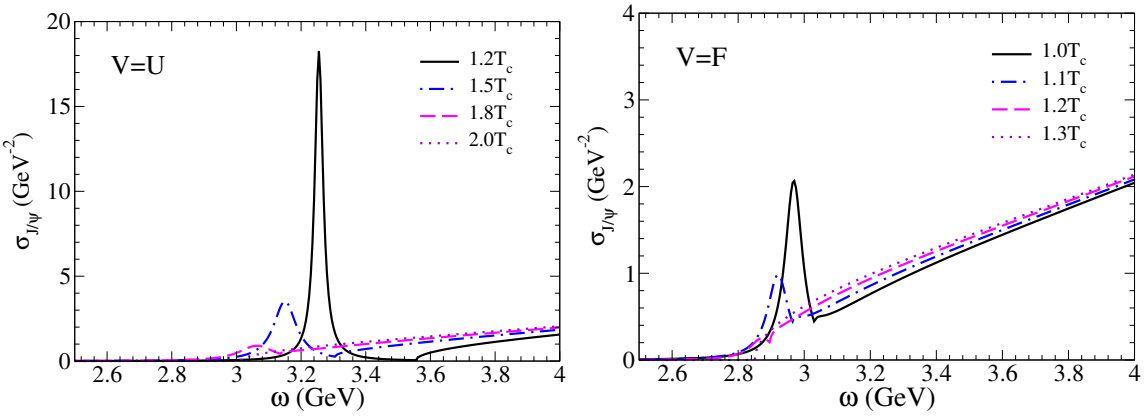

Fig. 25. Spectral functions in the vector channel for the strong (left panel) and weak (right panel) binding scenarios.

same form as in the vacuum,

$$\sigma_\Psi(\omega) = A_\Psi \; Z_\Psi(T)\frac{2\omega}{\pi}\frac{\omega\Gamma_\Psi(T)}{(\omega^2 - m_\Psi^2(T))^2 + \omega^2\Gamma_\Psi(T)^2} + \frac{B_\Psi N_c}{8\pi^2}\Theta(\omega - \sqrt{s(T)})\omega^2\sqrt{1-\frac{s(T)}{\omega^2}}(a + b\frac{s(T)}{\omega^2}) \; . \tag{3.25}$$

The in-medium continuum edge, $s(T)$, is now taken as the charm quark threshold at finite temperature, $\sqrt{s(T)} \equiv 2m_c^*(T)$, consistent with the potential model, see Fig. 16. The RBW term includes: (i) the in-medium charmonium mass, $m_\Psi(T)$, extracted from Eq. (3.1) based on Figs. 16 and 17; (ii) the width Γ_Ψ identified with the inelastic dissociation width discussed in the previous section; (iii) the aforementioned polestrength factor, $Z_\Psi(T)$, representing the modification of the strength of the bound-state part at finite temperatures relative to its vacuum value (A_Ψ), with $Z_\Psi|_{T=0}$=1. The $Z_\Psi(T)$ is adjusted to minimize the deviation of the correlator ratios from one.

The resulting $Z_\Psi(T)$ for J/ψ (vector channel) is plotted in Fig. 24, from which we extract its dissociation temperature $T_{J/\psi}^{\rm diss}$=2.0(1.25)T_c in the strong (weak) binding scenario. Similar analysis in the scalar channel yields χ_c dissociation temperatures

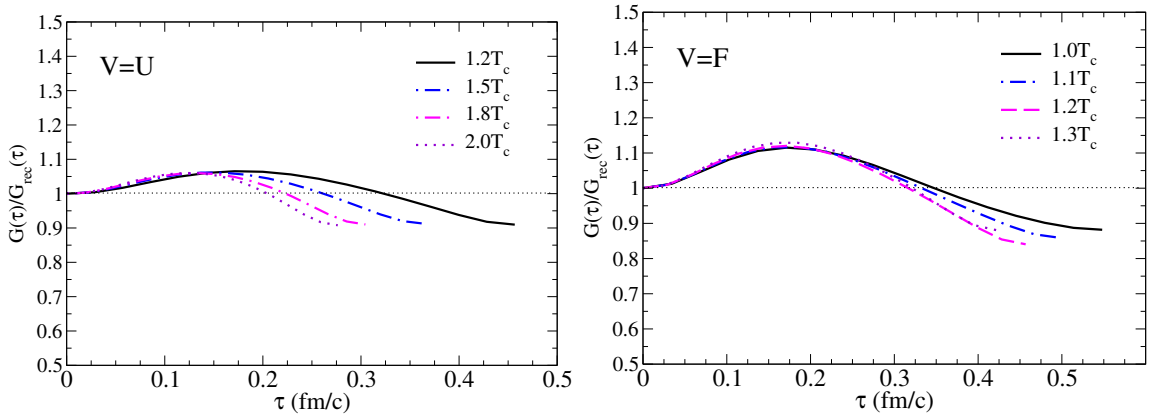

Fig. 26. Ratio of vector channel correlator to the reconstructed correlator for the strong (left panel) and weak (right panel) binding scenarios.

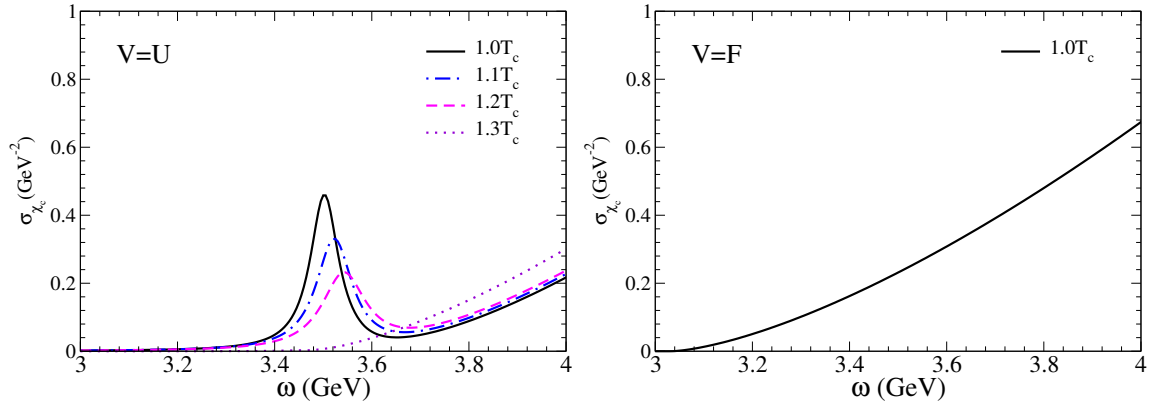

Fig. 27. Spectral functions in the scalar channel. The left (right) panel is for the strong (weak) binding scenario. In the weak-binding scenario χ_{c0} has already melted at T_c.

of $T_{\chi_c}^{\rm diss}$=1.3(1.0)T_c in the strong (weak) binding scenarios. We assume that χ_{c1} and χ_{c2} have the same dissociation temperatures as the χ_{c0}. For ψ' we simply assume its dissociation temperature to be T_c for both the strong- and weak-binding scenarios.

To comprehensively illustrate the medium effects we plot the final spectral functions for the vector channel in the strong- and weak-binding scenario in the QGP in Fig. 25, and their corresponding correlator ratios in Fig. 26; the spectral functions for the scalar channel are displayed in Fig. 27.

We see that the correlator ratios are indeed close to one, as found in lQCD [31, 30, 29]. In the hadronic phase (not shown), we assume vacuum masses for both charmonia and open-charm hadrons, which automatically ensures that the correlator ratios are close to one (deviations due to small charmonium widths in hadronic matter are negligible).

CHAPTER IV

THERMAL FIREBALL DESCRIPTION OF MEDIUM EVOLUTION

To solve the kinetic equation for the charmonium (Ψ=J/ψ, χ_c, ψ') evolution we need a description of the expanding medium in heavy-ion collisions. In particular, the temperature and the volume of the medium at any given time are required for estimating parton density and charm quark density, respectively, which are essential components for calculating the Ψ dissociation and regeneration rates. The traditional approaches describing the medium evolution include transport models, see Refs. [68, 69] for reviews, and relativistic hydrodynamics, see [70] for a review. In this work we however describe the medium evolution with a fireball model [71, 72] which is simpler yet captures the basic features of relativistic hydrodynamics. In Section IV.A we discuss the fireball description of the spatial expansion of the medium. In Section IV.B we discuss the equation of the state of the medium and extract the temperature of the fireball. In Section IV.C we review the popular blastwave formula for estimating particle p_t spectra with local thermal distributions boosted by the collective flow of the expanding source.

A. Fireball Expansion Profile

The fireball model approximates the medium created in heavy-ion collisions as a boost-invariant thermal fireball. The "boost-invariance" originates from the experimental fact that the rapidity (y) distribution of the charged particles, dN_{ch}/dy, is constant in the mid-rapidity ($y \sim 0$) region. This means that the medium in the central region is invariant under Lorentz boosts in the longitudinal (z) direction, which further implies that all thermodynamic quantities characterizing the central region depend only on the longitudinal proper time τ=$\sqrt{t^2 - z^2}$, recall Fig. 7.

The fireball volume, $V_{FB}(\tau)$, expands cylindrically according to

$$V_{FB}(\tau) = (z_0 + v_z\tau + \frac{1}{2}a_z\tau^2)\ \pi\ \left(r_0 + \frac{\sqrt{1+a_\perp^2\tau^2}-1}{a_\perp}\right)^2 \tag{4.1}$$

with expansion parameters $v_z, a_z, a_\perp$ chosen so that the results are consistent with the experimental data on the final light-hadron flow and resemble the evolution by hydrodynamical calculations. The relativistic form of transverse acceleration $(\sqrt{1+a_\perp^2\tau^2}-1)/a_\perp$ limits the surface speed, $v_s(\tau)$, to below the speed of light in the large τ limit. For small τ it recovers the non-relativistic form with constant transverse acceleration, $v_s(\tau) \sim a_\perp\tau$. Note that the fireball expansion profile, Eq. (4.1), depends only on the longitudinal proper time, $\tau{=}\sqrt{t^2-z^2}$, and not separately on t or z, as required by the boost invariance of the medium.

The initial transverse radius r_0 represents the initial transverse overlap of the two colliding nuclei at a given impact parameter b, while the initial longitudinal length, z_0, is related to thermalization time τ_0 through $z_0 \simeq \Delta y\tau_0$ where $\Delta y{=}1.8$ represents the typical longitudinal rapidity coverage of a thermal fireball. We assume that at a formation time of $\tau_0{=}1.0\ (0.6)\,\mathrm{fm}/c$ the medium at SPS (RHIC) first thermalizes with all the entropy, $S_{\mathrm{tot}}(b)$, being built up. The latter is estimated from the multiplicities of observed charged particles and assumed to be conserved during the adiabatic expansion.

B. Equation of State of the Medium

To determine the temperature of the system we utilize the equation of state (EoS) of the medium. An important insight from the success of the ideal hydrodynamic description of the medium evolution is that the total entropy of the system is conserved. Together with the information of the fireball expansion profile the entropy

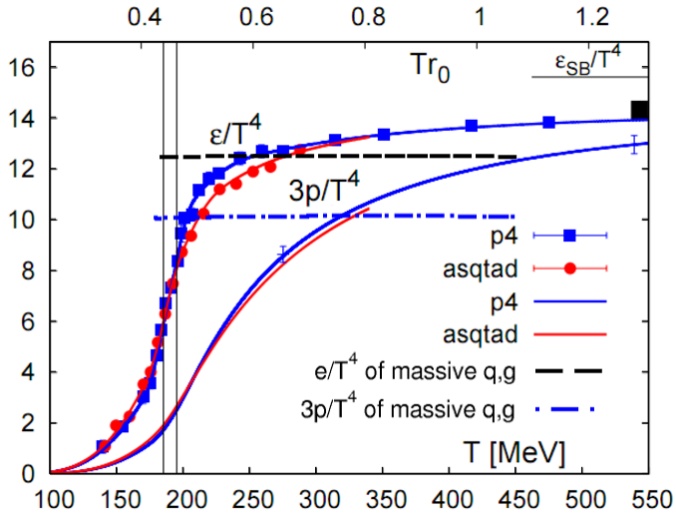

Fig. 28. Comparison of energy density from an ideal massive parton gas with data from lattice QCD [5]. Dashed (dot-dashed) line: energy density (pressure) calculated from an ideal massive quark and gluon gas with g_s=2.3.

density of the fireball at each given moment can be obtained. This quantity allows us to estimate the temperature of the fireball through comparison with the thermodynamic equation of state (the entropy density as a function of the temperature, T). In QGP we model the medium by an ideal gas of massive quarks and gluons, with the entropy density as a function of temperature given by

$$s(T) = \sum_i \frac{d_i}{(2\pi)^3} \int d^3k [\pm(1\pm f_i(k;T))\log(1\pm f_i(k;T)) - f_i(k;T)\log f_i(k;T)] \ , \quad (4.2)$$

where d_i is the color-spin degeneracy of partons, the $f_i(k;T)$ are the thermal distributions for massive quarks and gluons, given by Eqs. (3.4) and (3.3) respectively, and the plus sign in "$\pm$" is taken for gluons (i=g) and the minus sign is taken for quarks (i=$q,\bar{q}$). For the temperature dependence of thermal quasiparticle masses $m_i(T)$ we take guidance from pQCD calculation, see Eqs. (3.5), (3.6) and (3.7). The strong coupling constant g is estimated by matching the resulting energy density of the parton gas to lQCD calculations, see Fig. 28, resulting in $g_s \sim$2.3. Note that this g is decou-

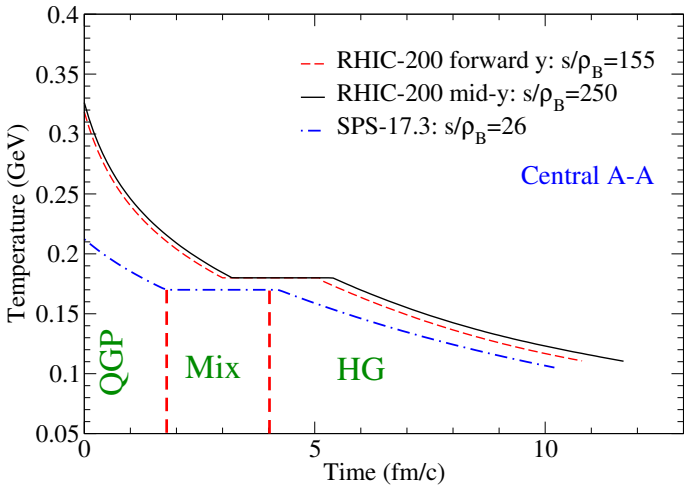

Fig. 29. Time profiles of temperature for central collisions of heavy nuclei (participant number $N_{\rm part}$=380) at RHIC ($\sqrt{s}$=200 AGeV; solid line: mid rapidity; dashed line: forward rapidity) and SPS ($\sqrt{s}$=17.3 AGeV; dot-dashed line).

pled from the α_s in the quasifree dissociation cross section. In the hadronic medium an EoS similar to Eq. (4.2) is employed but including 76 mesonic and baryonic states up to masses of 2 GeV. For particles which do not decay strongly, *e.g.*, pion, kaon, antiproton, we include their corresponding chemical potentials to maintain their abundances when the system cools down from chemical to thermal freeze-out [71]. The critical temperature, T_c=170 (180) MeV at SPS (RHIC), is roughly consistent with thermal-model fits to observed particle ratios [73] and predictions of lattice QCD [74]. A freeze-out temperature of $T_{\rm fo} \simeq 120$ MeV terminates the evolution and results in a total fireball lifetime of $\tau_{\rm fo}$=10-12 fm/c for central A+A collisions. The resulting temperature evolution as a function of time τ is displayed in Fig. 29 for SPS and RHIC. Note that there is little difference between mid ($|y| < 0.35$) and forward rapidity ($|y| \in [1.2, 2.2]$) for Au+Au collisions at RHIC due to the slowly varying rapidity density of charged particles over this y range [75], cf. Ref. [76] for more details.

For heavy-ion collisions with lower center-of-mass (cms) energies, *e.g.*, at the

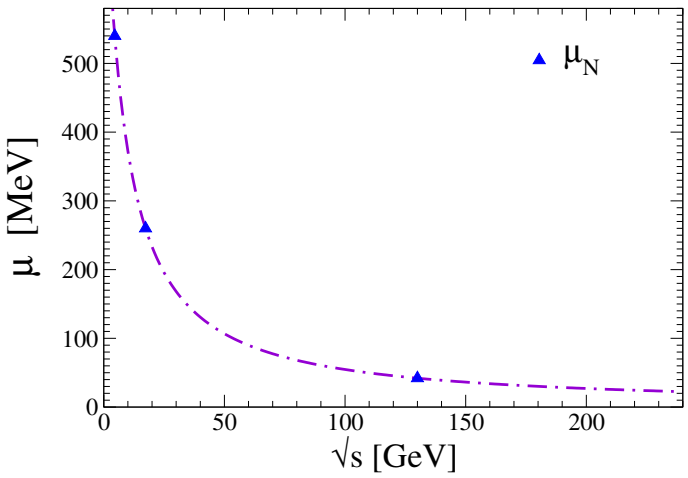

Fig. 30. Excitation function of the baryon chemical potential $\mu_B(T_c)$ at the assumed phase transition line. The points correspond to values extracted from particle ratios.

future FAIR facility, stronger stopping of incoming nuclei entails the medium to be more asymmetric in terms of the net baryon number, corresponding to a larger baryon chemical potential μ_B, see Fig. 30, and lower initial temperature, T. In this regime the thermodynamic properties of the medium are characterized by both T and $\mu_B(\gtrsim T)$. In order to determine the temperature evolution in such systems we resort to a second conserved quantity during the fireball evolution, which is the net baryon number, N_B. With both baryon density, n_B, and entropy density, s, given at each time we are able to solve for $\mu_B(\tau)$ and $T(\tau)$ by using

$$s(T,\mu_B) = \sum_i \frac{d_i}{(2\pi)^3}\int d^3k[\pm(1\pm f_i(k;T,\mu_B))\log(1\pm f_i(k;T,\mu_B)) - f_i(k;T,\mu_B)\log f_i(k;T,\mu_B)]\ , \tag{4.3}$$

$$n_B(T,\mu_B) = \sum_i \frac{d_i}{3\times(2\pi)^3}\int d^3k[(f_q(k;T,\mu_B) - f_{\bar{q}}(k;T,\mu_B)]\ , \tag{4.4}$$

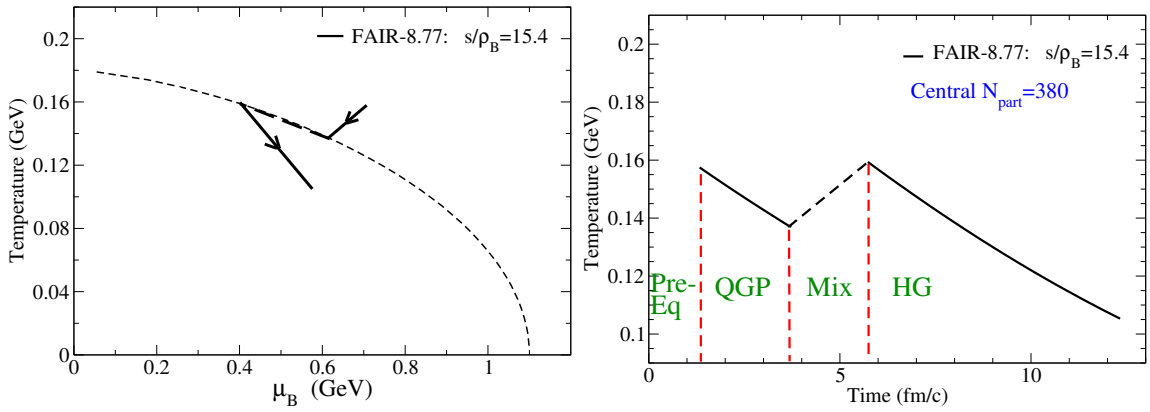

Fig. 31. Temperature evolution of heavy-ion collisions at FAIR. Left panel: Trajectory of heavy-ion collisions on the QCD phase diagram at FAIR ($\sqrt{s}$=8.8AGeV). Right panel: Time profile of temperature for central collisions of heavy nuclei (participant number N_{part} =380) at FAIR ($\sqrt{s}$=8.8AGeV).

The thermal quark distributions at finite μ_B are

$$f_q(k;T,\mu_B) = \frac{1}{\exp\left(\frac{\sqrt{k^2+m_i^2}-\mu_B/3}{T}\right)+1}$$
$$f_{\bar{q}}(k;T,\mu_B) = \frac{1}{\exp\left(\frac{\sqrt{k^2+m_i^2}+\mu_B/3}{T}\right)+1} \,. \tag{4.5}$$

As part of the EoS of the system, the phase boundary $\mu_B(T_c)$ (instead of a single T_c) is determined with guidance from thermal-model fits to observed particle ratios at various center-of-mass energies [73], see Figs. 30 and 31.

The resulting time evolution of the fireball is characterized by a trajectory in the QCD phase diagram at fixed s/n_B ratio, see the left panel of Fig. 31. We note the zigzag structure of the trajectory, which reflects the fact that the medium is reheated by the latent heat when it undergoes the phase transition, as first pointed out in Ref. [77].

The resulting temperature evolution as a function of time τ for central Pb+Pb

collisions at FAIR energies is displayed in the right panel of Fig. 31. The thermalization time τ_0 is assumed to be 1.3fm/c at FAIR energies. With an initial temperature lower than 160 MeV the QGP phase still lasts for 1-2fm/c, which is followed by the mixed phase with duration of around 2fm/c. The overall fireball lifetime is again around 10fm/c.

C. Blastwave Description of Charmonium p_t Spectra

In addition to the temperature evolution profile the thermal fireball model allows to define a flow field, which enables us to estimate the transverse momentum (p_t) spectra of locally (kinetically) thermalized particles, boosted by the flow field. Historically this analysis was developed by Siemens and Rasmussen [78], and is referred to as the blastwave model. Later the blastwave model in a boost-invariant medium was developed by Schnedermann, Sollfrank and Heinz [79]. Here we follow Ref. [79] and briefly review the derivation of the "blastwave formula".

Since the medium is not static in the lab frame we employ the Cooper-Frye formula [80] to count the particle number in the freeze-out hyper-surface,

$$E\frac{dN}{d^3p} = \frac{1}{(2\pi)^3}\int d\Sigma_\mu(x)p^\mu f(x,p) = \frac{d}{(2\pi)^3}\int d\Sigma_\mu(x)p^\mu e^{-p\cdot u/T} \ . \tag{4.6}$$

Here the Σ_μ is the freeze-out hyper-surface, u^μ is the four velocity of a given medium cell, and $f(x,p)$=$d\, e^{-p\cdot u/T}$ is the thermal particle distribution in the local rest frame with d being the degeneracy factor.

Since the freeze-out is commonly assumed to occur at fixed longitudinal proper time, τ=$\sqrt{t^2-z^2}$, it is convenient to parameterize the freeze-out hyper-surface by

$$x^\mu = (\tau_{fo}\cosh\eta, r\cos\phi, r\sin\phi, \tau_{fo}\sinh\eta) \ , \tag{4.7}$$

where η=$\tanh^{-1}(z/t)$ is the space-time rapidity. The volume element of the hypersurface is therefore

$$d\Sigma^{\mu} = \tau_{fo}\,(\cosh\eta, 0, 0, \sinh\eta)\, r\ dr\ d\eta\ d\phi\ . \tag{4.8}$$

The particle four-momentum can be parameterized as

$$p^{\mu} = (m_t \cosh y, p_t \cos\phi_p, p_t \sin\phi_p, m_t \sinh y)\ \ , \tag{4.9}$$

where y=$\tanh^{-1}(p_z/E)$ is the momentum rapidity of the particle and m_t=$\sqrt{m^2+p_t^2}$ its transverse mass. Therefore we have

$$p\cdot d\Sigma = \tau_{fo} m_t \cosh(y-\eta) r dr d\eta d\phi\ . \tag{4.10}$$

A parameterization of the four-velocity u^{μ} of a medium cell can be written as

$$u^{\mu} = \left(\cosh\rho\cosh y^{cell}, \sinh\rho\cos\phi_p, \sinh\rho\sin\phi_p, \cosh\rho\sinh y^{cell}\right)\ . \tag{4.11}$$

Here $y^{cell} = \tanh^{-1}(v_z^{cell})$ is the longitudinal rapidity of a medium cell. According to boost-invariant condition ($v_z^{cell} = z/t$), it is equal to the longitudinal space-time rapidity, namely, $y^{cell} = \eta$; ρ=$\tanh^{-1}(v_{\perp}^{cell})$ is the transverse rapidity of the medium cell. Therefore the four product $p\cdot u$ can be expressed as

$$p\cdot u = m_t \cosh\rho\cosh(\eta - y) - p_t \sinh\rho\cos(\phi-\phi_p)\ . \tag{4.12}$$

Plugging Eqs. (4.10) and (4.12) into Eq. (4.6) we obtain the one particle momentum

spectrum in the lab frame

$$E\frac{dN}{d^3p} = \frac{d}{(2\pi)^3}\int_0^{2\pi} d\phi \int_{-\infty}^{\infty} d\eta \int_0^R r dr$$
$$\times \tau_{fo} m_t \cosh(y-\eta) \exp[(-m_t \cosh\rho \cosh(\eta - y) + p_t \sinh\rho \cos(\phi - \phi_p))/T] \ . \tag{4.13}$$

After the integration over η and ϕ is performed we arrive at the blastwave formula,

$$E\frac{dN}{d^3p} = \frac{dN}{dyd^2p_t} = \frac{d}{2\pi^2}\tau_{fo} m_t \int_0^R r dr K_1(\frac{m_t \cosh\rho}{T}) I_0(\frac{p_t \sinh\rho}{T}) \ . \tag{4.14}$$

Here K_1 and I_0 are modified Bessel functions. The transverse rapidity of a medium cell ρ=$\tanh^{-1}(v_\perp^{cell})$ is given by the fireball model by assuming a linear transverse flow profile with

$$v_\perp^{cell}(\vec{r}) = \frac{r}{R} v_s \ , \tag{4.15}$$

where R is the radius of the fireball and $v_s(\tau)$=$a_\perp \tau$ is the transverse flow velocity at the surface of the fireball.

In Chapter VI we will utilize the blastwave formula to estimate the transverse momentum spectra of Ψ regenerated from thermal charm quark spectra.

CHAPTER V

PRIMORDIAL CHARMONIUM PRODUCTION

The central purpose of studying charmonium production in heavy-ion collisions is to utilize charmonium as a probe of the hot and dense medium. Therefore charmonium production in the pre-equilibrium stage is necessary as a baseline for assessing any modifications due to the hot medium. Since charm-anticharm production is a hard process at SPS and RHIC (the production time of charm quark pair, $\tau^{c\bar{c}} \sim$0.07fm/c, is shorter than nucleus passage time, $\tau_{pass} \sim$0.13fm/c at RHIC), it can be approximated as superposition of production in elementary nucleon-nucleon collisions. Thus, in a first approximation, the initially produced charmonia in A+A collisions can be estimated from their production in p+p collisions (scaled by the number of binary nucleon-nucleon collisions in an A+A collision). The main purpose of this chapter is to apply further corrections specific for p+A and A+A collisions. These corrections are usually referred to as cold nuclear matter (CNM) effects. We first give an overview of charmonium production in p+p collisions in Section V.A. Then we proceed to the CNM effects in Section V.B.

A. Charmonium Production in p+p Collisions

In p+p collisions charmonia are produced in two steps:

1) The $c\bar{c}$ pairs are produced through hard collisions (with large momentum transfer) between the partons from the two colliding protons. The leading order processes in pQCD include the gluon fusion (dominating at high energies) and quark annihilation,

$$g + g \to c + \bar{c}, \qquad q + \bar{q} \to c + \bar{c}\ . \tag{5.1}$$

As hard processes the $c\bar{c}$ production cross section in p+p collisions can be factorized into a convolution of incoming parton distribution function, $f_i(x, Q^2)$, and the parton scattering cross section, $\sigma^{ij\to[c\bar{c}]}(x_1, x_2, Q^2)$, to yield,

$$\sigma^{NN\to[c\bar{c}]}(Q^2) = \int_0^1 dx_1 \int_0^1 dx_2 \sum_{i,j} f_i(x_1, Q^2) f_j(x_2, Q^2) \sigma^{ij\to[c\bar{c}]}(x_1, x_2, Q^2) \ . \quad (5.2)$$

Here, x_1 and x_2 are the momentum fractions of the two colliding partons within the two colliding protons. The large virtuality, Q^2, allows us to compute the partonic cross-section, $\sigma(x_1, x_2, Q^2)$, as a perturbative expansion in powers of $\alpha_s(Q^2)$. According to the uncertainty principle the time scale of the perturbative partonic process is $\sim 1/Q$.

2) c and $\bar{c}$ quarks which are close to each other in the phase space ("pre-resonance" $c\bar{c}$ states) may develop into a charmonium state through non-perturbative "final-state" interactions. Compared to charm quark production this step is much slower, with a typical formation time for charmonium states on the order of $1/\epsilon_B^{\Psi} \gg 1/(2m_c)$. Calculations based on a non-relativistic Schrödinger equation suggest the typical formation time of charmonium states to be τ_Ψ ~1-2 fm/c [20]. Due to the large separation in the time scale the quantum interference between charm quark production and charmonium production is suppressed. Therefore the factorization between the charm quark production and charmonium production is usually assumed,

$$\sigma_{A+B\to\Psi+X} \approx \sum_n \int d\Phi_{c\bar{c}} \ \sigma_{A+B\to c\bar{c}[n]+X}(\Phi_{c\bar{c}}, m_c) \ F_{c\bar{c}[n]\to\Psi}(\Phi_{c\bar{c}}) \ , \quad (5.3)$$

with a sum over possible $c\bar{c}[n]$ states and an integration over available $c\bar{c}$ phase space $d\Phi_{c\bar{c}}$; F represents a non-perturbative transition probability for a pair of off-shell $c\bar{c}$ to a charmonium state, Ψ. The microscopic mechanisms for this transition are still under debate. Three widely discussed models in the literature are the color

evaporation model (CEM), the color singlet model (CSM) and the non-relativistic QCD (NRQCD) model.

The CEM [81, 82, 83] assumes that all $c\bar{c}$ pairs with invariant mass less than the threshold of producing a pair of open-charm mesons, regardless of their color, spin, and invariant mass, have the same probability to become a charmonium. That is, the $F_{c\bar{c}[n]\to\Psi}$ in Eq. (5.3) is a constant for a given quarkonium state, which is usually obtained by a fit to the data.

The CSM [84, 85, 86, 87, 88] assumes that only a color-singlet charm quark pair with the right quantum number can become a charmonium of the same quantum number and the transition from the pair to a meson is given by the charmonium wave function overlap at the origin.

The NRQCD model [67, 89, 90] allows every $c\bar{c}[n]$ state to become a bound charmonium, while the probability is determined by corresponding non-perturbative matrix elements $F_{c\bar{c}[n]\to\Psi}$. The $F_{c\bar{c}[n]\to\Psi}$ encoding the non-perturbative dynamics is expanded in terms of local matrix elements in a power series of the heavy quark velocity, v.

Each of these models has its advantages and limitations in explaining available experimental data, see Ref. [91] for a review. The Ψ production mechanisms in p+p collisions also have influence on Ψ production in A+A collisions. For example, recent RHIC measurements [92, 93] found a reduced suppression for high p_t J/ψ's compared to low p_t ones in A+A collisions, which lends support to the picture that the "pre-resonance" $c\bar{c}$ states are in a color-singlet state, see Section VI.B.2.b for a more detailed discussion.

Since our purpose is to utilize charmonium as a probe to the hot medium we rely on experimental values on J/ψ and $c\bar{c}$ production in p+p collisions as the baseline for assessing in-medium physics in A+A collisions. For the p+p charmonium production

cross per unit rapidity we take the values $\mathrm{d}\sigma^{\Psi}_{pp}/dy$=37 nb [94] for $\sqrt{s}$=17.3 AGeV Pb-Pb [94] (with ca. 40% uncertainty) and $\mathrm{d}\sigma^{\Psi}_{pp}/dy$=750(500) nb for $\sqrt{s}$=200 AGeV Au-Au [95] at mid and forward rapidity (with ca. 10(20)% uncertainty). The input charm quark N+N cross section at SPS energy, $\mathrm{d}\sigma_{\bar{c}c}/\mathrm{d}y$ (y=0)=2.2 μb, is taken from a recent compilation of experimental data in Ref. [96]. For full RHIC energy, we use $\mathrm{d}\sigma_{\bar{c}c}/\mathrm{d}y$ (y=0)=123$\pm$40μb, in line with recent PHENIX measurements [97]. We reduce the input charm quark cross section at forward rapidity by 1/3, $\mathrm{d}\sigma^{\bar{c}c}_{pp}/\mathrm{d}y$ (y=1.7)=$\frac{2}{3}\mathrm{d}\sigma^{\bar{c}c}_{pp}/\mathrm{d}y(y$=0), according to recent experimental data [98].

B. Charmonium Production in A+A Collisions

After having fixed charmonium production in p+p collisions the next step is to scale it by the number of binary nucleon-nucleon (N+N) collisions, N_{coll}, to estimate charmonium primordial production in A+A collisions, which is a standard procedure for a hard probe. N_{coll} is usually calculated with the Glauber model, which plays an important role in connecting p+p and A+A collisions. Below we briefly review the main results from the (optical) Glauber model which are needed in this work. The emphasis is placed on concepts relevant for Ψ production, for a more comprehensive review of the Glauber model, see Ref. [99].

1. Brief Review of Glauber Model

In this section we give a brief review of the Glauber model and introduce two important quantities linking A+A collisions with elementary nucleon-nucleon (N+N) collisions: 1) the number of binary collisions, N_{coll}, 2) the number of participants or wounded nucleons, N_{part}, which are nucleons from the projectile or the target which suffer at least one inelastic collision. In the Glauber model the collision between two

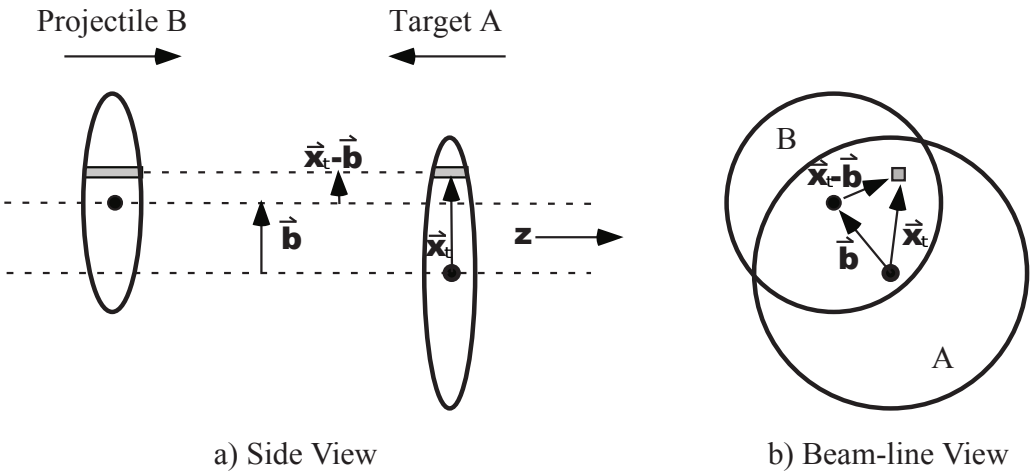

Fig. 32. Schematic representation of the geometry of Glauber model. Left panel: transverse view. Right panel: longitudinal view. The picture is taken from Ref. [99].

nuclei, A and B, consisting of A and B nucleons, respectively, is considered as a superposition of (binary) collisions of the individual incoming nucleons. The geometry of the Glauber model is schematically sketched in Fig. 32.

The inputs of the Glauber model are 1) nuclear charge densities, usually taken as a Wood-Saxon density profile,

$$\rho(r) = \frac{\rho_0}{1+\exp\left(\frac{r-R}{a}\right)} \ , \tag{5.4}$$

where ρ_0=0.17 fm^{-3} is the nucleon density in the center of the nucleus, R is the nuclear radius and a is the thickness of the nuclear skin. For ^{197}Au, R=6.38 fm, a=0.535 fm. For ^{208}Pb, R=6.62 fm, a=0.549 fm [100]; 2) Inelastic nucleon-nucleon cross section, σ_{inel}^{NN}, which can be obtained from experimental measurements, *e.g.*, σ_{inel}^{NN}=30(42) mb at SPS (RHIC) [17].

The nuclear thickness function,

$$T_A(\vec{x}_t) = \int dz \ \hat{\rho}_A(\vec{x}_t, z) \ , \tag{5.5}$$

can be interpreted as the probability of finding a nucleon within a unit transverse area at $\vec{x}_t$ of nucleus A. The $\hat{\rho}_A$ is the nuclear density in Eq. (5.4) normalized to 1, namely,

$$\int \hat{\rho}_A d^2x_t dz = \frac{1}{A}\int \rho_A d^2x_t dz \ = 1 \ . \tag{5.6}$$

Therefore $T_A(\vec{x}_t)T_B(\vec{x}_t - \vec{b})$ is the joint probability of finding a pair of nucleons from nuclei A and B, respectively, within the common unit transverse area at $\vec{x}_t$. Their corresponding number of collisions is given by $T_A(\vec{x}_t)T_B(\vec{x}_t - \vec{b})\sigma_{\rm inel}^{\rm NN} d^2x_t$. Integrating over the transverse plane we obtain the total number of collisions contributed by this pair,

$$N_{\rm coll}^{pair}(b) = \sigma_{\rm inel}^{\rm NN}\, T_{AB}(b) = \sigma_{\rm inel}^{\rm NN}\int T_A(\vec{x}_t)T_B(\vec{x}_t - \vec{b})\ d^2x_t \ , \tag{5.7}$$

where $T_{AB}(b)$ is called the nuclear overlap function. Since from the two nuclei A and B a total number of AB such pairs can be found and each of them contributes an equal number of collisions, we obtain the following expression for the total number of binary collisions

$$N_{\rm coll}(b) = AB\, T_{AB}(b)\, \sigma_{\rm inel}^{\rm NN} \ . \tag{5.8}$$

The centrality of heavy-ion collisions is often expressed in terms of the number wounded nucleons (participants), $N_{\rm part}$. In the Glauber model, $N_{\rm part}$ can be estimated as follows: The probability for a given nucleon from nucleus A to be located at transverse position $\vec{x}_t$ is $T_A(\vec{x}_t)$, and the probability for this nucleon to collide with a nucleon from nucleus B (located at $(\vec{x}_t - \vec{b})$) is $T_A(\vec{x}_t)\, T_B(\vec{x}_t - \vec{b})\, \sigma_{\rm inel}^{\rm NN}$. The probability of not colliding is thus $T_A(\vec{x}_t)\,(1 - T_B(\vec{x}_t - \vec{b})\, \sigma_{\rm inel}^{\rm NN})$. The probability of not colliding with any of the B nucleons from nucleus B is thus $T_A(\vec{x}_t)\,[1 - T_B(\vec{x}_t - \vec{b})\, \sigma_{\rm inel}^{\rm NN}]^B$. Therefore the probability for the nucleon at $\vec{x}_t$ suffering at least one collision is $T_A(\vec{x}_t)\,(1 - [1 - T_B(\vec{x}_t - \vec{b})\, \sigma_{\rm inel}^{\rm NN}]^B)$. Integrating over the transverse plane we obtain

the probability for a given nucleon in nucleus A suffering at least one collision,

$$P_{wo}^{A}(b) = \int T_A\left(\vec{x}_t\right) \left\{1 - \left[1 - T_B(\vec{x}_t - \vec{b})\, \sigma_{\rm inel}^{\rm NN}\right]^B\right\} d^2x_t \ . \tag{5.9}$$

Since there are $A(B)$ nucleons in nucleus A(B) we obtain the total number of wounded nucleons (participants) in A+B collisions at impact parameter b as

$$\begin{aligned} N_{\rm part}(b) &= A\ P_{wo}^{A}(b) + B\ P_{wo}^{B}(b) \\ &= A \int T_A\left(\vec{x}_t\right) \left\{1 - \left[1 - T_B\left(\vec{x}_t - \vec{b}\right) \sigma_{\rm inel}^{\rm NN}\right]^B\right\} d^2x_t \\ &\quad + B \int T_B\left(\vec{x}_t - \vec{b}\right) \left\{1 - \left[1 - T_A\left(\vec{x}_t\right) \sigma_{\rm inel}^{\rm NN}\right]^A\right\} d^2x_t \ . \end{aligned} \tag{5.10}$$

2. Cold Nuclear Matter Effects

The notion that Ψ production in A+A collisions can be viewed as superposition of independent N+N collisions is only approximately true. The deviation of primordial Ψ production in A+A from $N_{\rm coll}$-scaled p+p collisions is usually attributed to the so-called cold nuclear matter (CNM) effects.

In this section we examine the following three aspects of CNM effects: 1) Nuclear shadowing, 2) Cronin effect 3) Nuclear absorption. These CNM effects can, in principle, be estimated from p+A collisions where no hot medium is expected to form.

a. Nuclear Shadowing

It is a well-established fact that the partonic structure of high-energy nuclei is different from the incoherent superposition of the constituent nucleons, see Ref. [101] for a recent review. This modification is usually parameterized by

$$R_i^A(x, Q^2) = \frac{f_i^A(x, Q^2)}{A f_i(x, Q^2)} \ , \quad i = q, \bar{q}, g \ , \tag{5.11}$$

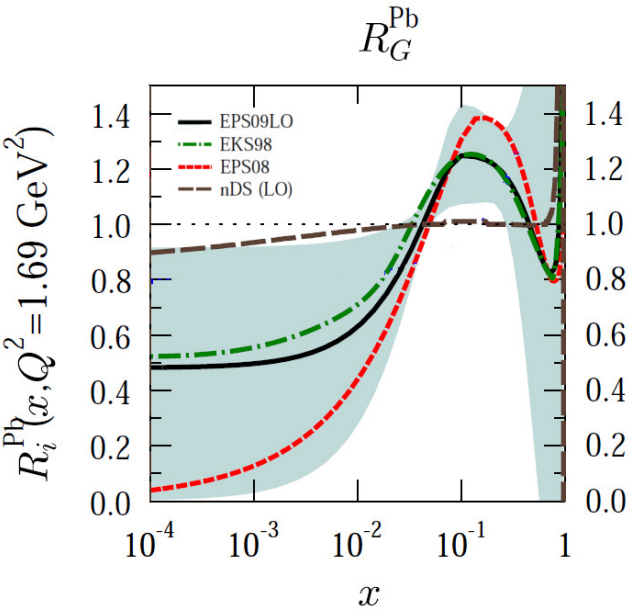

Fig. 33. Modification of parton distribution function in nucleus. Figure taken from Ref. [102].

defined as the ratio of the parton distribution function for a nucleon inside the nucleus (nPDF), $f_i^A(x,Q^2)$, to the corresponding one for a free proton (PDF), $f_i(x,Q^2)$, where x is the longitudinal momentum fraction of the parton within the nucleon. As illustrated in Fig. 33 different names have been assigned to these modifications depending on the relevant range of x under consideration: 1) *Shadowing* for the suppression observed at small ($x \lesssim 0.05$). 2) *Antishadowing* for the enhancement at moderate values of $0.05 \lesssim x \lesssim 0.3$. 3) *EMC effect* for the suppression observed in the region $0.3 \lesssim x \lesssim 0.7$; and 4) *Fermi motion* for the enhancement when $x \to 1$. Let us estimate the impact on charmonium production from the modification of nuclear parton distribution function by assuming that the initially produced charm quark pair has the same rapidity as the charmonium into which they evolve. Then the

momentum fraction of the incoming partons x is

$$x_{1,2} = \frac{m_t}{\sqrt{s_{NN}}} \exp(\pm y) \ , \tag{5.12}$$

with the transverse mass $m_t = \sqrt{m_\Psi^2 + p_t^2}$ of Ψ, and y being its momentum rapidity. In $\sqrt{s}$=17.3AGeV Pb+Pb collisions at SPS the relevant x ~0.2 is in the anti-shadowing region. In $\sqrt{s}$=200AGeV Au+Au collisions at RHIC, for charmonia produced at mid-rapidity, the relevant x for partons from both colliding nuclei is around 0.02, close to the transition from the shadowing to the anti-shadowing region. For charmonia produced at forward rapidity, y ~1.7, the x of the parton from the forward going (in the same direction with the produced Ψ) nucleus is around 0.1 (anti-shadowing region), while the x of the backward going parton is around 0.003 (shadowing region). In most parameterizations of nPDF, the shadowing of the backward parton is generally considered to be stronger than the anti-shadowing of the forward going parton, see Fig. 33. So the overall effect from the modification of parton distribution function is expected to cause suppression of Ψ production relative to p+p collisions. However, for high p_t Ψ produced at forward y at RHIC the x of the backward going parton could be shifted to 0.01 (for p_t=10 GeV), where the shadowing is small and could well be compensated by the anti-shadowing of the forward going parton. Therefore it is expected that for high p_t Ψ produced at forward y the suppression due to nuclear shadowing should be suppressed. The shadowing / anti-shadowing effects are experimentally observed in d+Au collisions at RHIC, see Fig. 34. The enhancement (suppression) of charmonia produced at backward (forward) rapidity is due to anti-shadowing (shadowing).

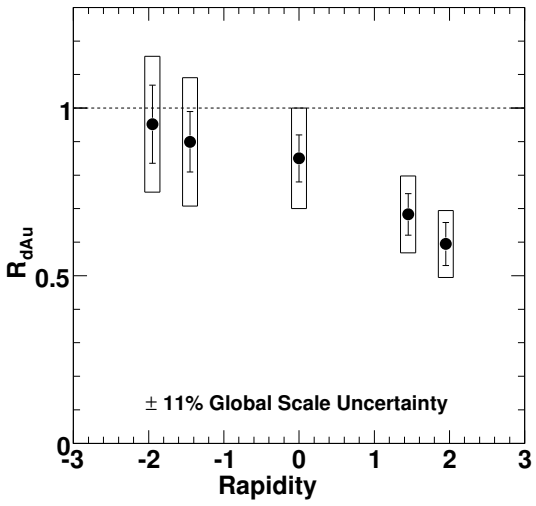

Fig. 34. Rapidity dependence of J/ψ R_{dAu} in d+Au collisions at $\sqrt{s}$=200AGeV measured by PHENIX [103].

b. Cronin Effect

The Cronin effect refers to an enhancement of hadron production at intermediate and high p_t in p+A relative to p+p collisions (scaled by $N_{\rm coll}$). This effect is generally attributed to multiple soft scatterings of the projectile partons propagating through the target nucleus before the hard scattering. From the transverse kicks in the soft scatterings the partons acquire additional $\langle p_t^2 \rangle$ and therefore the $\langle p_t^2 \rangle$ of the finally produced charmonia increases correspondingly. Fig. 35 illustrates the Cronin effect at SPS energies, where the $\langle p_t^2 \rangle$ of charmonium produced in p+A collisions increases with size of the colliding nucleus (approximated by the path length travelled by the colliding parton). The Cronin effect for J/ψ is currently difficult to quantify at RHIC energies due to large uncertainties associated with d+Au data.

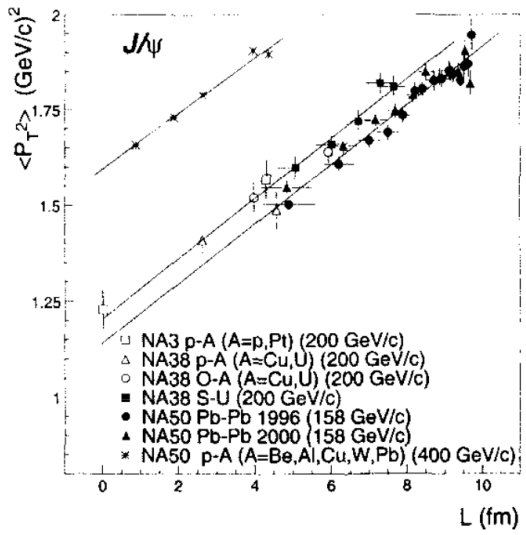

Fig. 35. $\langle p_t^2 \rangle$ of the J/ψ as a function of the geometric length of matter, L, traversed by partons in the initial state. The figure is taken from Ref. [104].

c. Nuclear Absorption

In p+A or A+A collisions the "pre-resonance" $c\bar{c}$ states (those $c\bar{c}$ pairs close to each other in phase space which would form charmonium if there were no rescattering off surrounding particles, *i.e.*, in p+p collisions) are subject to dissociation through inelastic collisions with passing-by nucleons before they are fully developed into charmonia. Nuclear absorption is observed in p+A collisions at SPS, where the energy deposited is too small to create a hot medium: charmonium production is substantially suppressed relative to ($N_{\rm coll}$ scaled) p+p collisions, see Fig. 36. At RHIC energy nuclear absorption is observed in d+Au collisions, see Fig. 37, which is weaker than at SPS, presumably because the time scale over which the two nuclei pass through each other ($2R/\gamma$, γ: Lorentz factor) is ten times shorter at RHIC. Therefore the "pre-resonance" $c\bar{c}$ states collide with passing-by nucleons shortly after their pair production, when they are still small in size (not far from their production vertex) and thus have a smaller dissociation cross section compared to at SPS energy.

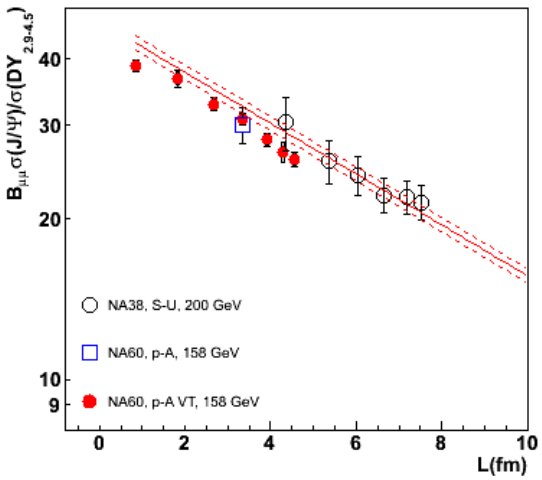

Fig. 36. J/ψ R_{AA} (normalized to Drell-Yan pairs) vs. L for various p+A and S+U systems. Note that this "L" is the effective average length travelled by (pre-) charmonium states, not by the initial state partons. This is different from the "L" in Fig. 35. The figure is taken from Ref. [105].

3. Implementation of CNM Effects

In our transport approach charmonium production in the pre-equilibrium stage serves as the initial condition for the evolution in the hot medium. For simplicity we assume that the initial phase space distribution of charmonia, $f(\vec{x}, \vec{p}, \tau_0)$, determined from Ψ production in the pre-equilibrium stage, can be factorized into coordinate and momentum spaces. According to boost-invariance we only need to consider the phase space distribution in the transverse plane,

$$f_\Psi(b, \vec{x}_t, \vec{p}_t, \tau_0) = f_\Psi(b, \vec{x}_t, \tau_0) f_\Psi(b, \vec{p}_t, \tau_0) \ . \tag{5.13}$$

Let us start with the spatial part, $f_\Psi(b, \vec{x}_t, \tau_0)$. The Glauber model tells us the initially produced charmonia distribution according to the nuclear overlap function, $f_\Psi(b, \vec{x}_t, \tau_0) \propto T_A(\vec{x}_t)\, T_B(\vec{x}_t - \vec{b})$. We augment it with the nuclear absorption: The probability for the dissociation of a pre-resonance $c\bar{c}$ state created at ($\vec{x}_t$,z_A) inside a

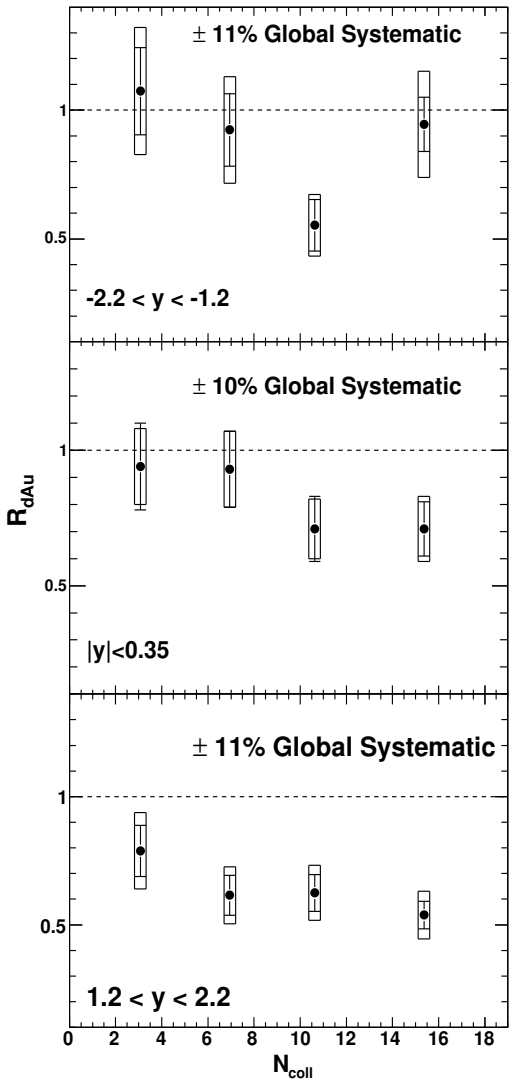

Fig. 37. Centrality dependence of J/ψ R_{dAu} in 200AGeV d+Au collisions measured by PHENIX [103].

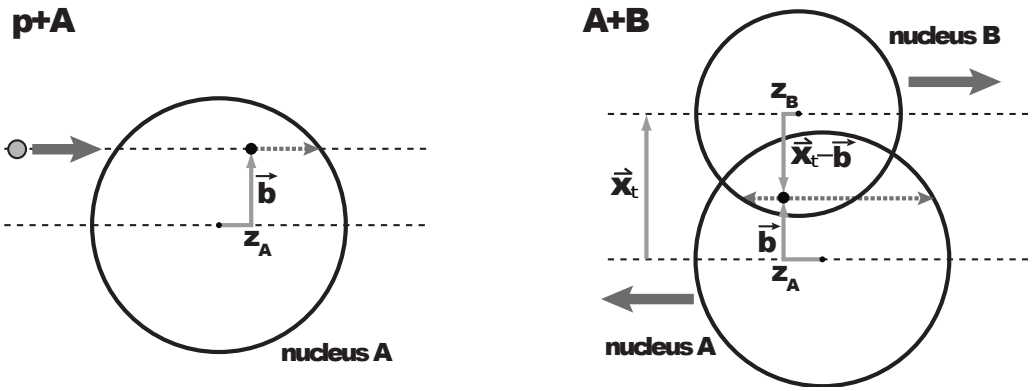

Fig. 38. Schematic representation of the geometry of J/ψ nuclear absorption. The dot represents a (pre)-charmonium. The dashed arrows are their absorption trajectories. Figure taken from Ref. [99].

nucleus A through passing-by nucleons in the same nucleus A is

$$P^{A}_{\rm abs}(\vec{x}_t, z_{\rm A}) = \sigma_{\rm abs}\, T_{\rm A>}(\vec{x}_t, z_{\rm A}) \quad \text{with} \quad T_{\rm A>}(\vec{x}_t, z_{\rm A}) = \int_{z_{\rm A}}^{\infty} \hat{\rho}_{\rm A}(\vec{x}_t, z)\, {\rm d}z \ , \tag{5.14}$$

where $\hat{\rho}$ is normalized to 1, see Eq. (5.6). The effective absorption cross section $\sigma_{\rm abs}$ parameterizes the inelastic scattering between Ψ and nucleons. The integration limits are determined by the absorption trajectories, as illustrated in Fig. 38. Therefore the corresponding survival probability is

$$P^{\rm A}_{\rm surv}(\vec{x}_t, z_{\rm A}) = (1 - \sigma_{\rm abs}\, T_{\rm A>}(\vec{x}_t, z_{\rm A}))^{A-1} \approx \exp\left(-(A-1)\, \sigma_{\rm abs}\, T_{\rm A>}(\vec{x}_t, z_{\rm A})\right) \ , \tag{5.15}$$

where the factor of $(A-1)$ reflects the fact that the $c\bar{c}$ producing nucleon does not participate in the absorption. Similarly the probability for a pre-resonance $c\bar{c}$ state created at $(\vec{x}_t - \vec{b}, z_{\rm B})$ surviving from collisions with nucleons in nucleus B is

$$P^{\rm B}_{\rm surv}(\vec{x}_t - \vec{b}, z_{\rm B}) \approx \exp\Big(-(B-1)\, \sigma_{\rm abs}\, T_{\rm B>}(\vec{x}_t - \vec{b}, z_{\rm B})\Big) \ . \tag{5.16}$$

Therefore the number of surviving charmonia at $\vec{x}_t$ for impact parameter b is

$$\begin{aligned} f_\Psi(\vec{b},\vec{x}_t,\tau_0) =& \Delta y \frac{\mathrm{d}\sigma_{pp}^{\Psi}}{\mathrm{d}y} AB \int\ dz_\mathrm{A}\ dz_\mathrm{B} \hat{\rho}_A(\vec{x}_t,z_\mathrm{A})\ \hat{\rho}_B(\vec{x}_t-\vec{b},z_\mathrm{B}) \\ & \times P^\mathrm{A}_\mathrm{surv}(\vec{x}_t,z_\mathrm{A}) P^\mathrm{B}_\mathrm{surv}(\vec{x}_t-\vec{b},z_\mathrm{B}) \\ =& \Delta y \frac{\mathrm{d}\sigma_{pp}^{\Psi}}{\mathrm{d}y} AB \int\ dz_\mathrm{A}\ dz_\mathrm{B} \hat{\rho}_A(\vec{x}_t,z_\mathrm{A})\ \hat{\rho}_B(\vec{x}_t-\vec{b},z_\mathrm{B}) \\ & \times \exp\left\{-(A-1)\int_{z_\mathrm{A}}^{\infty} dz \hat{\rho}_A(\vec{x}_t,z)\sigma_{abs}\right\} \\ & \times \exp\left\{-(B-1)\int_{z_\mathrm{B}}^{\infty} dz' \hat{\rho}_B(\vec{x}_t-\vec{b},z')\sigma_{abs}\right\}\ , \end{aligned} \tag{5.17}$$

where σ_{pp}^{Ψ} is the charmonium production cross section in elementary nucleon-nucleon collisions. The total number of surviving charmonia is thus

$$N_\Psi(b) = \int f_\Psi(\vec{b},\vec{x}_t,\tau_0)\, d^2\vec{x}_t\ . \tag{5.18}$$

It is convenient to define a nuclear suppression factor,

$$\begin{aligned} S_\mathrm{nuc}(b) = & \frac{1}{T_{AB}(b)} \int d^2\vec{x}_t\, dz_\mathrm{A}\, dz_\mathrm{B}\, \hat{\rho}_A(\vec{x}_t,z_\mathrm{A})\ \hat{\rho}_B(\vec{b}-\vec{x}_t,z_\mathrm{B}) \\ & \times \exp\left\{-(A-1)\int_{z_\mathrm{A}}^{\infty} dz \hat{\rho}_A(\vec{x}_t,z)\sigma_{abs}\right\} \\ & \times \exp\left\{-(B-1)\int_{z_\mathrm{B}}^{\infty} dz' \hat{\rho}_B(\vec{x}_t-\vec{b},z')\sigma_{abs}\right\}\ , \end{aligned} \tag{5.19}$$

which can be used to express the number of surviving charmonia as

$$N_\Psi(b) = \Delta y \frac{\mathrm{d}\sigma_{pp}^{\Psi}}{\mathrm{d}y}\, ABT_{AB}(b) S_\mathrm{nuc}(b)\ . \tag{5.20}$$

Eqs.(5.17), (5.18), (5.19) and (5.20) can be reduced to p+A collisions by setting $\hat{\rho}_B(\vec{x}_t,z)=\delta^{(2)}(\vec{x}_t)\delta(z)$ and B=1. For example, for p+A collisions, Eq. (5.19) reduces

to

$$S_{\rm nuc}(b) = \frac{1}{T_A(b)} \int dz_{\rm A}\ \hat{\rho}_A(\vec{b}, z_{\rm A}) \times \exp\left\{-(A-1)\int_{z_A}^{\infty} dz \hat{\rho}_A(\vec{b}, z)\sigma_{abs}\right\} . \quad (5.21)$$

We parameterize both nuclear shadowing and nuclear absorption with the effective Ψ-N absorption cross section, $\sigma_{\rm abs}$. Applying Eq. (5.21) to p+A collisions at SPS we obtain $\sigma_{\rm abs}^{J/\psi}$=7.3±1 mb from the recent NA60 data at $E_{\rm lab}$=158 GeV (corresponding to $\sqrt{s_{NN}}$=17.3 GeV) [106]. This updated measurement at 158 GeV gives a significantly larger value than previously available for 400 GeV proton projectiles, $\sigma_{\rm abs}$ ≃4.4 mb [107] (the latter has been confirmed by NA60 [106], *i.e.*, at 400 GeV), which has been used in our previous calculations [44, 108]. The comparison with recent PHENIX data [103, 109] yields $\sigma_{\rm abs} \simeq 3.5$ mb (5.5 mb) for $\sqrt{s}$=200 AGeV Au-Au collisions at mid rapidity, $|y| < 0.35$ (forward rapidity, $|y| \in [1.2, 2.2]$), see, *e.g.*, Fig. 39. For simplicity, we assume the same absorption cross sections for the χ_c as for the J/ψ. However, for excited states $\sigma_{\rm abs}$ is expected to be significantly larger, even if they are not fully formed when the dissociation occurs. Taking guidance from the NA50 measurement with 400 GeV protons, we use $\sigma_{\rm abs}^{\psi'} \simeq 13$ mb at $\sqrt{s}$=17.3 AGeV and $\sigma_{\rm abs}^{\psi'} \simeq 6.5(10)$ mb at $\sqrt{s}$=200 AGeV for mid (forward) y.

The rather pronounced rapidity dependence of $\sigma_{\rm abs}$ at RHIC casts doubt on interpreting this quantity as an actual absorption cross section. It seems more reasonable to associate its increase at forward y with nuclear shadowing [110] since the dissociation kinematics is very similar between mid and forward rapidity. While this does not affect the use of our "effective" $\sigma_{\rm abs}$, it does imply a nuclear shadowing effect on the open-charm cross section in A+A collisions (which is an important ingredient in the calculation of regeneration). As a "minimal" scheme we therefore associate the

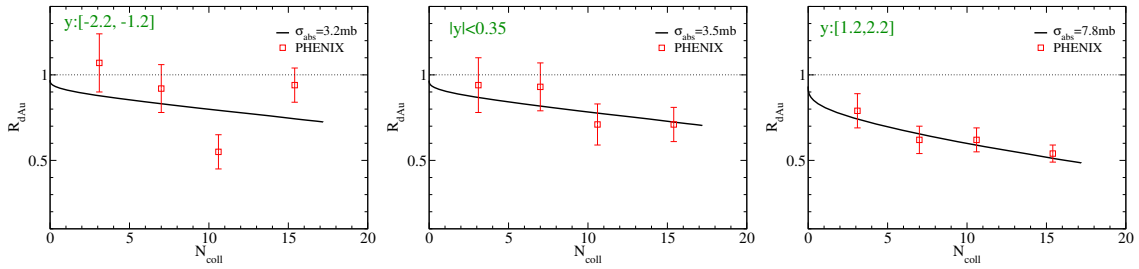

Fig. 39. Centrality dependence of J/ψ R_{dAu} in 200 AGeV d+Au collisions measured by PHENIX [103] together with a Glauber fit with a nuclear absorption cross section σ_{abs}=3.2mb, 3.5mb, and 7.8mb for backward, mid- and forward rapidity.

additional absorption of the J/ψ yield at forward y (relative to mid rapidity) with a suppression of open charm production caused by shadowing, while we assume no shadowing corrections at mid rapidity. Thus, at both SPS and RHIC the number of primordially produced $c\bar{c}$ pairs at mid-rapidity is calculated from the p+p cross section as

$$N_{c\bar{c}}^{\rm mid}(b) = \Delta y \frac{{\rm d}\sigma_{pp}^{c\bar{c}}}{{\rm d}y}\bigg|_{y=0} ABT_{AB}(b) \ , \tag{5.22}$$

while for forward y at RHIC we use

$$N_{c\bar{c}}^{\rm for}(b) = \Delta y \frac{{\rm d}\sigma_{pp}^{c\bar{c}}}{{\rm d}y}\bigg|_{y=1.7} ABT_{AB}(b) \frac{S_{\rm nuc}^{\rm for}}{S_{\rm nuc}^{\rm mid}} \ . \tag{5.23}$$

Here, $T_{AB}(b)$ is the usual nuclear overlap function, Eq. (5.7) and $S_{\rm nuc}$, defined in Eq. (5.19), denotes the J/ψ suppression factor due to CNM effects, parameterized by $\sigma_{\rm abs}$ in the Glauber formula, Eq. (5.17). In particular, the ratio $S_{\rm nuc}^{\rm for}/S_{\rm nuc}^{\rm mid}$ represents the extra suppression associated with nuclear shadowing, operative for both J/ψ and $c\bar{c}$ production.

For the momentum dependent part $f_\Psi(b, \vec{x}_t, \tau_0)$ we take the charmonium p_t spectra in p+p collisions as the baseline and apply a p_t broadening associated with the Cronin effect. The J/ψ p_t spectra in p+p collisions at SPS are parameterized with

an exponential distribution,

$$\frac{d\sigma_{pp}^{J/\psi}}{2\pi p_t dp_t} \propto \frac{1}{\langle p_t^2 \rangle} e^{-p_t^2/\langle p_t^2 \rangle} \ , \tag{5.24}$$

where $\langle p_t^2 \rangle$=1.15GeV^2 [104]. At full RHIC energy the J/ψ p_t spectra are parameterized with a power-law distribution,

$$\frac{d\sigma_{pp}^{J/\psi}}{2\pi p_t dp_t} \propto \frac{C}{[1+(p_t/D)^2]^6} \ , \tag{5.25}$$

where D is adjusted so that $\langle p_t^2 \rangle$=4.14 (3.56)GeV^2 for J/ψ produced at mid (forward) rapidity [95] and C is a normalization factor.

The Cronin effect is readily implemented into the 3-momentum dependent part $f_\Psi(b, \vec{p_t}, \tau_0)$ via a Gaussian smearing of the charmonium p_t distribution in p+p collisions, $f_\Psi^{pp}(p_t)$,

$$f_\Psi(b, \vec{p_t}, \tau_0) = \int \frac{d^2 q_t}{2\pi \langle \Delta p_t^2 \rangle} \exp\left(-\frac{q_t^2}{2\langle \Delta p_t^2 \rangle} \right) \ f_\Psi^{pp}(|\vec{p_t} - \vec{q_t}|) \ . \tag{5.26}$$

The nuclear increase of the average p_t^2, $\langle \Delta p_t^2 \rangle = \langle p_t^2 \rangle_{AA} - \langle p_t^2 \rangle_{pp}$, is estimated within a random-walk treatment of parton-nucleon collisions [111] as being proportional to the mean parton path length, $\langle l^{ab} \rangle$, in the cold medium: $\langle \Delta p_t^2 \rangle = a_{gN} \langle l^{ab} \rangle$. The coefficient a_{gN} is estimated from p+A data at SPS [104] and d-Au data at RHIC [103]. We use a_{gN}=0.076 GeV^2/fm for $\sqrt{s}$=17.3 AGeV Pb-Pb collisions and a_{gN}=0.1(0.2) GeV^2/fm for $\sqrt{s}$=200 AGeV Au-Au collisions at mid (forward) rapidity. The mean parton path length $\langle l^{ab} \rangle$ is determined from the geometric lengths l^a and l^b which two partons a and b travel before they collide, weighted according to the survival probability of final state charmonia [111]

$$l^{ab}(\vec{b}) = \frac{\int \ d^2 x_t \ dz_a \ dz_b \left(l^a(\vec{x}_t, z_a) + l^b(\vec{b} - \vec{x}_t, z_b) \right) K(\vec{b}, \vec{x}_t, z_a, z_b)}{\int d^2 x_t \ dz_a \ dz_b \ K(\vec{b}, \vec{x}_t, z_a, z_b)} \ , \tag{5.27}$$

where

$$l^a(\vec{x}_t, z_a) = A \int_{-\infty}^{z_a} dz \hat{\rho}_A(\vec{x}_t, z)/\rho_0 \ ,$$
$$l^b(\vec{b} - \vec{x}_t, z_b) = B \int_{z_b}^{\infty} dz \hat{\rho}_B(\vec{x}_t - \vec{b}, z)/\rho_0 \ , \tag{5.28}$$

are the respective path lengths travelled by parton a and b weighted according to the nuclear density $\rho(\vec{s}, z)$. The kernel $K(\vec{b}, \vec{x}_t, z_A, z_B)$ is given by

$$\begin{aligned} K(\vec{b}, \vec{x}_t, z_a, z_a) = \rho_A(\vec{x}_t, z_a)\rho_B(\vec{x}_t - \vec{b}, z_b) \\ \times \exp\left(-\sigma_{abs}\left[(A-1)\int_{z_a}^{\infty} dz \hat{\rho}_A(\vec{x}_t, z)\right.\right. \\ \left.\left. +(B-1)\int_{-\infty}^{z_b} dz \hat{\rho}_B(\vec{x}_t - \vec{b}, z)\right]\right) \ , \end{aligned} \tag{5.29}$$

reflecting the survival probability of final state charmonia, recall Eq. (5.17).

CHAPTER VI

APPLICATION TO HEAVY-ION COLLISIONS

In previous chapters we have introduced all the components of the kinetic rate equation/transport approach. In this section we elaborate its application to heavy-ion collisions and compare our numerical results with experimental data.

In Section VI.A we discuss the procedure of applying the kinetic approach to heavy-ion collisions. For the suppression of primordial charmonium (Ψ=J/ψ, χ_c, ψ') we employ the Boltzmann equation to evaluate the time evolution of the Ψ phase space distribution function. To solve the time evolution of regenerated Ψ using the Boltzmann equation requires calculating Ψ regeneration rates from the full time-dependent phase distribution function of charm quarks, which is numerically rather involved and is still a work in progress. For the most parts we adopt a simplified procedure: We estimate the inclusive yield from regeneration with a rate equation and estimate their p_t-spectra with the blastwave formula.

In Section VI.B we present the numerical results of the inclusive J/ψ yield and its transverse momentum (p_t) spectra and compare with SPS and RHIC data. We specifically compare two scenarios with the internal ("strong binding") or free ("weak binding") energy identified as the heavy quark 2-body potential. The effects specifically relevant for high p_t (>5GeV) J/ψ production are discussed. The discussions in Section VI.A and Section VI.B mostly follow Ref. [28].

In Section VI.C we study the impact on charmonium regeneration due to off-equilibrium effects in charm-quark phase space distributions. Specifically, we compare the inclusive yield and p_t spectra of regenerated J/ψ from limiting charm-quark spectra including: (1) thermal charm-quark spectra; (2) pQCD charm spectra. Also, the impact of a charm-quark correlation volume is discussed within the framework of

the Boltzmann equation.

In Section VI.D the production of excited Ψ states such as χ_c and ψ' at SPS and RHIC is briefly discussed.

Finally, in Section VI.E we present predictions for charmonium production at FAIR energies, where the medium is expected to have a lower initial temperature and higher baryon density compared to SPS energies.

A. The Rate Equation Approach

Throughout this chapter we solve kinetic equations (Boltzmann or rate equation) separately for Ψ=J/ψ, χ_c, ψ'. In the hot medium the dissociation and regeneration are the two main processes affecting the Ψ yield. It is often desirable to disentangle these two effects and study their respective strength. For this purpose we decompose the charmonium distribution in the medium at any time τ,

$$f_\Psi(p_t, x_t, \tau) = f_\Psi^{\rm prim}(p_t, x_t, \tau) + f_\Psi^{\rm reg}(p_t, x_t, \tau) \ , \tag{6.1}$$

into a (suppressed) primordial component and a regenerated one by exploiting the linearity of the Boltzmann or rate equation. According to boost-invariance we only need to solve for the time evolution of $f_\Psi(p_t, x_t, \tau)$ in the transverse plane. We define $f_\Psi^{\rm prim}(p_t, x_t, \tau)$ as the solution of the homogeneous Boltzmann equation,

$$\partial f_\Psi^{\rm prim}/\partial\tau + v_t \cdot \nabla_t f_\Psi^{\rm prim} = -\alpha_\Psi f_\Psi^{\rm prim} \ , \tag{6.2}$$

with the same initial condition as for the full Boltzmann equation, (2.1), $f_\Psi^{\rm prim}(p_t, x_t, \tau_0)$ $= f_\Psi(p_t, x_t, \tau_0)$, which is obtained from Eq. (5.13). The explicit expression for the solution of Eq. (6.2) is

$$f_\Psi^{\rm prim}(p_t, x_t, \tau) = f_\Psi(p_t, x_t - v_t(\tau-\tau_0), \tau_0) e^{-\int_{\tau_0}^{\tau} d\tau' \alpha_\Psi(p_t, x_t - v_t(\tau-\tau'), \tau')} \ . \tag{6.3}$$

We account for the "leakage effect", *i.e.*, charmonia escaping the fireball volume no longer being subject to suppression, by setting $\alpha_\Psi \equiv 0$ whenever $|\vec{x}_t - \vec{v}_t(\tau - \tau')| > R(\tau')$, where $R(\tau')$ is the fireball radius at time τ'. Due to the leakage effect the suppression of high p_t charmonia is reduced compared to low p_t ones, since the former are more likely to escape from the fireball.

The regeneration component, $f_\Psi^{\rm reg}$, follows as the difference between the solution of the full and the homogeneous Boltzmann equation, which can be expressed as

$$\partial f_\Psi^{\rm reg}/\partial\tau + v_t \cdot \nabla_t f_\Psi^{\rm reg} = -\alpha_\Psi f_\Psi^{\rm reg} + \beta_\Psi \ , \tag{6.4}$$

with vanishing initial condition, $f_\Psi^{\rm reg}(\vec{x},\vec{p},\tau < \tau_0^\Psi) = 0$. The onset time of regeneration processes, τ_0^Ψ, is defined by the dissociation temperature $T(\tau_0^\Psi) = T_\Psi^{\rm diss}$ for each state Ψ. The explicit expression for the solution of Eq. (6.4) is

$$f_\Psi^{\rm reg}(p_t,x_t,\tau) = \int_{\tau_0^\Psi}^{\tau} d\tau' \beta_\Psi(p_t, x_t - v_t(\tau-\tau'),\tau') e^{-\int_{\tau'}^{\tau} d\tau'' \alpha_\Psi(p_t, x_t - \vec{v}_t(\tau-\tau''),\tau'')} . \tag{6.5}$$

Due to the complication mentioned in the introduction of this chapter we adopt the following approximation: Instead of the Boltzmann transport equation (6.4) we solve the following rate equation for the inclusive yield of the regeneration component,

$$\frac{{\rm d}N_\Psi^{\rm reg}}{{\rm d}\tau} = -\Gamma_\Psi \ (N_\Psi^{\rm reg} - N_\Psi^{\rm eq}) \ . \tag{6.6}$$

For the dissociation rate, Γ_Ψ, we employ a 3-momentum average whose precise value is obtained by matching the final yield of the loss term to the exact result obtained from solving the momentum-dependent Boltzmann equation for the primordial component, Eq. (6.2). For the Ψ equilibrium limit we adopt the statistical model mentioned in Section II.C. Since the thermal production and annihilation rates of $c\bar{c}$ are believed to be small at SPS and RHIC energies, $c\bar{c}$ pairs are assumed to be exclusively produced in primordial N+N collisions and conserved thereafter. The open and hidden charm

states are then populated in relative chemical equilibrium according to the canonical charm-conservation equation, (2.49),

$$N_{c\bar{c}} = Z_1 \frac{I_1(2Z_1)}{I_0(2Z_1)} + N_{\rm hid} \ , \tag{6.7}$$

with $N_{c\bar{c}}$: total number of charm-quark pairs from initial production; $Z_1 = \gamma_c V_{\rm FB} n_{\rm op}$: 1-body open charm partition function (recall Eq. (2.38)), with pertinent equilibrium density $n_{\rm op}$; $N_{\rm hid} = \gamma_c^2 V_{\rm FB} n_{\rm hid}$: total number of all charmonium states with pertinent equilibrium density $n_{\rm hid}$; and γ_c: charm-quark fugacity accounting for the deviation of chemical equilibrium with the heatbath (γ_c=1 in full equilibrium). The ratio of modified Bessel functions, $I_1(2Z_1)/I_0(2Z_1)$, on the right-hand-side of Eq. (6.7) is the characteristic canonical suppression factor which accounts for the exact conservation of net-charm number, $N_c - N_{\bar{c}}$, in each event [112, 47]: for $Z_1 \ll 1$, one has $I_1(2Z_1)/I_0(2Z_1) \to Z_1$, which acts as an additional (small) probability to enforce a vanishing net charm content in the system (*i.e.*, both c and $\bar{c}$ have to be present simultaneously), see Section II.C.1 for a more detailed discussion.

The 1-body open charm partition function, Z_1, is evaluated as follows. For the QGP phase in the weak-binding scenario only charm quarks are counted as open-charm states. In the strong-binding scenario, the T-matrix calculations of Ref. [50] suggest that $c\bar{q}$ and $\bar{c}q$ (charm-light) bound states (D-mesons) survive in QGP up to $\sim$1.3 T_c; therefore, we count both charm quarks and the lowest-lying S-wave D-mesons (D, D^*, D_s and D_s^*), as open charm states for $T < 1.3T_c$. The charm-quark masses in the QGP correspond to the temperature-dependent ones displayed in Fig. 16, while for the meson resonances above T_c we estimate from Ref. [50] $m_D = m_{D^*} \simeq 2.0\,$GeV and $m_{D_s} = m_{D_s^*} \simeq 2.1\,$GeV (hyperfine splitting has been neglected). For the hadronic phase all charmed hadrons listed by the particle data group [113] are counted as open-charm states, with their vacuum masses. The number of hidden charm states, $N_{\rm hid}$,

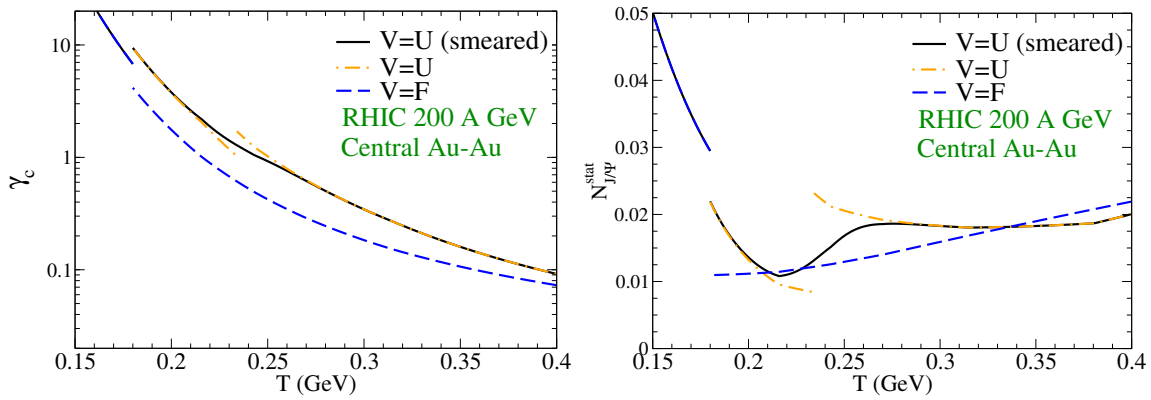

Fig. 40. Temperature dependence of the charm-quark fugacity (left panel) and the in-medium J/ψ equilibrium limit (right panel) using the statistical model in the QGP within the strong-binding scenario (dot-dashed lines: with and without D-meson resonances below and above $1.3\,T_c \simeq 234\,\mathrm{MeV}$, respectively; solid line: smooth interpolation of the previous two cases; see text for details), the weak-binding scenario (dashed line) and in the hadronic phase for temperatures below $T_c = 180\,\mathrm{MeV}$.

is evaluated in line with the existing charmonium states and their masses at given temperature T, but its contribution to $N_{c\bar{c}}$ is numerically negligible.

Knowing $n_{\rm op}$, $n_{\rm hid}$ and $V_{\rm FB}$ at each temperature, one can solve Eq. (6.7) for the charm-quark fugacity, $\gamma_c(T)$, and apply it to compute the statistical equilibrium limit of each charmonium state as

$$N_\Psi^{\rm stat} = \gamma_c^2 \; V_{\rm FB} \; n_\Psi \;, \tag{6.8}$$

in terms of its equilibrium density, n_Ψ. In Fig. 40 we collect the numerical results of the charm-quark fugacity $\gamma_c(T)$ and the statistical equilibrium limit for J/ψ abundances (excluding feeddown) for central 200 AGeV Au+Au collisions at RHIC. The discontinuity at $1.3\,T_c$ for the strong-binding scenario (dot-dashed line) is due to the inclusion of the D resonances in the QGP medium. We smoothly interpolate around the melting temperature for the D-mesons with a hyperbolic tangent func-

tion (solid line) to represent a more gradual (dis)appearance of the D resonances (we have checked that this procedure has negligible impact on the calculation of observables in Section VI.B).

To achieve a more realistic implementation of the statistical equilibrium limit, we apply two corrections to $N_\Psi^{\rm stat}$ to schematically implement off-equilibrium effects of charm quarks in momentum and coordinate space. The former is aimed at simulating incomplete thermalization of the charm-quark p_t spectra throughout the course of the thermally evolving bulk medium. We have shown in Section III.C that the coalescence rate from non- or partially thermalized c- and $\bar{c}$-quark spectra is smaller than for fully thermalized ones [114, 58], since the former are harder than the latter and thus provide less phase-space overlap for charmonium bound-state formation. We implement this correction by multiplying the charmonium abundances from the statistical model with a schematic relaxation factor [114],

$$N_\Psi^{\rm eq} = \mathcal{R}(\tau)\ N_\Psi^{\rm stat}\ ,\ \mathcal{R}(\tau) = 1 - \exp(-\tau/\tau_c^{\rm eq})\ , \tag{6.9}$$

where $\tau_c^{\rm eq}$ is a parameter which qualitatively represents the thermal relaxation time of charm quarks (it is one of our 2 main adjustable parameters in our phenomenological applications in Section VI.B). A rough estimate of this time scale may be obtained from microscopic calculations of this quantity within the same T-matrix approach as used here for charmonia, where the thermal charm-quark relaxation time turns out to be $\tau_{\rm eq}^c \simeq$3-10 fm/c [115, 50]. Such values allow for a fair description of open heavy-flavor suppression and elliptic flow at RHIC [115, 116]. The second correction is applied in coordinate space, based on the realization that, after their pointlike production in hard N+N collisions, the c and $\bar{c}$ quarks only have a limited time to diffuse throughout the fireball volume. At RHIC and especially at SPS only few $c\bar{c}$ pairs are produced (*e.g.*, ${\rm d}N_{c\bar{c}}/dy \simeq 1.2$ in semicentral (b=7 fm) Au+Au collisions

at RHIC), and the hadronization time (QGP lifetime) is smaller than the fireball radius. Thus, c and $\bar{c}$ will not be able to explore the full fireball volume but rather be restricted to a "correlation volume", $V_{\rm co}$ [44] (the analogous concept has been successfully applied to strangeness production in p+A and A+A collisions in the SPS energy regime [117]), see Section II.C.2 for a more detailed discussion. In the present rate equation approach we implement this correction by replacing the fireball volume $V_{\rm FB}$ in the argument of the Bessel functions in Eq. (6.7) by the correlation volume $V_{\rm co}$ [44, 118]. The latter is identified with the volume spanned by a receding $c\bar{c}$ pair,

$$V_{\rm co}(\tau) = \frac{4\pi}{3}(r_0 + \langle v_c \rangle \tau)^3 \ , \tag{6.10}$$

where $r_0 \simeq 1.2\,$fm represents an initial radius characterizing the range of strong interactions, and $\langle v_c \rangle$ is an average speed with which the produced c and $\bar{c}$ quark recede from the production point; we estimate it from the average p_t in D-meson spectra in p+A collisions [119, 44, 55] as $\langle v_c \rangle \simeq 0.55(0.6)c$ at SPS (RHIC). The correlation volume leads to a significant increase of γ_c (since I_0/I_1 is reduced) and thus of the modified Ψ "equilibrium limit" due to locally increased $c\bar{c}$ densities.

The p_t spectra of regenerated charmonia are approximated by local thermal distributions boosted by the transverse flow of the medium, amounting to a standard blastwave description [79], Eq. (4.14),

$$\frac{{\rm d}N_\Psi^{\rm reg}}{p_t {\rm d}p_t} \propto m_t \int_0^R r dr K_1\left(\frac{m_t \cosh\rho}{T}\right) I_0\left(\frac{p_t \sinh\rho}{T}\right) \tag{6.11}$$

($m_t = \sqrt{m_\Psi^2 + p_t^2}$). The medium is characterized by the transverse-flow rapidity $\rho = \tanh^{-1} v_\perp^{cell}(r)$ using a linear flow profile $v_t(r) = v_s \frac{r}{R}$ with a surface velocity $v_s = a_\perp \tau_{\rm mix}$ and transverse fireball radius $R = R(\tau_{\rm mix})$ as given by the fireball expansion formula, Eq. (4.1), at the end of the mixed phase, $\tau_{\rm mix}$. We evaluate the blastwave expression at the hadronization transition (T_c) and neglect rescattering of Ψ's in the

hadronic phase. Two additional effects are neglected in this treatment, which, to a certain extent, tend to compensate each other: on the one hand, due to incomplete charm-quark thermalization, one expects the regenerated charmonium spectra to be harder than in equilibrium, but, on the other hand, a good part of the regeneration occurs before the mixed phase [120, 40] (as will be shown in Section VI.B.1) so that the evaluation of the blastwave expression at the end of the mixed phase presumably overestimates the blue shift due to the flow field. We will explicitly check these effects in Section VI.C. Ultimately, an explicit evaluation of the gain term with realistic (time-dependent) charm-quark spectra within a Boltzmann equation [121] will be able to lift these approximations.

B. Inclusive J/ψ Yield and p_t Spectra at SPS and RHIC

In this section we present and discuss the numerical applications of the above framework to J/ψ data in URHICs at SPS and RHIC. For each observable, we confront the results of the strong- and weak-binding scenario in an attempt to discriminate qualitative features. The feeddown to J/ψ from χ_c and ψ' states is taken into account, assuming fractions of 32% and 8%, respectively, for primordial production in pp collisions. We have divided the discussion into the centrality dependence of inclusive J/ψ yields in Section VI.B.1 and the p_t dependence of J/ψ in Section VI.B.2.

1. Inclusive J/ψ Yield

The J/ψ yield in A+A collisions is usually quantified in terms of the nuclear modification factor as a function of centrality,

$$R_{AA}(b) = \frac{N_{J/\psi}^{AA}(b)}{N_{J/\psi}^{pp} N_{\rm coll}(b)} \ , \tag{6.12}$$

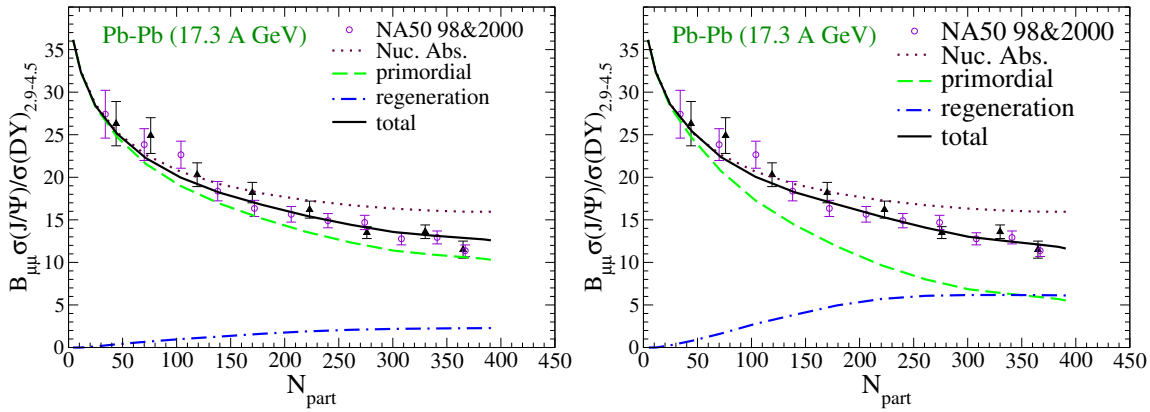

Fig. 41. J/ψ production (normalized to Drell-Yan pairs) versus centrality at SPS evaluated with the thermal rate-equation approach, compared to NA50 data [122, 123]. Solid lines: total J/ψ yield; dashed lines: suppressed primordial production; dot-dashed lines: regeneration component; dotted lines: primordial production with CNM effects only. Left panel: strong-binding scenario; right panel: weak-binding scenario.

where $N_{\rm coll}(b)$ is the number of binary collisions of the incoming nucleons at impact parameter b, recall Eq. (5.8). Before we turn to the results, we recall the two main parameters in our approach, which are the strong coupling constant, α_s, and the thermal charm-quark relaxation time, $\tau_c^{\rm eq}$. The former controls the inelastic charmonium reaction rate, (Eqs. (3.10) and (3.15)), and the latter the magnitude of the Ψ equilibrium limits, Eq. (6.9). We adjust them to reproduce the inclusive J/ψ yield for central A+A collisions at SPS and RHIC, within reasonable bounds. For α_s we find that a common value of 0.32, which is at the upper end of the value in the Coulomb term in the $Q\bar{Q}$ free energy, can be used, in combination with $\tau_c^{\rm eq}$=3.8 fm/c for the strong-binding scenario and $\tau_c^{\rm eq}$=1.6 fm/c for the weak-binding scenario. For simplicity, we refrain from introducing an additional temperature dependence into these parameters. The composition of the total yield, its centrality dependence and p_t spectra can then be considered as a prediction within each of the 2 scenarios.

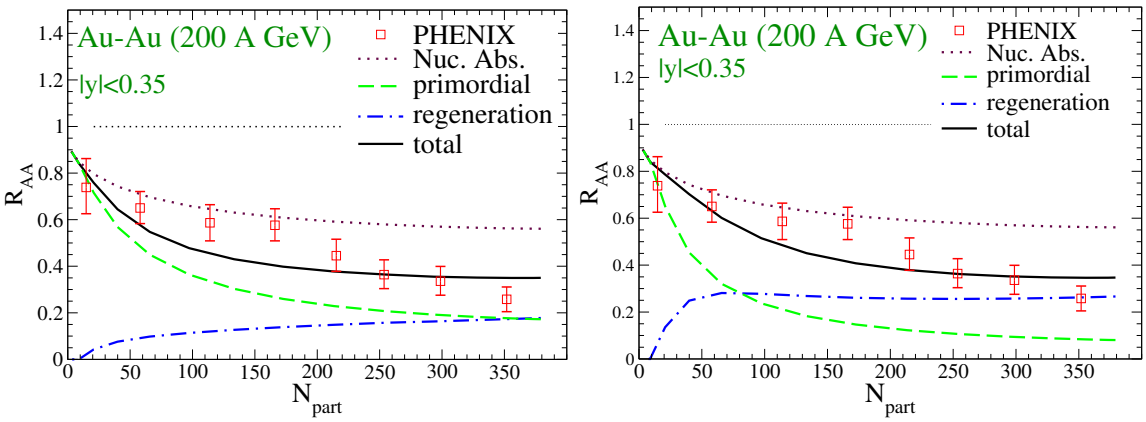

Fig. 42. J/ψ R_{AA} versus centrality at mid-rapidity at RHIC evaluated with the thermal rate-equation approach, compared to PHENIX data [124]. Solid lines: total J/ψ yield; dashed lines: suppressed primordial production; dot-dashed lines: regeneration component; dotted lines: primordial production with CNM effects only. Left panel: strong-binding scenario; right panel: weak-binding scenario.

We begin with J/ψ production in $\sqrt{s}$=17.3 AGeV Pb+Pb collisions at SPS, for which we compare our results in the strong- and weak-binding scenario with NA50 data in Fig. 41. For these data, the denominator in Eq. (6.12) is replaced by the number of Drell-Yan dileptons at high mass, while the numerator includes the branching ratio into dimuons. The pertinent proportionality factor, equivalent to the *pp* limit of this ratio (47.0±1.4 [125]), and the CNM-induced suppression (dotted line in Fig. 41) are inferred from the latest NA60 p+A measurements [106], which we reproduce using the Glauber model formula, Eq. (5.17), with $\sigma_{\rm abs}$=7.3 mb. The suppression of the primordial component (dashed line) relative to nuclear absorption (dotted line) represents the "anomalous" suppression by the hot medium, which increases with centrality due to higher initial temperatures and longer fireball lifetimes. The regeneration component increases with centrality as well, mostly due to the increase of the $\mathcal{R}$-factor and the larger lifetime which facilitates the approach to the equilibrium

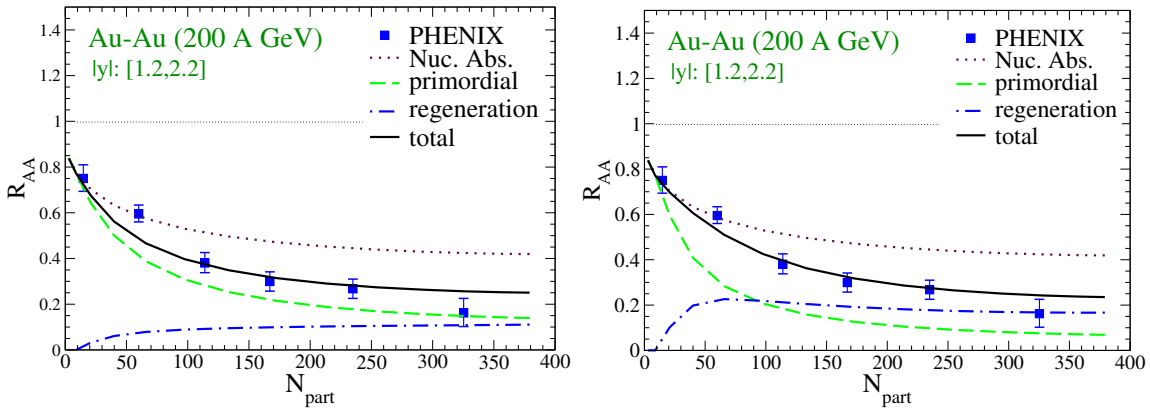

Fig. 43. J/ψ R_{AA} vs. centrality at forward rapidity compared to PHENIX data [124]. Solid lines: total J/ψ yield; dashed lines: suppressed primordial production; dot-dashed lines: regeneration component; dotted lines: primordial production with CNM effects only. Left panel: strong-binding scenario; right panel: weak-binding scenario.

limit according to Eq. (6.6). Because of detailed balance between dissociation and regeneration, an increase in the former also implies an increase in the latter. The sum (solid line) of primordial and regeneration contributions describes the centrality dependence of the inclusive J/ψ yield at SPS reasonably well in both scenarios. In the strong-binding scenario the primordial component is dominant and the majority of the anomalous suppression originates from the dissociation of χ_c and ψ', since at the temperatures realized at SPS ($T_0 \simeq 200\,\mathrm{MeV}$) the quasifree dissociation rates for χ_c and ψ' are much larger than those for J/ψ, recall Fig. 21. In the weak-binding scenario, however, the regeneration yield becomes comparable to the primordial one for semi-/central collisions due to larger dissociation rates and the smaller charm-quark equilibration time scale.

Next we examine the centrality dependence of J/ψ production in 200 AGeV Au+Au collisions at RHIC, first focusing on mid rapidity ($|y| < 0.35$), as shown in Fig. 42. The suppression due to CNM effects (dotted line in Fig. 42) is inferred

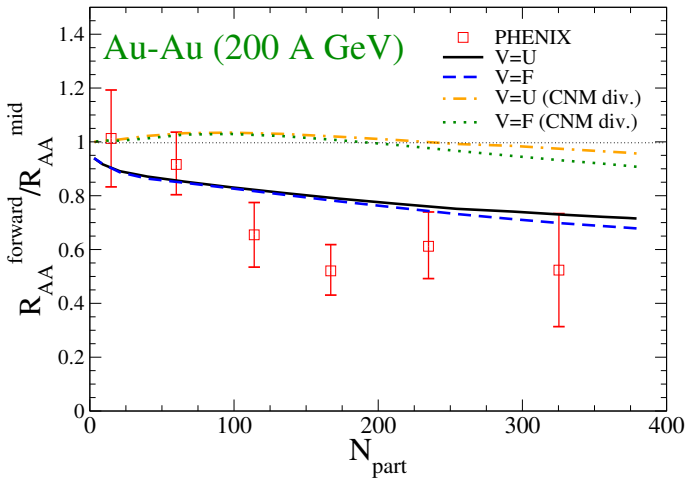

Fig. 44. Ratio of R_{AA} for J/ψ at forward and mid rapidity versus centrality in the strong (solid line) and weak (dashed line) binding scenarios compared to PHENIX data [124]. In the upper two curves, CNM effects have been divided out in both numerator and denominator of the ratio.

from latest PHENIX d+Au measurements, which we reproduce using the Glauber model formula Eq. (5.17) with $\sigma_{\rm abs}$=3.5 mb. For $N_{\rm part} \simeq 0-100$, the composition of primordial and regeneration contributions is quite comparable to the SPS for $N_{\rm part} \simeq 0-400$ within both scenarios. Beyond $N_{\rm part} \simeq 100$, suppression and regeneration continue to increase, leveling off at an approximately 50-50% (20-80%) partition for primordial and regeneration in the strong-binding (weak-binding) scenario in central collisions.

Let us now turn to J/ψ production at forward rapidity ($|y| \in [1.2, 2.2]$) at RHIC, shown in Fig. 43. Again, both strong- and weak-binding scenarios reproduce the experimental data fairly well, with similar relative partitions for primordial and regeneration contributions as at mid rapidity. However, one of the "puzzles" about J/ψ production at RHIC is the fact that the total J/ψ yield is more strongly suppressed at forward rapidity than at mid rapidity. In our approach this follows from the stronger shadowing at forward rapidity leading to less primordial production for

both J/ψ and $c\bar{c}$ pairs. The former (latter) leads to a reduction of the primordial (regeneration) component. Since the thermodynamic properties of the fireball are quite similar at mid and forward rapidity (recall Fig. 29), charmonium suppression and regeneration in the hot medium are very similar between the mid and forward rapidity as discussed in Ref. [76]. To quantify the difference at forward rapidity and mid rapidity we display the ratio between the corresponding R_{AA}'s in Fig. 44 for both scenarios, which clearly illustrates the importance of CNM effects to properly reproduce the data.

In Section III.A we have argued that the strong- and weak-binding scenarios discussed here may be considered as limiting cases for J/ψ binding in the QGP, as bracketed by the identification of the heavy-quark internal and free energies with a Q-$\bar{Q}$ potential. From the results above we believe that these scenarios also provide a reasonably model-independent bracket on the role of suppression and regeneration effects, in the following sense: At SPS, the strong-binding scenario defines a "minimal" amount of dissociation required to provide the anomalous suppression beyond CNM effects (a small regeneration component is inevitable due to detailed balance). The application to RHIC energy then implies an approximately equal partition of primordial and regenerated charmonia in central Au+Au, not unlike Ref. [40] where the vacuum charmonium binding energies ("strong binding") have been used in the QGP (together with the gluo-dissociation). On the other hand, in the weak-binding scenario, a large part of the J/ψ yield in central A+A is due to regeneration even at SPS, limited by the constraint that for sufficiently peripheral collisions (and at sufficiently large p_t) a transition to primordial production compatible with p+A data should be restored. Clearly, for central A+A at RHIC (and certainly at LHC) the final yield is then dominated by regeneration. Since both scenarios describe the inclusive yields reasonably well, it is mandatory to investigate more differential observables to

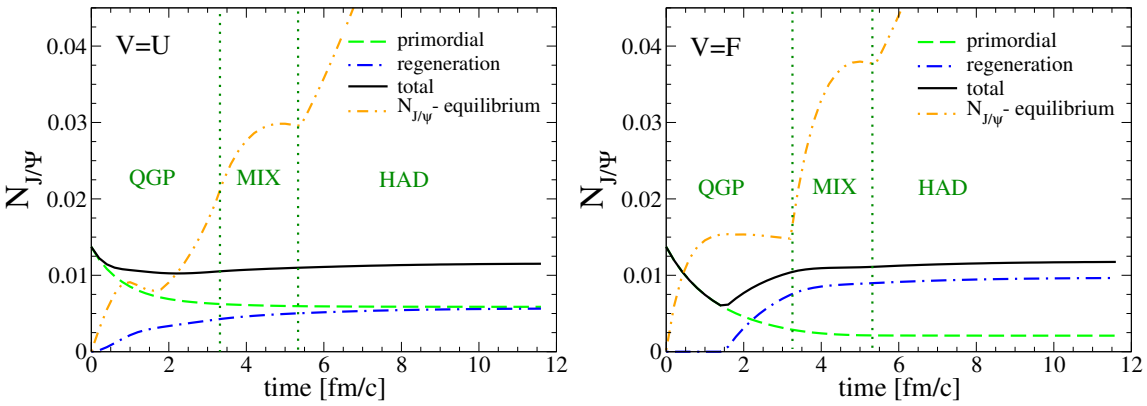

Fig. 45. J/ψ abundance as a function of time in central ($N_{\rm part}$=380) Au+Au collisions at RHIC. Solid lines: total; dashed line: primordial component; dot–dashed line: regeneration component; double dot-dashed line: equilibrium limit, $N^{\rm eq}_{J/\psi}$. Left panel: strong-binding scenario; right panel: weak-binding scenario.

find discriminating evidence. This will be pursued in the following section.

It is instructive to examine the time evolution of J/ψ production in the two scenarios, displayed in Fig. 45 for central collisions at mid rapidity at RHIC (excluding feeddown from χ_c and ψ'). In both scenarios most of the dissociation and regeneration indeed occur in the QGP and mixed phase, since the hadronic reaction rates are small. In the weak-binding scenario the time-dependent J/ψ yield exhibits a "dip" structure around $\tau \simeq 1.5\,{\rm fm}/c$ because the large dissociation rates suppress primordial J/ψ very rapidly and regeneration only starts after the medium temperature falls below the J/ψ dissociation temperature ($T^{\rm diss}_{J/\psi} \simeq 1.25\,T_c$). This scenario is closest in spirit to the statistical hadronization model [36] where all initial charmonia are suppressed (or never form to begin with, except for corona effects) and are then produced at the hadronization transition.

2. J/ψ Transverse Momentum Spectra

a. Average Transverse Momentum

The results of the previous section suggest that, within the current theoretical (*e.g.*, charm-quark relaxation time, $\tau_c^{\rm eq}$) and experimental uncertainties both of the "limiting" scenarios can reproduce the centrality dependence of the inclusive $R_{AA}^{J/\psi}(N_{\rm part})$ reasonably well at both SPS and RHIC energies. However, the composition between suppression and regeneration yields is rather different which ought to provide a key to distinguish the two scenarios. The obvious "lever arm" are charmonium p_t spectra [37]. One expects that the primordial component is characterized by harder p_t spectra (following a power law at high p_t) while the regeneration component produces softer p_t spectra characterized by phase-space overlap of (partially) thermalized charm-quark spectra. However, in practice, the transition from the "soft" recombination regime to the "hard" primordial regime is quite uncertain; *e.g.*, collective flow and incomplete thermalization of c-quarks can lead to a significant hardening of the regenerated J/ψ spectra, while a dissociation rate which increases with 3-momentum [108] can induce a softening of the spectra of surviving primordial charmonia.

For a more concise discussion of the p_t dependence of J/ψ as a function of centrality at SPS and RHIC we here focus on the average p_t^2, as compiled in Figs. 46 and 47. At the SPS (Fig. 46), the centrality dependence of $\langle p_t^2\rangle$ is largely dictated by the the Cronin effect in the primordial component, especially in the strong-binding scenario where this contribution dominates the yield at all centralities. The momentum dependence of the dissociation rate induces a slight suppression of $\langle p_t^2\rangle$ at large centrality compared to the case where only CNM effects are included (dashed vs. dotted line) [108]. In the weak-binding scenario, larger contributions from regeneration induce a slight "dip" structure at intermediate centralities due to a rather small

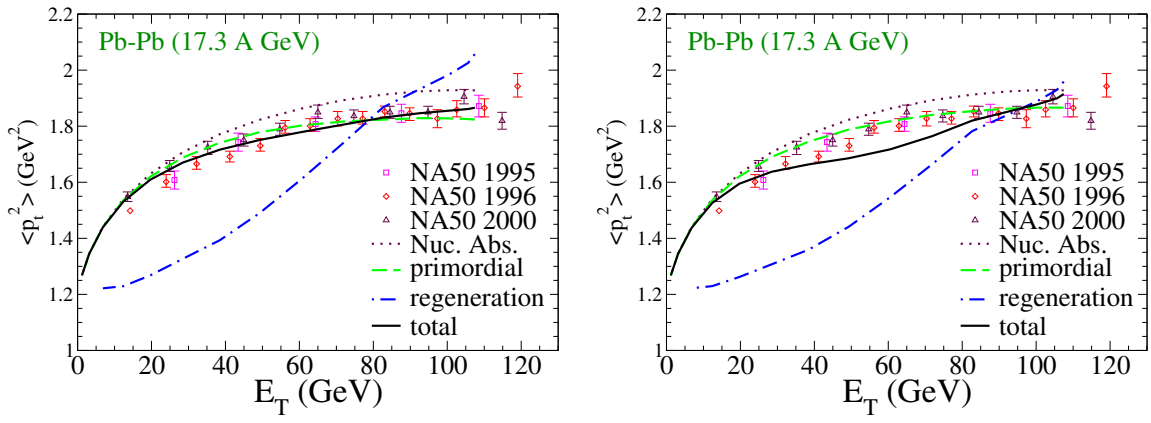

Fig. 46. $\langle p_t^2 \rangle$ of J/ψ vs. centrality at SPS, compared to NA50 data [126, 104]. In each panel, $\langle p_t^2 \rangle$ is plotted for total J/ψ yield (primordial + regeneration component; solid lines), the suppressed primordial component (dashed line), the regeneration component (dash-dotted line) and primordial production with CNM effects only (dotted lines). The left (right) panels correspond to the strong-binding (weak-binding) scenario. The transverse energy, E_T, is a measure of centrality. Its value in GeV is about $0.275 \times N_{part}$.

collective flow at the end of the (relatively short) mixed phase in these collisions. At RHIC energy (Fig. 47), the individual primordial and regeneration components show qualitatively similar behavior for $\langle p_t^2 \rangle (N_{\rm part})$ as at SPS, *i.e.*, an increase due to Cronin effect and collective flow, respectively. At mid rapidity, the general trend is that with increasing centrality the growing regeneration contribution pulls down the average $\langle p_t^2 \rangle$, in qualitative agreement with the data. The curvature of the $\langle p_t^2 \rangle (N_{\rm part})$ dependence, which appears to be negative in the data, is not well reproduced, neither by the strong- nor by the weak-binding scenario, even though the deviations are smaller in the former. A more microscopic calculation of the gain term, together with more accurate estimates of the Cronin effect, are warranted to enable more definite conclusions. For both rapidity regions, the $\langle p_t^2 \rangle$ of the suppressed primordial component is slightly larger in the weak- than in the strong-binding scenario. This is caused by the stronger 3-momentum increase of the dissociation rate in the strong-binding

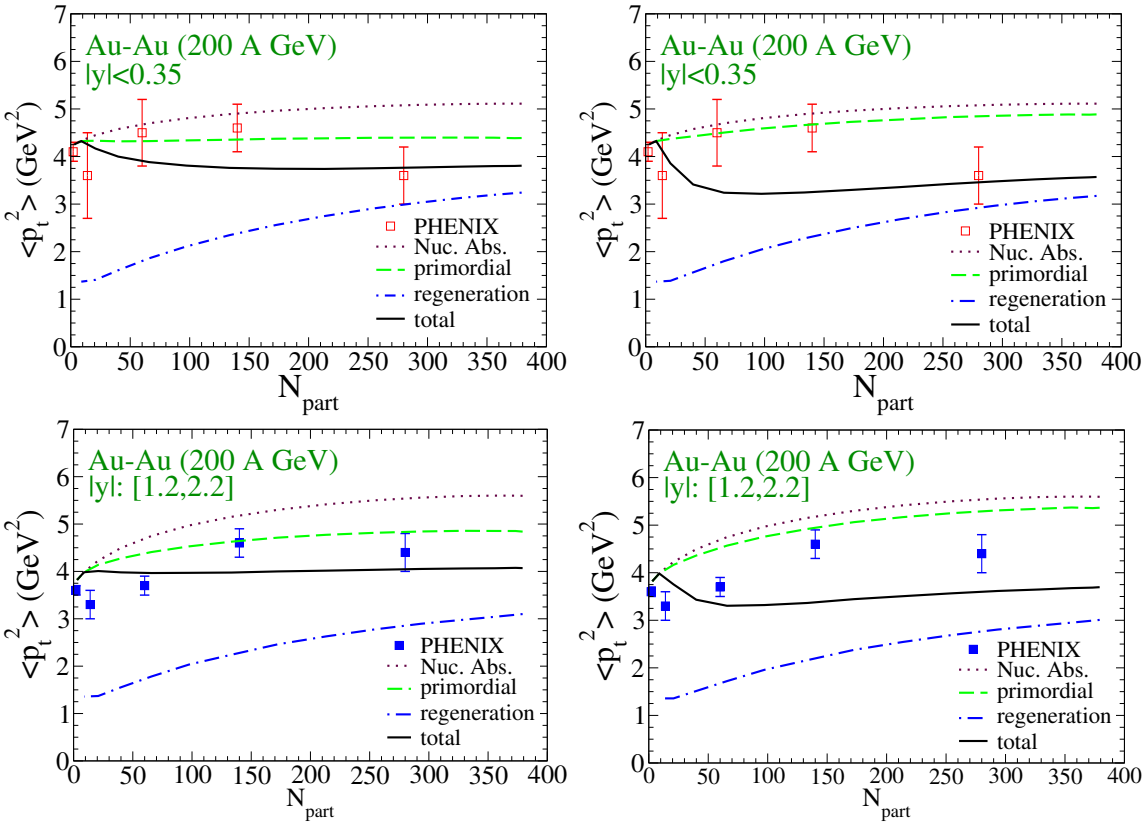

Fig. 47. $\langle p_t^2 \rangle$ of J/ψ vs. centrality at RHIC at mid-rapidity (upper panels) and forward rapidity (lower panels), compared to PHENIX data [124]. In each panel, $\langle p_t^2 \rangle$ is plotted for total J/ψ yield (primordial + regeneration component; solid lines), the suppressed primordial component (dashed line), the regeneration component (dash-dotted line) and primordial production with CNM effects only (dotted lines). The left (right) panels correspond to the strong-binding (weak-binding) scenario.

scenario, recall the right panel of Fig. 21.

The overall comparison to SPS and RHIC data for the p_t dependence of J/ψ's seems to indicate a slight preference for the strong-binding scenario. This is mostly derived from the observation that for peripheral collisions the experimentally observed $\langle p_t^2 \rangle$ essentially follows the extrapolation of the Cronin effect, suggesting J/ψ production of predominantly primordial origin (the collective flow imparted on the regeneration component appears to be too small at these centralities, rendering the weak-binding scenario problematic).

b. High p_t J/ψ Production and Elliptic Flow

The average p_t^2 essentially characterizes the momentum dependence of charmonium production at low and moderate p_t where most of the yield is concentrated. Recent RHIC data [92, 93] have triggered considerable interest in J/ψ production at high $p_t \simeq 5 - 10\,\mathrm{GeV}$ which is expected to provide complementary information. It was found that the suppression in $R_{AA}^{J/\psi}(p_t \gtrsim 5\,\mathrm{GeV})$ in Cu-Cu collisions is reduced compared to the low-p_t region, with R_{AA}-values of ∼0.7-1 or even larger [93]. This is quite surprising in light of the light-hadron spectra measured thus far at RHIC which all exhibit stronger suppression of $R_{AA} \simeq 0.25$ for $p_t \gtrsim 6\,\mathrm{GeV}$ (even electron spectra from open heavy flavor, *i.e.*, charm and bottom decays). It also appears to be at variance with the thermal J/ψ dissociation rates which, if anything, increase with momentum (recall Fig. 21) and thus imply a stronger suppression at higher p_t. Furthermore, the leakage effect mentioned in Section VI.A is not strong enough to produce the experimentally observed increase in $R_{AA}^{J/\psi}(p_T \gtrsim 5\,\mathrm{GeV})$ [108].

Therefore we consider the following two effects primarily relevant at high p_t [127]: (1) Finite formation times for the charmonium states [128, 129, 130] and (2) Bottom feeddown. Concerning (1), one expects reduced geometrical sizes for a "pre-

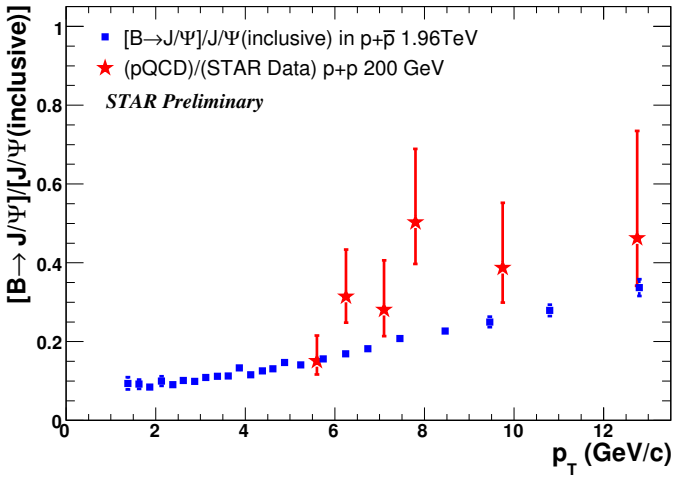

Fig. 48. Ratio of J/ψ from B-meson feeddown to inclusive J/ψ indicated by Tevatron [131] and STAR data [132].

resonance" $c\bar{c}$ pair relative to a fully formed charmonium due to a finite formation time, τ_f, required to build up the hadronic wave function. If the "pre-resonance" $c\bar{c}$ pair is in a color-singlet state, as suggested by the color singlet model (CSM) (recall Section V.A), its smaller geometrical size will translate into a smaller dissociation cross section, since it appears color-neutral for incoming partons whose momenta are not large enough to resolve its inner structure. For a schematic estimate we parameterize the evolution of the pre-hadronic dissociation rate as

$$\Gamma_{pre-\Psi}(\tau) = \Gamma_\Psi \tau/\tau_f^{lab} \quad , \quad \tau \leq \tau_f^{lab} = \tau_f m_t/m_\Psi \tag{6.13}$$

with Γ_Ψ: (nuclear, partonic or hadronic) dissociation rates for a formed charmonium, τ: fireball proper time, τ_f=0.89(2.01,1.50) fm/c: formation time of $J/\psi(\chi_c, \psi')$ in its rest frame, and $m_t = (m_\Psi^2 + p_t^2)^{1/2}$. Essentially, (pre-) charmonium dissociation rates acquire an additional momentum dependence through Lorentz time dilation, being reduced at high p_t. Also note that the longer formation times of χ_c and ψ' imply less suppression relative to J/ψ, quite contrary to standard dissociation and regeneration

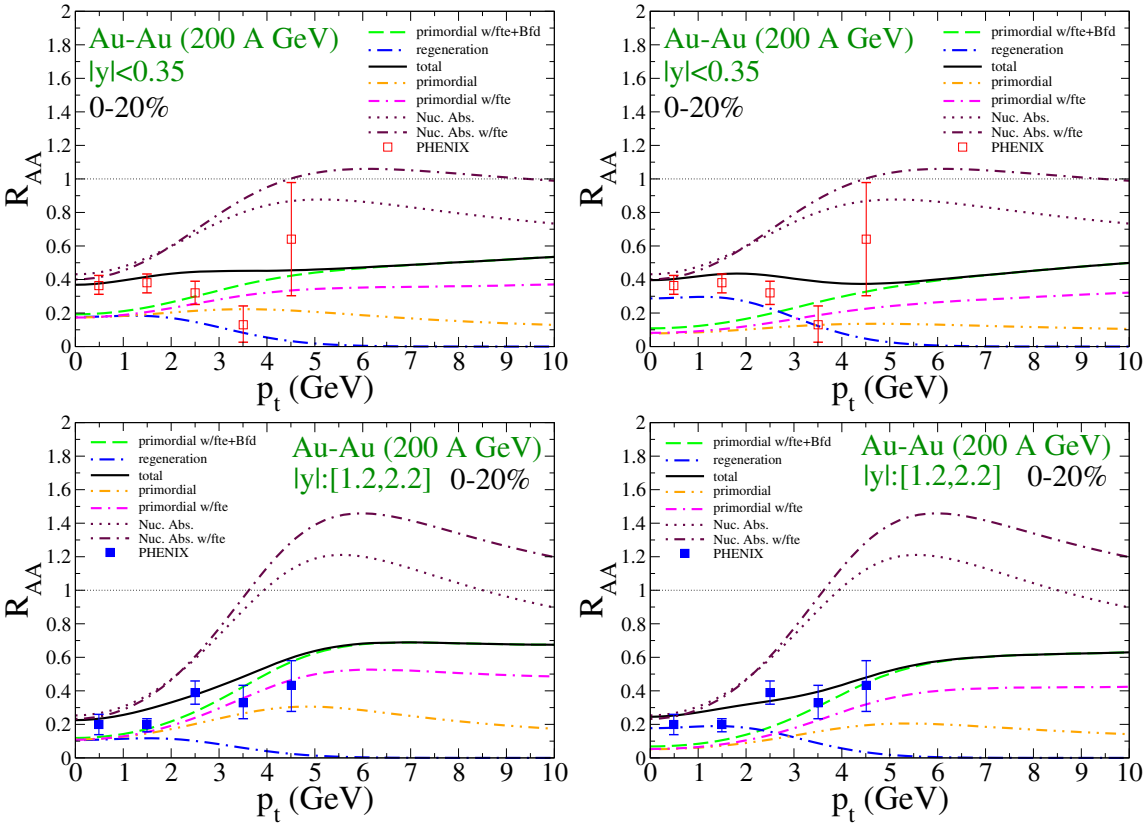

Fig. 49. J/ψ R_{AA} versus p_t in central 200 AGeV Au+Au collisions including formation-time effects (fte) and B-meson feeddown (Bfd) contributions. PHENIX data [124] are compared to our rate-equation calculations in the strong- and weak-binding scenarios (left and right panels, respectively). Upper panels: mid-rapidity; lower panels: forward rapidity.

mechanisms: as higher excited $c\bar{c}$ states than J/ψ they have smaller binding energy and therefore are more easily destroyed, and they are heavier so that their equilibrium abundances are suppressed compared to J/ψ by the thermal Boltzmann factor leading to a reduced regeneration. Therefore high-p_t χ_c and ψ' could provide a rather unique signature of the formation time effect. Concerning (2), Fig. 48 shows recent data on the $B \to J/\psi$ feeddown fraction in elementary p+p($\bar{\text{p}}$) collisions, which is quite significant. As an estimate of this contribution, we use the Tevatron data [131] and replace the corresponding fraction of primordial component.

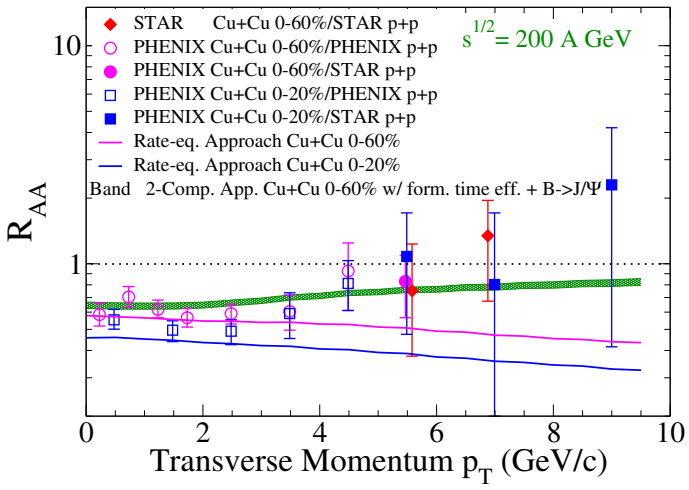

Fig. 50. J/ψ R_{AA} vs. p_t in 0-60% Cu+Cu collisions, compared RHIC data [92, 133]. The formation time effects and B-meson feeddown (green band) are included. The partition between the primordial and regeneration components is based on the thermal rate-equation approach in Ref. [108].

Combining formation time effects and B-meson feeddown we obtain results for $R_{AA}^{J/\psi}(p_t)$, as displayed in Fig. 49 up to $p_t = 10\,\mathrm{GeV}$. We find that the suppression is reduced to about 0.5 at the highest p_t, compared to about 0.4 at low p_t. This is similar to the moderate enhancement we found in the Cu-Cu case [127], as shown in Fig. 50. Surprisingly, the high-p_t suppression turns out to be very similar in both strong- and weak-binding scenarios, despite the fact that the high-p_t yield is exclusively due to the primordial component whose strength is very different in the 2 scenarios at low p_t. The reason is the 3-momentum dependence of the dissociation rates, which become quite similar in the 2 scenarios at large 3-momentum: at $p \simeq 10$ GeV, the difference in the energy-threshold due to binding energies of several 100 MeV becomes less relevant so that a collision with almost any thermal parton is energetic enough for dissociating the bound state. For J/ψ at forward rapidity (shown in lower panels of Fig. 49), we additionally include the effect that the nuclear shadowing (responsible for the extra CNM-induced suppression relative to mid-rapidity) decreases with the

p_t of the primordially produced J/ψ. We assume that it ceases to exist at around p_t=10 GeV, recall the discussion in Section V.B.2.a.

Let us also estimate the elliptic flow, $v_2(p_t)$, of the J/ψ, (recall Eq. (1.12)), which is hoped to be another good discriminator of primordial and regenerated production. For the former, a nonzero v_2 is basically due to the path-length difference when traversing the azimuthally asymmetric fireball, typically not exceeding 2-3% [40, 134]. For the latter, much larger values can be obtained if the coalescing charm quarks are close to thermalized [135, 58]. However, as pointed out in Ref. [127], the well-known mass effect suppresses the $v_2(p_t)$ for heavy particles at $p_t \lesssim m$; it is precisely in this momentum regime where the regeneration component is prominent. In Ref. [127] we estimate the total J/ψ $v_2(p_t)$ by combining the v_2 from the primordial production computed in Refs. [40, 134] and that from the regeneration computed in Refs. [135, 58] with relative fractions determined from our thermal rate-equation approach. In Fig. 51 we show the resulting total J/ψ $v_2(p_t)$ for 20-40% central Au+Au collisions, where neither the formation time effect nor B-meson feeddown is included. These two effects would further increase the fraction of the primordial components in the intermediate to high p_t region leading to an even smaller total v_2 in this region. Thus, we predict that in both strong- and weak-binding scenarios the total J/ψ $v_2(p_t)$ does not exceed $\sim$5% at any p_t, similar to what is found in Refs. [40, 136]. The only alternative option we can envision are strong elastic interactions of the J/ψ which are only conceivable in the strong binding scenario to avoid break-up in scattering off thermal partons [55].

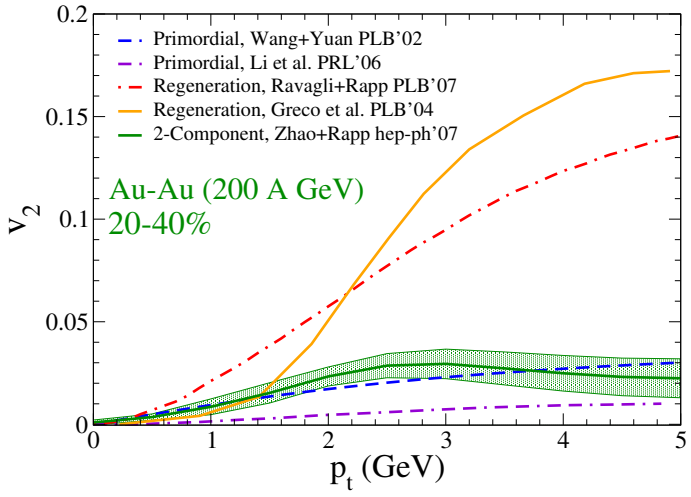

Fig. 51. J/ψ $v_2(p_t)$ for 20-40% central Au+Au collisions at RHIC. Figure taken from Ref. [127]. The band represents the sum of uncertainties based on differences between two independent "input" $v_2(p_t)$ calculations for each of the two components.

C. Explicit Calculations of the Regeneration Component

In this section we explicitly calculate J/ψ regeneration from input charm-quark spectra using the Boltzmann equation (6.4) instead of the rate equation (6.6) to check the sensitivity of Ψ regeneration to off-equilibrium effects in charm-quark spectra.

1. Sensitivity of J/ψ Regeneration to Charm-Quark p_t Spectra

We first compare the inclusive yield of J/ψ's regenerated from the three types of charm-quark momentum spectra introduced in Section III.C: 1) thermal charm-quark spectra; 2) 3-dimensionally isotropic pQCD spectra; 3) transversely pQCD + longitudinally thermal spectra. Our calculation is performed at RHIC energy where the regeneration component takes up a significant fraction. For comparison purpose we only consider J/ψ regeneration in QGP phase with the quasifree process $i + c + \bar{c} \to i + J/\psi$ $(i = g, q, \bar{q})$ within the strong binding scenario. Neither the

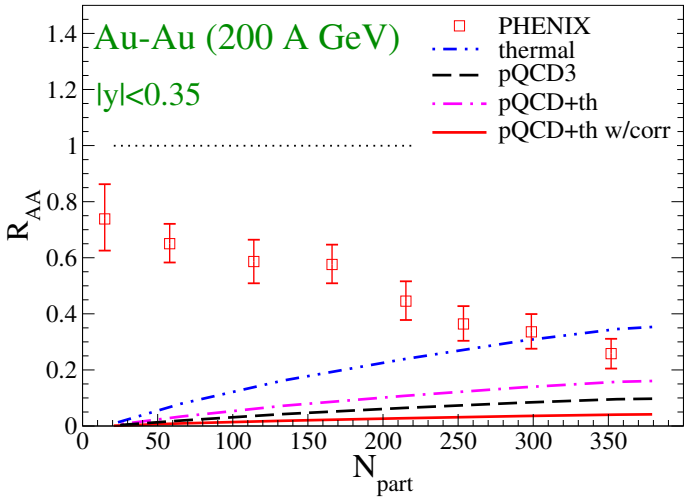

Fig. 52. J/ψ regeneration from different charm-quark spectra. Double-dot-dashed line: thermal charm-quark spectra. Dashed line: 3-dimensionally isotropic pQCD charm-quark spectra. Dot-dashed line: pQCD charm-quark spectra in transverse plane + thermal spectra in longitudinal direction. Solid line: pQCD charm-quark spectra in transverse plane with angular correlation between c and $\bar{c}$ + thermal spectra in longitudinal direction.

canonical ensemble effect nor the correlation volume effect (see Section II.C) are applied; these two effects will be discussed in the next section. The resulting centrality dependence of inclusive yields of regenerated J/ψ is compared in Fig. 52. Clearly, the thermal charm-quark spectra are most efficient in regenerating J/ψ due to the large phase space overlap between c, $\bar{c}$ quarks and light partons in the medium. The regeneration from longitudinally thermal and transversely pQCD spectra is reduced to about half relative to the thermal spectra. The regeneration from 3-dimensionally isotropic pQCD charm-quark spectra is even reduced by a factor of 4. This result is similar to what is found in a quark coalescence model [58] where the number of J/ψ coalesced from pQCD charm-quark spectra is smaller than that from thermal spectra by a factor of 3. However in Ref. [40] a similar Boltzmann transport approach was employed for J/Ψ regeneration with the (inverse) gluo-dissociation process as the re-

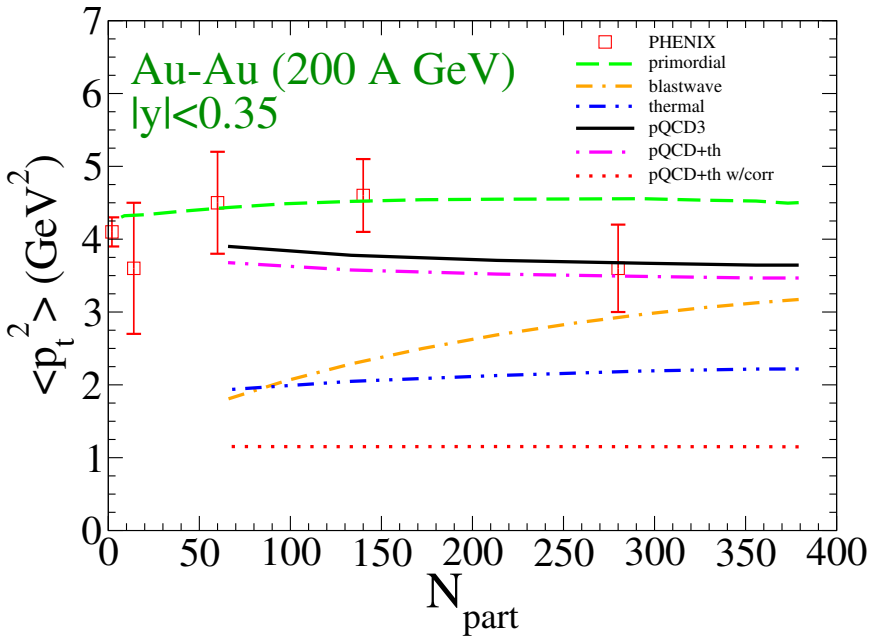

Fig. 53. $\langle p_t^2 \rangle$ of J/ψ's regenerated from different charm-quark spectra. Double-dot–dashed line: thermal charm-quark spectra; solid line: 3-dimensional isotropic pQCD charm-quark spectra; dot-dashed line: longitudinal thermal + transverse pQCD charm-quark spectra; dotted line: longitudinal thermal + transverse pQCD charm-quark spectra with angular correlation between c and $\bar{c}$; double dash-dotted line: the $\langle p_t^2 \rangle$ from the rate equation + blastwave treatment; dashed line: the $\langle p_t^2 \rangle$ of the primordial component.

generation mechanism and it is found that the inclusive yield of regenerated J/ψ from pQCD charm spectra is quite comparable with that from thermal spectra (within a $\sim$30% difference). Further investigations are needed to clarify the discrepancy. We also find that if the angular correlation between the transverse momentum of c and $\bar{c}$ is included, to reflect the back-to-back charm production in initial hard collisions, the regeneration is further reduced to about 1/10 of the regeneration from fully thermalized charm-quark spectra, as a result of further reduction of the $c\bar{c}$ overlap in momentum space.

Next we proceed to the $\langle p_t^2 \rangle$ of regenerated J/ψ, displayed in Fig. 53. As ex-

pected, the $\langle p_t^2 \rangle$ of J/ψ regenerated from pQCD charm-quark spectra is larger than that from thermal spectra. We note that the $\langle p_t^2 \rangle$ from thermal charm-quark spectra is lower than that estimated from the blastwave formula. This is due to the fact that in the strong-binding scenario most of the regeneration processes occur at an early stage of the medium evolution (see Fig. 45), when the collective flow has not yet fully built up. Here the (transverse) medium flow effect is included only for the thermal charm-quark spectra, for the other two types of pQCD spectra we assume the medium is at rest in the lab frame. We also note that the introduction of the angular correlation between c and $\bar{c}$ momenta significantly lowers the $\langle p_t^2 \rangle$ of regenerated J/ψ. This is because high p_t J/ψ's are more likely to be regenerated from two charm quarks with a small angle between them, the probability of which is significantly suppressed by the back-to-back correlation of charm pairs. Therefore the regeneration of J/ψ's at high p_t is more reduced than at low p_t leading to a reduction of $\langle p_t^2 \rangle$.

2. Sensitivity of J/ψ Regeneration to Charm-Quark Correlation Volume

In this section we explicitly evaluate J/ψ regeneration from individual events with integer numbers of $c\bar{c}$ pairs produced, recall Fig. 15. The correlation volume effect (see Section II.C.2) is applied separately to events with integer (k) charm quark pairs. At the end we average the regenerated J/ψ over these events. The time dependence of the correlation volume $V_{co}(\tau)$ is modelled using Eq. (6.10). A rather simplified prescription is adopted to treat the merging of correlation volumes: If at any given moment τ the total correlation volume (sum over all "bubbles") $kV_{co}(\tau)$ is larger than $V_{FB}(\tau)$, $kV_{co}(\tau)$ is set to $V_{FB}(\tau)$ for the subsequent evolution. In order to check the sensitivity of J/ψ regeneration to different sizes of the correlation volume, we multiply $V_{co}(\tau)$ from Eq. (6.10) with different overall scaling factors and compare the resulting inclusive yield. The results are presented in Fig. 54. First we see

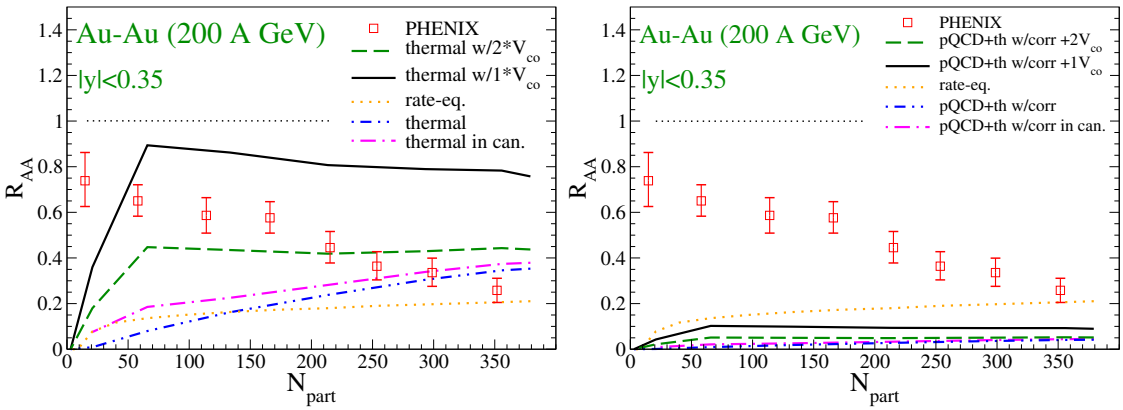

Fig. 54. J/ψ regeneration with different charm-quark correlation volumes. Left panel: thermal charm-quark spectra; right panel: longitudinal thermal + transverse pQCD charm-quark spectra with angular correlation between c and $\bar{c}$. Double-dot-dashed line: regeneration in grand-canonical ensemble; dot-dashed line: regeneration in canonical ensemble, but without correlation volume effect; solid line: regeneration with $1\times V_{co}$; dashed line: regeneration with $2\times V_{co}$; dotted line: regeneration from the thermal rate equation approach.

that the charmonium regeneration is stronger in the canonical ensemble than in the grand-canonical ensemble. Including the correlation volume effect further enhances the regeneration due to the effectively larger probability for one charm quark to find its partner (by a factor of V_{FB}/kV_{co}). Because V_{co} grows faster than V_{FB} this effect is more pronounced for peripheral collisions where the medium lifetime is relatively shorter and the early stage regeneration has greater impact on the final yield. We also note that with V_{co} doubled to $2V_{co}$ the regeneration yield almost drops by a factor of two (dashed line). However, further increasing V_{co} the regeneration yield only decreases by a limited amount due to the fact that for large correlation volume $kV_{co} \sim V_{FB}$ the correlation volume "bubbles" begin merging and their maximal size is restricted to the entire fireball volume, V_{FB}. This can be seen from the fact that for central collisions the regeneration with $2V_{co}$ is already quite close to the limit (Dot-dashed line) where the $c\bar{c}$ pairs are correlated inside the entire fireball (essentially no

correlation volume effect). With the correlation volume effect included the inclusive yields of J/ψ regeneration from thermal and from longitudinal thermal + transverse pQCD charm-quark spectra (with $c\bar{c}$ angular correlation) span a rather large range. The rate equation result (with $1\times V_{co}$) is inside these two limits.

Our studies in this section demonstrate the fact that J/ψ regeneration is very sensitive to the charm quark off-equilibrium effects in both momentum (partial thermalization) and coordinate space (correlation volume effect). It is therefore of crucial importance to implement these effects in a more systematic and more realistic way. Ideally one would obtain the time-dependent joint c and $\bar{c}$ phase space distribution from, *e.g.*, Langevin simulations, as input to address these issues. Work in this direction is planned.

D. ψ' and χ_c Production

In addition to providing a feeddown contribution to J/ψ production, excited charmonia can give valuable complementary information on the medium created in heavy-ion collisions. Being more loosely bound states they usually have larger dissociation rates than J/ψ, and due to their heavier masses, their thermal equilibrium abundances are smaller than J/ψ. Therefore we expect stronger suppression for excited charmonia compared to J/ψ. However, if formation time effects [128, 130, 129] are important, one may observe less suppression for χ_c than for J/ψ.

With the thermal rate equation approach we calculate the ψ' to J/ψ ratio in $\sqrt{s}$=17.3A Pb+Pb collisions and compare to NA50 measurements in Fig. 55. In p+p collisions at SPS energies, the ratio of produced ψ' to J/ψ mesons amounts to a value of about 0.017 (the branching ratios from ψ' and J/ψ into dimuons are included). The nuclear absorption cross section for ψ', $\sigma_{\rm abs}^{\psi'}$, extracted by NA50 is

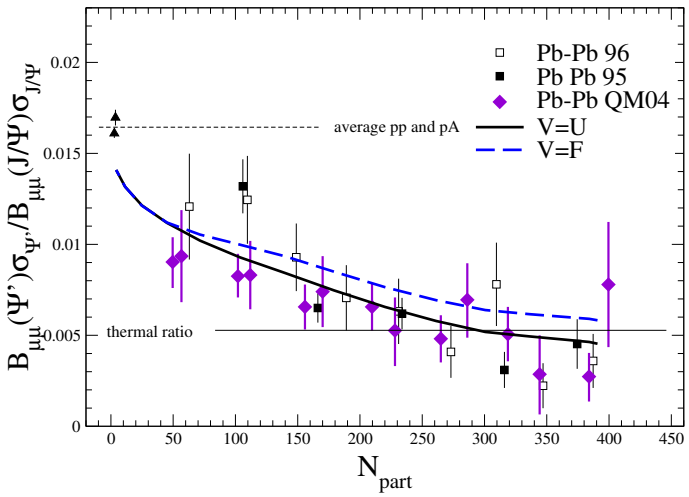

Fig. 55. Inclusive ψ' to J/ψ ratio at SPS compared to NA50 data [137, 138]. Solid line: strong-binding scenario; dashed line weak-binding scenario.

7.9 mb compared to $\sigma_{\rm abs}^{J/\psi}$=4.4mb for J/ψ. Both these two numbers are measured in 400 GeV p+A collisions. With the updated $\sigma_{\rm abs}^{J/\psi}$=7.3 mb at 158 GeV and assuming that the ratio between $\sigma_{\rm abs}^{\psi'}$ and $\sigma_{\rm abs}^{J/\psi}$ is the same for p+A collisions at both 158 GeV and 400 GeV, we obtain $\sigma_{\rm abs}^{\psi'}$=13mb for $\sqrt{s}$=17.3 AGeV Pb+Pb collisions. The data from NA50 suggest additional suppression in ψ' relative to J/ψ in Pb+Pb collisions on top of the larger nuclear absorption cross section for ψ'. In the strong-binding scenario this can be explained by the larger quasifree dissociation rate in QGP due to the smaller binding for ψ'. In the weak binding scenario a significant fraction of charmonia is from regeneration, less ψ' than J/ψ are regenerated due to the lower dissociation temperature of ψ', $T_{diss}^{\psi'} \simeq T_c$ vs. $T_{diss}^{J/\psi} \sim 1.25 T_c$, implying a later onset of regeneration for ψ'.

For Ψ production in $\sqrt{s}$=200 AGeV Au+Au collisions at mid-rapidity at RHIC we use $\sigma_{\rm abs}^{J/\psi}$=$\sigma_{\rm abs}^{\chi_c}$=3.5 mb and $\sigma_{\rm abs}^{\psi'}$ ≃6.5 mb. The ψ' to J/ψ ratio and the χ to J/ψ ratio are displayed in Fig. 56. For χ_c states, we constrain ourselves to χ_{c1} and χ_{c2} with a combined average branching ratio of 27% into J/ψ's. Both drop with centrality

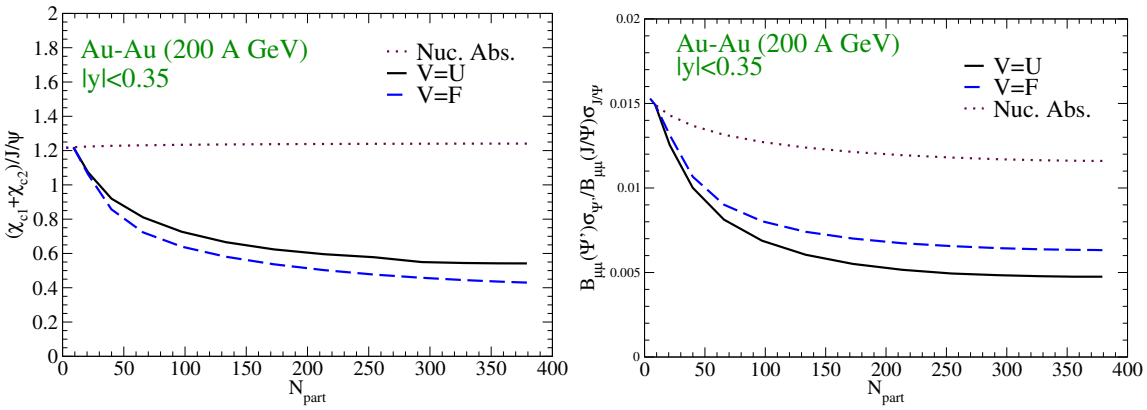

Fig. 56. Inclusive $(\chi_{c1}+\chi_{c2})/(J/\psi)$ ratio (left panel) and $\psi'/(J/\psi)$ ratio (right panel) vs. centrality at mid-rapidity at RHIC evaluated with the thermal rate-equation approach. Solid line: strong binding scenario; dashed line: weak binding scenario. Dotted line: nuclear absorption only. The J/ψ's in the denominator include feeddown from χ_c and ψ'.

below the ratios obtained from CNM-induced suppression.

E. Charmonium Production at FAIR

Finally we briefly discuss charmonium production at the forthcoming FAIR accelerator. The typical collision energy for heavy nuclei is up to $\sqrt{s}$ ~10 AGeV. The medium created at FAIR is expected to have lower initial temperature and larger baryon density than at SPS, recall Figs. 30 and 31. In central collisions QGP is still expected to form.

We calculate charmonium production in $\sqrt{s}$=8.8 AGeV Pb+Pb collisions using the thermal rate equation approach. For the charmonium production cross in p+p collisions we take $\mathrm{d}\sigma_{pp}^{\Psi}/dy$=2.4 nb [94]. We use $\sigma_{\mathrm{abs}}^{J/\psi}$=7.3 mb [106] and $\sigma_{\mathrm{abs}}^{\psi'}$=13.0 mb by assuming the nuclear absorption at FAIR is the same as at SPS. The input charm-quark cross section in p+p collisions is taken as $\mathrm{d}\sigma_{\bar{c}c}/\mathrm{d}y$ $(y{=}0){=}0.2\,\mu$b according to the extrapolation in Ref. [139].

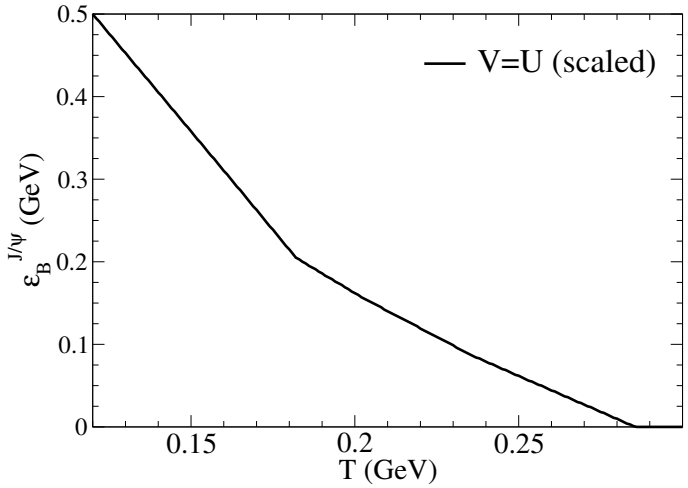

Fig. 57. Temperature dependence of J/ψ binding energy at FAIR in the strong binding scenario. It is obtained by rescaling the J/ψ binding energy at μ_B=0 according to Eq. (6.14).

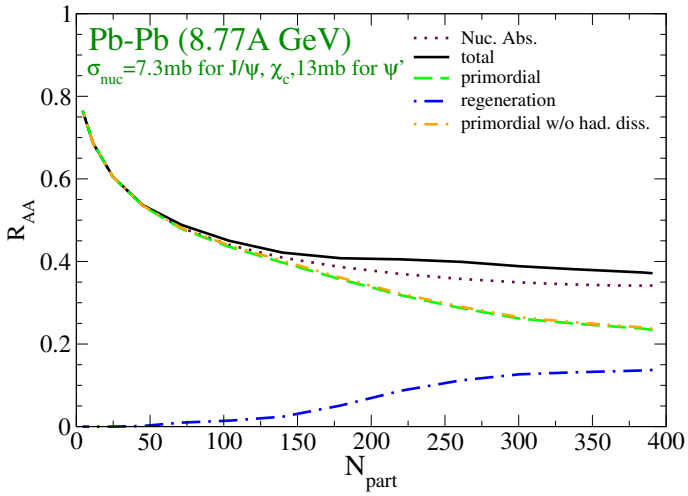

Fig. 58. Results of the thermal rate-equation approach for $R_{AA}^{J/\psi}$ vs. centrality at FAIR. Solid line: total J/ψ yield; dashed line: suppressed primordial production; dot-dashed line: regeneration component; dotted line: primordial production with nuclear absorption only; double-dash-dotted line: suppressed primordial production with quasifree suppression in the QGP only (without hadronic suppression).

Since currently lQCD can only yield reliable results in the low baryon density regime, we lack information on in-medium Ψ properties from first principle calculations for FAIR conditions. For exploratory studies we obtain the in-medium Ψ binding energies at FAIR by rescaling those at RHIC energy according to the ratio between the critical temperatures, $T_c^{\rm FAIR}$ and $T_c^{\rm RHIC}$, namely,

$$\epsilon_B(T)|_{\rm FAIR} = \epsilon_B \left(\frac{T_c^{\rm RHIC}}{T_c^{\rm FAIR}} T \right) \Bigg|_{\rm RHIC} , \tag{6.14}$$

where $T_c^{\rm RHIC}$ is around 180 MeV and $T_c^{\rm RHIC}$ is around 135 MeV, recall Fig. 31. In this dissertation we restrict ourselves to the strong binding scenario. The resulting in-medium binding energy for J/ψ is illustrated in Fig. 57.

We present the resulting centrality dependence of J/ψ R_{AA} in Fig. 58. For central collisions the regeneration component takes up a significant fraction and compensates for the anomalous suppression of the primordial component, rendering the total yield even slightly above that resulting solely from CNM-induced suppression. Most of the suppression of the primordial component is due to nuclear absorption. The majority of the anomalous suppression is from partonic dissociation in the QGP. The suppression in hadronic matter is negligible. Note however that the $SU(4)$ effective theory employed here for hadronic dissociation takes into account only mesons-induced suppression, while the medium at FAIR energy is rather baryon-dense. Therefore the hadronic suppression shown in Fig. 58 must be considered as a lower limit, susceptible to significant corrections from inelastic Ψ collisions with baryons as studied, *e.g.*, in Ref. [140].

Next we evaluate the centrality dependence of the ψ' to J/ψ ratio. In p+p collisions in the FAIR energy regime this ratio is extrapolated to be around 0.01 [141] (The branching ratios from ψ' and J/ψ into dimuons are included). The results of the rate-equation approach, presented in Fig. 59, show that the $\psi'/(J/\psi)$ drops with

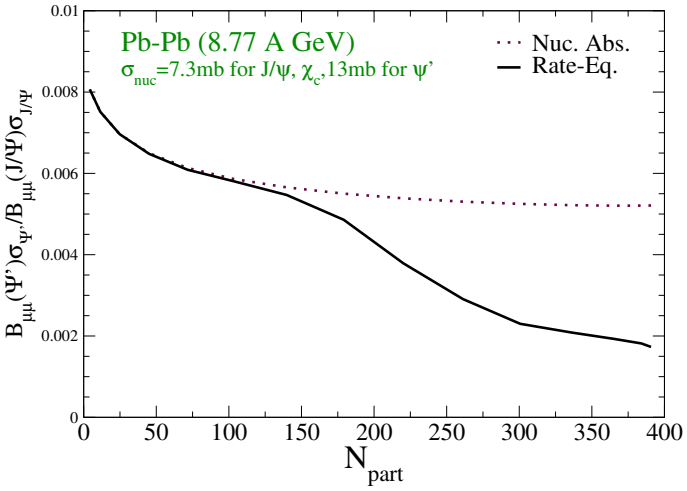

Fig. 59. Results of the thermal rate-equation approach for the $\psi'/(J/\psi)$ ratio vs. centrality at FAIR. Solid line: full result; dotted line: primordial component with CNM effects only.

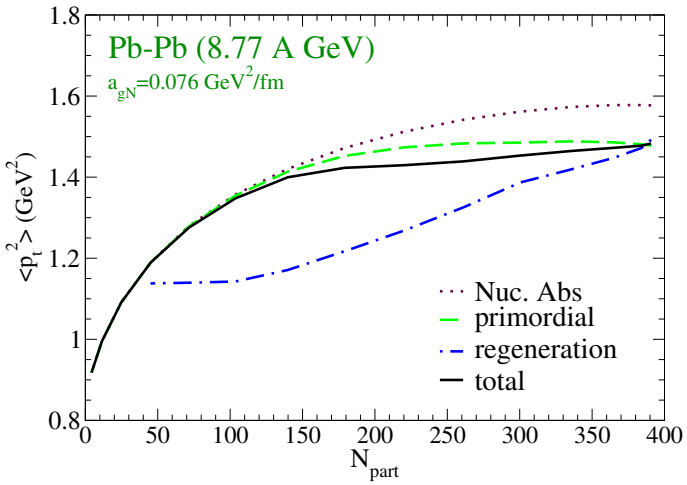

Fig. 60. Results of the thermal rate-equation approach for $\langle p_t^2 \rangle$ vs. centrality at FAIR. Solid line: total J/ψ yield. dashed line: suppressed primordial production; dot-dashed line: thermal regeneration; dotted line: primordial production with CNM effects only.

centrality well below the ratios obtained from CNM-induced suppression as a result of anomalous suppression.

We finally turn to J/ψ transverse momentum spectra. The $\langle p_t^2 \rangle_{pp}$ in p+p collisions at FAIR energy regime is extrapolated to be around $0.8\,\mathrm{GeV}^2$ [142]. We assume a Cronin effect at FAIR similar to that of SPS, with a_{gN}=0.076GeV^2/fm. The resulting centrality dependence of $\langle p_t^2 \rangle$ is displayed in Fig. 60. Similar to SPS energies the $\langle p_t^2 \rangle$ for the primordial and regeneration component exhibits a different centrality dependence, where the former is largely determined by the Cronin effect. The anomalous suppression in QGP induces a small suppression of $\langle p_t^2 \rangle$ due to the larger dissociation rate for Ψ with higher momentum, recall the right panel of Fig. 21. The $\langle p_t^2 \rangle$ for the regeneration component increases with centrality due to the growing collective flow. The p_t dependence of $R_{AA}^{J/\psi}$ for selected centralities is summarized in Fig. 61. Again, the Cronin effect prevails via the primordial component and the collective flow entails the R_{AA} of the regeneration component to increase with p_t.

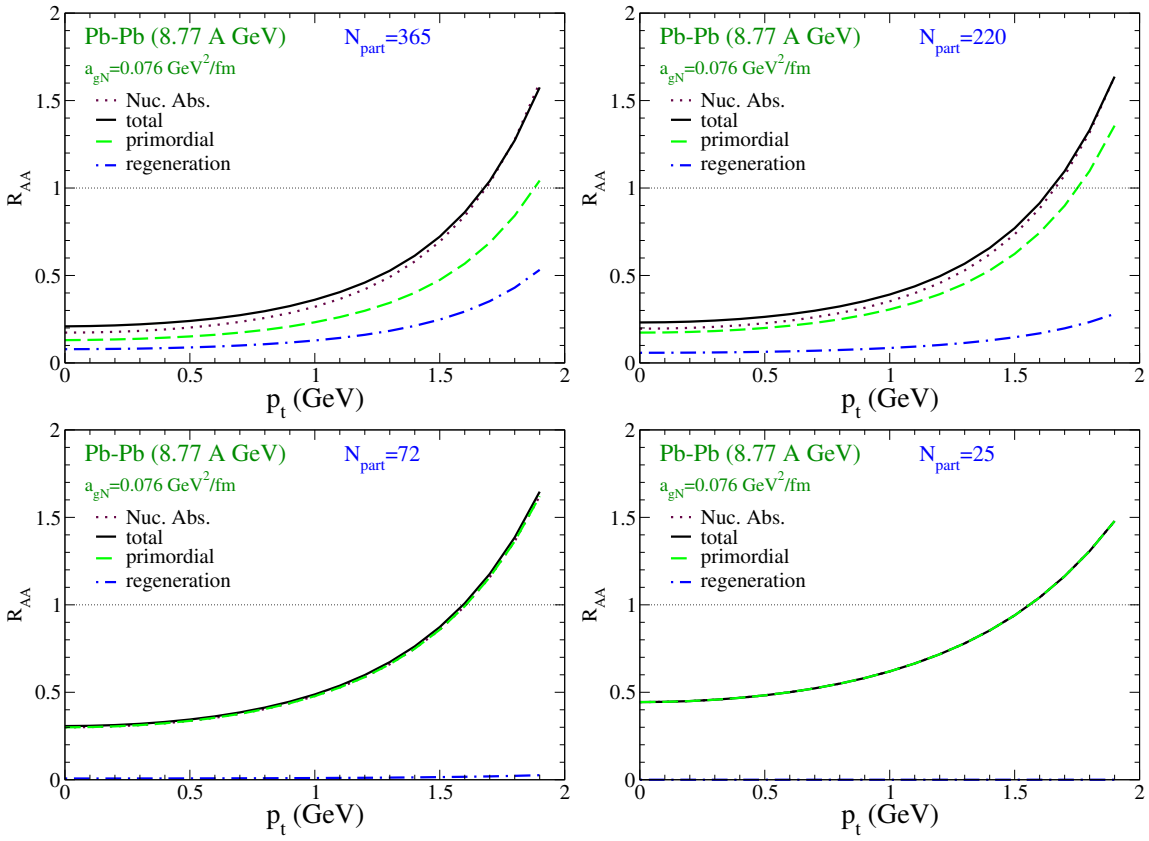

Fig. 61. $R_{AA}^{J/\psi}$ vs. transverse momentum for different centrality selections of Pb+Pb collisions at FAIR. Solid line: total J/ψ yield; dashed line: suppressed primordial production; dot-dashed line: thermal regeneration; dotted line: primordial production with CNM effects only.

CHAPTER VII

CONCLUSIONS AND OUTLOOK

Quantum Chromodynamics (QCD) has been established as the underlying theory for the strong interaction decades ago, but several open problems persist in the non-perturbative regime of the strong interaction to date. One of the prominent problems is to understand the phase structure of the QCD matter which ultimately consists of quarks and gluons. At low temperatures quarks and gluons are confined into hadrons, which become the effective degrees of freedom of the QCD matter. First principle numerical calculations of discretized (lattice) QCD predict that at a temperature of $\sim$170 MeV ($10^{12}K$), ordinary hadronic matter will undergo a transition into a deconfined phase where quarks and gluons are the relevant degrees of freedom, forming the so-called Quark-Gluon Plasma (QGP). One expects to gain insights into the strong interaction and many-body dynamics of QCD through investigating the properties of QGP. However, since QGP exists only at very high temperature, its natural occurrence is rare. Fortunately QGP can be created in present-day's laboratories through ultra-relativistic heavy-ion collisions (URHICs). Since in URHICs QGP exists for a very short time (several fm/c), its properties can only be inferred from finally observed particles. Among these particles the charmonia as the bound states of charm (c) and anti-charm ($\bar{c}$) quarks turn out to be an excellent probe for QGP in URHICs: The strong force binding c and $\bar{c}$ in vacuum is expected to be screened in QGP by surrounding colored quarks and gluons. As a result, charmonium bound states are easier to dissociate by collisions with particles in the medium, leading to a reduction of its experimentally observed yield.

In order to utilize charmonium as a quantitative probe for the properties of the medium created in URHICs, one needs a framework associating experimental observ-

ables with theoretical calculations of in-medium charmonium properties. In this work we have constructed such a framework in which a Boltzmann transport equation is employed to describe the time evolution of the charmonium phase space distribution in URHICs. The in-medium charmonium properties figuring into the transport equation are constrained by thermal lattice QCD (lQCD): We have estimated the charmonium in-medium binding energies from a potential model with input 2-body potentials inferred from the free energy of a static pair of heavy quark and antiquark computed in lQCD. Based on the obtained charmonium in-medium binding energies a "quasifree" approximation has been employed to evaluate the charmonium dissociation and regeneration rates, which are the main inputs to the transport equation. Finally, the consistency between the charmonium binding energy and dissociation rates has been verified with the quarkonium current-current correlation function, another quantity calculated by lQCD independently from the heavy quark free energy. In this way we have established a link between the equilibrium properties of charmonia calculated from first principles, but in euclidean spacetime, and the off-equilibrium evolution of charmonium phase space distributions in heavy-ion collisions.

In the Boltzmann equation the dissociation and regeneration rates play the role of the interface between the microscopic dynamics and the macroscopic observables. In this dissertation we have worked out the momentum dependence of the charmonium dissociation rate, which turns out to be sensitive to the charmonium binding energies. We have also explicitly worked out the charmonium regeneration rates based on the detailed balance between the dissociation and regeneration processes, not restricted to equilibrium conditions. We have found that the dominant regeneration process in QGP is a 3-to-2 process with the initial states consisting of c, $\bar{c}$ and a light parton. In the "quasifree" approximation this 3-to-2 process is found to be factorizable into a 2-to-2 scattering process and a 2-to-1 coalescence process. We have calculated the

regeneration rates with different input charm quark momentum spectra. We have found that, the thermal charm-quark spectra turn out to be much more efficient in regenerating charmonia than the charm-quark spectra from initial hard collisions, due to a larger phase space overlap between c and $\bar{c}$ quarks. Both the inclusive yield of regenerated charmonia and their p_t spectra appear to be very sensitive to the level of thermalization of the input charm quark spectra.

Within the current uncertainties from various inputs our results from the transport equation agree reasonably well with the J/ψ production data measured at the Super-Proton-Synchrotron (SPS) and the Relativistic Heavy-Ion Collider (RHIC), thus corroborating the picture of the deconfining phase transition as predicted by QCD. Moreover we have demonstrated that the J/ψ transverse momentum data exhibit promise for discriminating power for different scenarios for the heavy-quark potential as extracted from lQCD data: The scenario with the internal energy (rather than the free energy) of the $c\bar{c}$ system identified as the potential is slightly favored, though further theoretical studies and more precise experimental data are required to draw definitive conclusions.

To reduce the current uncertainties of the theoretical approach, further developments are in order. First, our calculations show that in URHICs the partition between the primordial and regenerated charmonia is sensitive to their in-medium binding energy, therefore a reliable determination of the in-medium c-$\bar{c}$ 2-body potential is needed for an accurate evaluation of charmonium in-medium binding energy, and thus of the dissociation and regeneration rates.

Second, an explicit calculation of charmonium regeneration from (time-dependent) charm-quark phase-space distributions in c-$\bar{c}$ recombination reactions should be performed. One should use realistic charm-quark spectra as following, *e.g.*, from Langevin simulations with constraints from the T-matrix formalism and from open-charm ob-

servables, to reduce the currently large uncertainty in this part of the input.

Third, hydrodynamic simulation of the medium evolution could be employed for a more detailed and realistic description of the temperature and the flow field of the underlying medium, especially in coordinate space.

Fourth, a microscopic model for primordial $c\bar{c}$ and charmonium production is warranted to better disentangle nuclear shadowing and absorption in the pre-equilibrium stage, including formation-time effects. This would improve the initial conditions for the transport approach in the hot medium.

These developments will ultimately lead to a comprehensive approach which can serve as a quantitative bridge between charmonium phenomenology in heavy-ion collisions and theoretical studies of charmonia in the QGP (and hadronic matter). It will enable us to deduce from experimental observables effective degrees of freedom for the hot and dense medium created at various collision energies, improving our knowledge of the phase structure of hot and dense QCD matter. Furthermore it will provide insights into basic properties of the strong force in terms of color screening of Coulomb and confining interactions. All these aspects of information will eventually contribute to the establishment of a coherent picture of the strong interaction in the non-perturbative regime.

REFERENCES

[1] D. J. Gross and F. Wilczek, Phys. Rev. Lett. **30**, 1343 (1973).

[2] H. D. Politzer, Phys. Rev. Lett. **30**, 1346 (1973).

[3] M. Schmelling, in *Proc. of 28. International Conference on High-Energy Physics (ICHEP 96), Warsaw, Poland, 25-31 Jul 1996*, edited by Z. Ajduk and A.K. Wroblewski, (World Scientific, Singapore, 1996); ICHEP. **96**, 91 (1996); arXiv:hep-ex/9701002.

[4] A. Bazavov, C. Bernard, C. DeTar, Steven Gottlieb, U.M. Heller *et al.*, Rev. Mod. Phys. **82**, 1349 (2010).

[5] P. Petreczky, Nucl. Phys. A **830**, 11C (2009).

[6] M. Cheng, N. H. Christ, S. Datta, J. van der Heide, C. Jung *et al.*, Phys. Rev. D **77**, 014511 (2008).

[7] R. Rapp, T. Schafer, E. V. Shuryak and M. Velkovsky, Phys. Rev. Lett. **81**, 53 (1998).

[8] M. G. Alford, K. Rajagopal and F. Wilczek, Phys. Lett. B **422**, 247 (1998).

[9] R. Rapp and H. van Hees, in *The Physics of Quarks: New Research (Horizons in World Physics)*, edited by N. L. Watson and T. M. Grant, (Nova Science Publishers, New York, 2009), p. 87-138; arXiv:0803.0901 [hep-ph].

[10] T. Hirano, N. van der Kolk and A. Bilandzic, Lect. Notes Phys. **785**, 139 (2010).

[11] J. Adams, M.M. Aggarwal, Z. Ahammed, J. Amonett, B.D. Anderson *et al.* [STAR Collaboration], Nucl. Phys. A **757**, 102 (2005).

[12] K. Adcox, S.S. Adler, S. Afanasiev, C. Aidala, N.N. Ajitanand *et al.* [PHENIX Collaboration], Nucl. Phys. A **757**, 184 (2005).

[13] P. Huovinen, P. F. Kolb, U. W. Heinz, P. V. Ruuskanen and S. A. Voloshin, Phys. Lett. B **503**, 58 (2001).

[14] S. Pratt, Phys. Rev. Lett. **53**, 1219 (1984).

[15] X. N. Wang and M. Gyulassy, Phys. Rev. Lett. **68**, 1480 (1992).

[16] S. Wicks, W. Horowitz, M. Djordjevic and M. Gyulassy, Nucl. Phys. A **784**, 426 (2007).

[17] K. Nakamura [Particle Data Group], J. Phys. G **37**, 075021 (2010).

[18] L. Antoniazzi, M. Arenton, Z. Cao, T. Chen, S. Conetti *et al.* [E705 Collaboration], Phys. Rev. D **46**, 4828 (1992).

[19] I. Abt, A. Abyzov, M. Adams, H. Albrecht, V. Amaral *et al.* [HERA-B Collaboration], Phys. Lett. B **561**, 61 (2003).

[20] F. Karsch and R. Petronzio, Z. Phys. C **37**, 627 (1988).

[21] E. Eichten, K. Gottfried, T. Kinoshita, K. D. Lane and T. M. Yan, Phys. Rev. D **17**, 3090 (1978) [Erratum-ibid. D **21**, 313 (1980)].

[22] E. Eichten, K. Gottfried, T. Kinoshita, K. D. Lane and T. M. Yan, Phys. Rev. D **21**, 203 (1980).

[23] S. Jacobs, M. G. Olsson and C. I. Suchyta, Phys. Rev. D **33**, 3338 (1986) [Erratum-ibid. D **34**, 3536 (1986)] [Phys. Rev. D **34**, 3536 (1986)].

[24] F. Karsch, M. T. Mehr and H. Satz, Z. Phys. C **37**, 617 (1988).

[25] O. Kaczmarek and F. Zantow, Phys. Rev. D **71**, 114510 (2005).

[26] T. Matsui and H. Satz, Phys. Lett. B **178**, 416 (1986).

[27] P. Petreczky and K. Petrov, Phys. Rev. D **70**, 054503 (2004).

[28] X. Zhao and R. Rapp, submitted to Phys. Rev. C (2010); arXiv:1008.5328 [hep-ph].

[29] A. Jakovac, P. Petreczky, K. Petrov and A. Velytsky, Phys. Rev. D **75**, 014506 (2007).

[30] S. Datta, F. Karsch, P. Petreczky and I. Wetzorke, Phys. Rev. D **69**, 094507 (2004).

[31] G. Aarts, C. Allton, M.B. Oktay, M. Peardon and J. I. Skullerud, Phys. Rev. D **76**, 094513 (2007).

[32] T. Umeda, Phys. Rev. D **75**, 094502 (2007).

[33] T. Umeda, PoS **LAT2007**, 233 (2007).

[34] P. Petreczky, Eur. Phys. J. C **62**, 85 (2009).

[35] M. Asakawa, T. Hatsuda and Y. Nakahara, Prog. Part. Nucl. Phys. **46**, 459 (2001).

[36] A. Andronic, P. Braun-Munzinger, K. Redlich and J. Stachel, Nucl. Phys. A **789**, 334 (2007).

[37] L. Grandchamp and R. Rapp, Phys. Lett. B **523**, 60 (2001).

[38] A. Polleri, [unpublished manuscript] (2003), arXiv:nucl-th/0303065.

[39] A. Polleri, T. Renk, R. Schneider and W. Weise, Phys. Rev. C **70**, 044906 (2004).

[40] L. Yan, P. Zhuang and N. Xu, Phys. Rev. Lett. **97**, 232301 (2006).

[41] B. Zhang, C. M. Ko, B. A. Li, Z. W. Lin and S. Pal, Phys. Rev. C **65**, 054909 (2002).

[42] O. Linnyk, E. L. Bratkovskaya and W. Cassing, Nucl. Phys. A **807**, 79 (2008).

[43] R.L. Thews and M.L. Mangano, Phys. Rev. C **73**, 014904 (2006).

[44] L. Grandchamp, R. Rapp and G.E. Brown, Phys. Rev. Lett. **92**, 212301 (2004).

[45] P. Braun-Munzinger and J. Stachel, Phys. Lett. B **490**, 196 (2000).

[46] J. Rafelski and M. Danos, Phys. Lett. B **97**, 279 (1980).

[47] M.I. Gorenstein, A.P. Kostyuk, H. Stoecker and W. Greiner, Phys. Lett. B **509**, 277 (2001).

[48] C. M. Ko, V. Koch, Z. w. Lin, K. Redlich, M. A. Stephanov and X. N. Wang, Phys. Rev. Lett. **86**, 5438 (2001).

[49] S. Pal, C. M. Ko and Z. w. Lin, Phys. Rev. C **64**, 042201 (2001).

[50] F. Riek and R. Rapp, Phys. Rev. C, **82**, 035201 (2010).

[51] O. Kaczmarek, PoS C **POD07**, 043 (2007).

[52] M. E. Peskin, Nucl. Phys. B **156**, 365 (1979); G. Bhanot and M. E. Peskin, Nucl. Phys. B **156**, 391 (1979).

[53] B. L. Combridge, Nucl. Phys. B **151**, 429 (1979).

[54] Z. w. Lin and C. M. Ko, Phys. Rev. C **62**, 034903 (2000).

[55] R. Rapp and H. van Hees, in *Quark-Gluon Plasma 4*, edited by R. Hwa and X.N. Wang, (World Scientific Singapore, 2010), p. 111-206; arXiv:0903.1096 [hep-ph].

[56] H. van Hees and R. Rapp, Phys. Rev. C **71**, 034907 (2005).

[57] T. Sjostrand, P. Eden, C. Friberg, L. Lonnblad, G. Miu, S. Mrenna and E. Norbin, Comput. Phys. Commun. **135**, 238 (2001).

[58] V. Greco, C. M. Ko and R. Rapp, Phys. Lett. B **595**, 202 (2004).

[59] R. Rapp, D. Blaschke and P. Crochet, Prog. Part. Nucl. Phys. **65**, 209 (2010).

[60] K.L. Haglin and C. Gale, Phys. Rev. C **63**, 065201 (2001).

[61] L. Grandchamp-Desraux, Charmonium Production In Heavy-Ion Collisions, Ph.D. dissertation, Stony Brook University, Stony Brook, New York, 2003.

[62] R. S. Azevedo and M. Nielsen, Phys. Rev. C **69**, 035201 (2004).

[63] C. M. Ko, B. Zhang, X. N. Wang and X. F. Zhang, Phys. Lett. B **444**, 237 (1998).

[64] D. Cabrera and R. Rapp, Phys. Rev. D **76**, 114506 (2007).

[65] A. Mocsy and P. Petreczky, Phys. Rev. D **77**, 014501 (2008).

[66] A. Mocsy and P. Petreczky, Phys. Rev. D **73**, 074007 (2006).

[67] G.T. Bodwin, E. Braaten and G.P. Lepage, Phys. Rev. D **51**, 1125 (1995) [Erratum-ibid. D **55**, 5853 (1997)].

[68] S. A. Bass, M. Belkacem, M. Bleicher, M. Brandstetter, L. Bravina *et al.*, Prog. Part. Nucl. Phys. **41**, 255 (1998).

[69] W. Cassing and E. L. Bratkovskaya, Phys. Rept. **308**, 65 (1999).

[70] U. W. Heinz, in *Relativistic Heavy Ion Physics, Landolt-Börnstein, New Series, Vol. I 23*, edited by R. Stock, (Springer Verlag, New York, 2010), cha. 5-1; arXiv:0901.4355 [nucl-th].

[71] R. Rapp and J. Wambach, Eur. Phys. J. A **6**, 415 (1999).

[72] R. Rapp and E. V. Shuryak, Phys. Lett. B **473**, 13 (2000).

[73] P. Braun-Munzinger, K. Redlich and J. Stachel, in *Quark-Gluon Plasma 3*, edited by R. Hwa and X.N. Wang, (World Scientific Singapore, 2003), p. 491-599; arXiv:nucl-th/0304013.

[74] M. Cheng, N. H. Christ, S. Datta, J. van der Heide, C. Jung *et al.*, Phys. Rev. D **74**, 054507 (2006).

[75] I. Arsene, I.G. Bearden, D. Beavis, C. Besliu, B. Budick *et al.* [BRAHMS Collaboration], Nucl. Phys. A **757**, 1 (2005).

[76] X. Zhao and R. Rapp, Eur. Phys. J. C **62**, 109 (2009).

[77] C. M. Hung and E. V. Shuryak, Phys. Rev. C **57**, 1891 (1998).

[78] P. J. Siemens and J. O. Rasmussen, Phys. Rev. Lett. **42**, 880 (1979).

[79] E. Schnedermann, J. Sollfrank and U. W. Heinz, Phys. Rev. C **48**, 2462 (1993).

[80] F. Cooper and G. Frye, Phys. Rev. D **10**, 186 (1974).

[81] M. B. Einhorn and S. D. Ellis, Phys. Rev. D **12**, 2007 (1975).

[82] J. F. Amundson, O. J. P. Eboli, E. M. Gregores and F. Halzen, Phys. Lett. B **390**, 323 (1997).

[83] R. Gavai, D. Kharzeev, H. Satz, G. A. Schuler, K. Sridhar and R. Vogt, Int. J. Mod. Phys. A **10**, 3043 (1995).

[84] E. L. Berger and D. L. Jones, Phys. Rev. D **23**, 1521 (1981).

[85] C. H. Chang, Nucl. Phys. B **172**, 425 (1980).

[86] R. Baier and R. Ruckl, Phys. Lett. B **102**, 364 (1981).

[87] R. Baier and R. Ruckl, Z. Phys. C **19**, 251 (1983).

[88] G. A. Schuler, CERN Preprint CERN-TH-7170-94, (1994); arXiv:hep-ph/9403387.

[89] E. Braaten, S. Fleming and T. C. Yuan, Ann. Rev. Nucl. Part. Sci. **46**, 197 (1996).

[90] M. Beneke, in *Stanford 1996, The Strong Interaction, from Hadrons to Partons*, edited by Jennifer Chan, Lilian DePorcel, and Lance Dixon, (Proceedings of the 1996 SLAC Summer School, Stanford, 1996), p. 549-574; arXiv:hep-ph/9703429.

[91] N. Brambilla, M. Krmer, R. Mussa, A. Vairo, G. Bali *et al.* [Quarkonium Working Group], published as CERN Yellow Report, CERN-2005-005, Geneva, 2005; arXiv:hep-ph/0412158.

[92] A. Adare, S. Afanasiev, C. Aidala, N. N. Ajitanand, Y. Akiba *et al.* [PHENIX Collaboration], Phys. Rev. Lett. **101**, 122301 (2008).

[93] B. I. Abelev, M. M. Aggarwal, Z. Ahammed, B. D. Anderson, D. Arkhipkin *et al.* [STAR Collaboration], Phys. Rev. C **80**, 041902 (2009).

[94] I. Abt, M. Adams, M. Agari, H. Albrecht, A. Aleksandrov *et al.* [HERA-B Collaboration], Phys. Lett. B **638**, 407 (2006).

[95] A. Adare, S. Afanasiev, C. Aidala, N. N. Ajitanand, Y. Akiba *et al.* [PHENIX Collaboration], Phys. Rev. Lett. **98**, 232002 (2007).

[96] C. Lourenco and H. K. Wohri, Phys. Rept. **433**, 127 (2006).

[97] A. Adare, S. Afanasiev, C. Aidala, N. N. Ajitanand, Y. Akiba *et al.* [PHENIX Collaboration], Phys. Rev. Lett. **97**, 252002 (2006).

[98] Y. f. Zhang, J. Phys. G **35**, 104022 (2008).

[99] M. L. Miller, K. Reygers, S. J. Sanders and P. Steinberg, Ann. Rev. Nucl. Part. Sci. **57**, 205 (2007).

[100] C. W. De Jager, H. De Vries and C. De Vries, Atom. Data Nucl. Data Tabl. **14**, 479 (1974).

[101] N. Armesto, J. Phys. G **32**, R367 (2006).

[102] K. J. Eskola, H. Paukkunen and C. A. Salgado, JHEP **0904**, 065 (2009).

[103] A. Adare, S. S. Adler, S. Afanasiev, C. Aidala, N. N. Ajitanand *et al.* [PHENIX Collaboration], Phys. Rev. C **77**, 024912 (2008).

[104] N. S. Topilskaya, C. Alexa, R. Arnaldi, M. Atayan, C. Baglin *et al.* [NA50 Collaboration], Nucl. Phys. A **715**, 675 (2003).

[105] R. Arnaldi, talk at ECT* Workshop on "Heavy Quarkonia Production in Heavy-Ion Collisions", Trento, Italy, May 25-29, 2009;
http://www.ect.it/Meetings/ConfsWksAndCollMeetings/
ConfWksDocument/2009/Talks/WORKSHOP_25May09/arnaldi.ppt

[106] R. Arnaldi, K. Banicz, J. Castor, B. Chaurand, W. Chen *et al.* [NA60 Collaboration], [unpublished manuscript] (2010); arXiv:1004.5523 [nucl-ex].

[107] B. Alessandro, C. Alexa, R. Arnaldi, M. Atayan, S. Beolè *et al.* [NA50 Collaboration], Eur. Phys. J. C **48**, 329 (2006).

[108] X. Zhao and R. Rapp, Phys. Lett. B **664**, 253 (2008).

[109] A. Frawley, talk at CATHIE-INT Mini-Program on "Quarkonium in Hot Media: from QCD to Experiment", Seattle (WA), June 16-26, 2009; http://www.int.washington.edu/talks/WorkShops/int_09_42W/

[110] E. G. Ferreiro, F. Fleuret, J. P. Lansberg and A. Rakotozafindrabe, Phys. Rev. C **81**, 064911 (2010).

[111] J. Hufner and P. f. Zhuang, Phys. Lett. B **515**, 115 (2001) [arXiv:nucl-th/0104078].

[112] J. Cleymans, K. Redlich and E. Suhonen, Z. Phys. C **51**, 137 (1991).

[113] W. M. Yao *et al.* [Particle Data Group], J. Phys. G **33**, 1 (2006).

[114] L. Grandchamp and R. Rapp, Nucl. Phys. A **709**, 415 (2002).

[115] H. van Hees, M. Mannarelli, V. Greco and R. Rapp, Phys. Rev. Lett. **100**, 192301 (2008).

[116] H. van Hees, V. Greco and R. Rapp, Phys. Rev. C **73**, 034913 (2006).

[117] S. Hamieh, K. Redlich and A. Tounsi, Phys. Lett. B **486**, 61 (2000).

[118] C. Young and E. Shuryak, Phys. Rev. C **79**, 034907 (2009).

[119] S. A. Klinksiek, Finding the Charm in 800-GeV/c p-Cu and p-Be Single Muon Spectra, Ph.D. dissertation, The University of New Mexico, Albuquerque, New Mexico, 2003; arXiv:hep-ex/0609002.

[120] R. Rapp, Eur. Phys. J. C **43**, 91 (205).

[121] X. Zhao and R. Rapp, in preparation (2010).

[122] L. Ramello *et al.* [NA50 Collaboration], Nucl. Phys. A **715**, 243 (2003).

[123] B. Alessandro *et al.* [NA50 Collaboration], Eur. Phys. J. C **39**, 335 (2005).

[124] A. Adare, S. Afanasiev, C. Aidala, N. N. Ajitanand, Y. Akiba *et al.* [PHENIX Collaboration], Phys. Rev. Lett. **98**, 232301 (2007).

[125] R. Arnaldi, private communication (2010).

[126] M. C. Abreu, B. Alessandro, C. Alexa, R. Arnaldi, M. Atayan *et al.* [NA50 Collaboration], Phys. Lett. B **499**, 85 (2001).

[127] X. Zhao and R. Rapp, in *Proc. of the 24th Winter Workshop on Nuclear Dynamics*, edited by W. Bauer, R. Bellwied, J. W. harris and C. Market, (EP Systema Bt., Budapest, 2008), p. 195-200; arXiv:0806.1239 [nucl-th].

[128] J.P. Blaizot and J.Y. Ollitrault, Phys. Rev. D **39** (1989) 232.

[129] F. Karsch and R. Petronzio, Z. Phys. C **37** (1988) 627.

[130] S. Gavin and R. Vogt, Nucl. Phys. B **345**, 104 (1990); J. P. Blaizot and J. Y. Ollitrault, Phys. Rev. D **39**, 232 (1989); F. Karsch and R. Petronzio, Z. Phys. C **37**, 627 (1988).

[131] D. E. Acosta, J. Adelman, T. Affolder, T. Akimoto, M. G. Albrow *et al.* [CDF Collaboration], Phys. Rev. D **71** (2005) 032001.

[132] Z. Tang and Z. Xu, private communication (2008).

[133] Z. Tang [STAR Collaboration], J. Phys. G **35**, 104135 (2008).

[134] X. N. Wang and F. Yuan, Phys. Lett. B **540**, 62 (2002).

[135] L. Ravagli and R. Rapp, Phys. Lett. B **655**, 126 (2007).

[136] T. Song, C. M. Ko, S. H. Lee and J. Xu, [unpublished manuscript] (2010); arXiv:1008.2730 [hep-ph].

[137] M. C. Abreu, B. Alessandro, C. Alexa, R. Arnaldi, J. Astruc *et al.* [NA50 Collaboration], Nucl. Phys. A **638**, 261 (1998).

[138] M. Sitta, B. Alessandro, C. Alexa, R. Arnaldi, M. Atayan *et al.* [NA50 Collaboration], J. Phys. G **30**, S1175 (2004).

[139] A. Andronic, P. Braun-Munzinger, K. Redlich and J. Stachel, Phys. Lett. B **659**, 149 (2008).

[140] W. Liu, C. M. Ko and Z. W. Lin, Phys. Rev. C **65**, 015203 (2002).

[141] O. Linnyk, E. L. Bratkovskaya, W. Cassing and H. Stoecker, Nucl. Phys. A **786**, 183 (2007).

[142] A. K. Chaudhuri, J. Phys. G **32**, 229 (2006).

VITA

Name:	Xingbo Zhao
Address:	Department of Physics and Astronomy, 12 Physics Hall, Ames, Iowa, 50011-3160
Email Address:	xbzhao@tamu.edu
Education:	B.S., Physics, University of Science and Technology of China, 2005 Ph.D., Physics, Texas A&M University, 2010